

Comprehensive study of non-synoptic wind effects on buildings

Mu'ath Al-Makhadmeh

A Thesis in
The Department of
Building, Civil and Environmental Engineering

Presented in Partial Fulfillment of the Requirements
for the Degree of Master of Applied Science (Building Engineering)
at
Concordia University
Montreal, Quebec, Canada

February 2022

© Mu'ath Al-Makhadmeh, 2022

CONCORDIA UNIVERSITY
School of Graduate Studies

This is to certify that this thesis prepared.

By: Mu'ath Al-Makhadmeh

Entitled: Comprehensive study of non-synoptic wind effects on buildings

and submitted in partial fulfillment of the requirements for the degree of

Master of Applied Science (Building Engineering)

complies with the regulations of the University and meets the accepted standards with respect to originality and quality.

Signed by the final Examining Committee:

_____	Chair
Dr. Bruno Lee	
_____	Examiner
Dr. Lyes Kadem	External (to program)
_____	Examiner
Dr. Anjan Bhowmick	
_____	Supervisor
Dr. Ted. Stathopoulos	

Approved by

Dr. Mazdak Nik-Bakht, GPD
Department of Building, Civil and Environmental Engineering

Dr. Mourad Debbabi, Dean
Faculty of Engineering and Computer Science

Date

Feb 23, 2022

ABSTRACT

Comprehensive study of non-synoptic wind effects on buildings

Mu'ath Al-Makhadmeh

The present study examines wind loads on flat roof low-rise buildings under the effect of the simulated wind speed profile of the downburst phenomena. Examination of buildings is necessary since very few studies have examined non-synoptic winds. Indeed, non-synoptic winds have not been considered in the wind provisions of codes and standards. As a result, the interaction between wind and buildings under these phenomena should be investigated as in the case for the assessment of current well-known Atmospheric Boundary Layer (ABL) winds.

Many trials have been carried out at the wind tunnel of Concordia University to simulate the downburst phenomena. Different configurations have been tried to simulate wind speed profile close to the available target full-scale data. The produced wind speed profile and turbulence intensity are presented in terms of comparisons among the target profile, the ABL profile and downbursts profiles of previous studies.

The size of roof pressure zones and the magnitude of pressure coefficients on flat roofs of low-rise buildings have been examined experimentally in the wind tunnel of Concordia University. Two building models were constructed at a length scale of 1:400 with identical plan dimensions (60 m x 60 m) and two building heights (10 m and 20 m). The models were tested for 7 wind directions: 0°, 15°, 30°, 45°, 60°, 75° and 90°. The pressure measurement results have been presented in terms of contours of enveloped local pressure coefficients. The results of the current study have been compared with those of ABL (same model dimensions) and downburst of previous studies.

It was found that the produced downburst wind speed profile of the current study agrees well with the target full scale data. The velocity increases at a low height and decreases going upwards.

The results of the present study show that the wind direction plays a main role in the pressure coefficient distributions, the most critical wind direction is different for the roof corner and the roof edge. In addition, it was found that the higher building heights experience higher wind loads.

Acknowledgment

Praise to Allah, the almighty, who has guided us to this; and we would never have been guided if Allah had not guided us.

Dedicated to:

The soul of my Father (may Allah Almighty bless him), who I lost during my studies, who loved and encouraged me throughout my life. Daddy I miss you so much....

To my beloved Mother Who is standing beside me in every moment of my life. Your prayers are the most amazing support for me, and still and I will need them the rest of my life.

I would like to express my deep and sincere gratitude to my supervisor Dr. Ted Stathopoulos, for providing me the opportunity to work in the wind engineering field. Thank you for the valuable guidance and continuous support. It has been an honor to work under his supervision.

I would like to thank my beloved wife, Lubna for her love, continuous support, all the sacrifices that she made for me to overcome many challenges throughout my life. I am so thankful to my lovely twins, Omar and Ban, who were born starting of my studies. Thank you for the joy and love you bring to my life. I would like to thank my sister Wala'a, Eman and my brother Hani and Tariq, for their support and love. I also thank my family in-law for their support.

I would like to thank my brother-in-law, Tariq, for his support and advice. Special thanks go to my colleagues and friends, especially Hatem, Murad for their support and teaching me everything about the experiment in the wind tunnel and their help and encouragement during my studies.

TABLE OF CONTENTS

List Of Figures	viii
List Of Tables	xi
Chapter 1. Introduction	1
1.1 Overview	1
1.2 Thunderstorm Damage.....	6
1.3 Scope and Objectives	8
1.4 Thesis Outline	9
Chapter 2. Non-synoptic winds	10
2.1 Tornado	10
2.1.1 Previous work (Physical characteristics - Available facilities).....	10
2.1.2 Review of facilities.....	15
2.2 Downburst.....	26
2.2.1 Previous work (Physical characteristics - Available facilities).....	26
2.2.2 Review of Facilities	27
Chapter 3. Wind Codes and Standards - Non-synoptic Winds	32
3.1 National Building Code of Canada (NBCC).....	32
3.2 American Society of Civil Engineers (ASCE 7)	34
3.2.1 The Extended Method.....	37
3.2.2 The Simplified method.....	38
Chapter 4. Experimental Methodology	41
4.1 Description of the facility – applications.....	41
4.1.1 Building Aerodynamics Laboratory at Concordia university	42
4.1.2 Atmospheric Boundary Layer velocity profile (ABL).....	45

4.2	Modification of flow simulation attempts	48
4.3	Model Configuration.....	58
Chapter 5.	Experimental Results and Analysis	61
5.1	Mean wind speed and turbulence intensity	61
5.2	Wind load measurements.....	73
5.2.1	Contours of the most critical pressure coefficients	73
5.2.2	Local pressure coefficients	78
5.2.3	Comparison with ABL previous studies	83
5.2.4	Comparison with downburst previous studies	87
Chapter 6.	Conclusions and future work	90
6.1	Conclusions.....	90
6.2	Future work.....	91
References	92
Appendix A	97
Appendix B	102

List Of Figures

Figure 1-1 Real tornado characteristics, Image source: from Encyclopædia Britannica, Inc. https://www.britannica.com/science/tornado/Physical-characteristics-of-tornadoes	2
Figure 1-2 Downdraft characteristics, source. Britannica, https://www.britannica.com/science/updraft ...	4
Figure 1-3 Characteristics comparison of horizontal wind profile in a straight-line with microburst, after Sengupta and Sarkar, (2008).....	5
Figure 1-4 Joplin tornado damage in Joplin, Mo, May 2011, source: https://www.theatlantic.com/photo/2011/05/tornado-damaged-joplin-from-above/100073/	7
Figure 1-5 Macroburst trees damage occurred in Minnesota in 2011, source: https://www.nssl.noaa.gov/education/svrwx101/wind/types/	8
Figure 2-1 Schematic diagram of tornado showing the aspect ratio parameters (Davies-Jones, 1986)	11
Figure 2-2 Comparison of scaled tangential velocity profiles for laboratory tornado and the Mulhall radar data (Haan et al., 2008)	13
Figure 2-3 Schematic diagram of tornado vortices chamber (Church et al., 1979).....	16
Figure 2-4 Schematic diagram of Purdue university simulator (Church et al., 1979).....	17
Figure 2-5 Schematic diagram of Texas tech university simulators A) TTU -VSII ((Amit R. Mishra et al., 2008) and B) VorTECH (Tang et al., 2018).....	19
Figure 2-6 ISU Simulator A) Schematic diagram (Haan et al., 2008) and B) photo of circular duct (Haan et al., 2009).....	21
Figure 2-7 MINI-ISU simulator	22
Figure 2-8 A) photo of the multi-fan system and B) Schematic diagram of WindEEE Dome, after (Hangan, 2014).....	23
Figure 2-9 Schematic diagram of Tongji university simulator, after (Cao et al., 2018)	24
Figure 2-10 Schematic diagram of tornado simulator at Tokyo polytechnic university, after (Sabareesh et al., 2012).....	25
Figure 2-11 Schematic diagram of Texas Tech jet wind tunnel, after Chay and Letchford (2002).....	28
Figure 2-12 Schematic diagram of ISU microburst simulator, after Zhang et al. (2013)	29
Figure 2-13 Schematic diagram of Birmingham university jet nozzle, after McConville et al. (2009)	30
Figure 2-14 Schematic diagram of Western university downburst simulator, after Hangan et al., (2017)	31
Figure 3-1 Tornado-prone regions of Canada, after (NBC2015, 2015).....	33
Figure 3-2 Tornado Gust Wind Speed with Annual Probability of 10 – 5, after (ASCE/SEI 7-10).....	35

Figure 3-3 Recorded tornadoes between 1950–2013, with a rating of EF3–EF5; after, (ASCE 7, 2016)	36
Figure 3-4 Design wind speed map (FEMA, 2015)	39
Figure 4-1 Construction view of Concordia University wind tunnel (Top and side view)	43
Figure 4-2 Front view of the Boundary Layer Wind Tunnel at Concordia University	44
Figure 4-3 Exposure C and Exposure B at the wind tunnel of Concordia University, after (Aldoum and Stathopoulos, 2020)	46
Figure 4-4 Vertical mean wind speed and turbulence intensity for exposure C and exposure B, after (Aldoum and Stathopoulos, 2020)	47
Figure 4-5 Trial 1 configurations at BLWT of Concordia University; A) one roughness element panel B) two roughness element panels	49
Figure 4-6 Trial 2 configurations at BLWT of Concordia University; A) with spires, B) without spires	51
Figure 4-7 Trial 3 configuration at BLWT of Concordia University	52
Figure 4-8 Typical configuration of Trial 4 at BLWT of Concordia University	52
Figure 4-9 A cross section of the BLWT at Concordia University shows Trial 4 modifications: A) top view, B) side view	54
Figure 4-10 Typical configuration of trial 5 at BLWT of Concordia University	55
Figure 4-11 A cross section of the BLWT at Concordia University shows Trial 5 modifications: A) top view, B) side view	56
Figure 4-12 60m x 60m building model with pressure tap layout on the roof	59
Figure 5-1 Velocity profile of trial 4, Configuration II; A) Test Configuration, B) Set 1, C) Set 2	63
Figure 5-2 Velocity profile of trial 4, Configuration III; A) Test configuration, B) Set 1, C) Set 2	64
Figure 5-3 Velocity profile of trial 5, Configuration I. (H1=15 cm, H2=20 cm, X=2 m)	65
Figure 5-4 Velocity profile of trial 5, Configuration II. (H1=15 cm, H2=20 cm, X=1.5 m)	65
Figure 5-5 Velocity profile of trial 5, Configuration III. (H1=15 cm, H2=20 cm, X=1 m)	66
Figure 5-6 Velocity profile of trial 5, Configuration IV. (H1=15 cm, H2=0 cm, X=2 m)	66
Figure 5-7 Comparison of the vertical wind velocity profiles between the present experiment and the corresponding previous studies	67
Figure 5-8 Velocity profile of exposure B	70
Figure 5-9 Comparison of the longitudinal turbulence intensity profiles between the present experiment and the corresponding previous studies	71
Figure 5-10 Power spectral density of longitudinal turbulence component evaluated at one-sixth the gradient height	72

Figure 5-11 Contours of most critical mean pressure coefficients (C_p) for all wind directions ($H=10$ m)	74
Figure 5-12 Contours of most critical peak pressure coefficients (C_{pCg}) for all wind directions ($H=10$ m)	75
Figure 5-13 Contours of most critical mean pressure coefficients (C_p) for all wind directions ($H=20$ m)	76
Figure 5-14 Contours of most critical peak pressure coefficients (C_{pCg}) for all wind directions ($H=20$ m)	77
Figure 5-15 Extreme negative peak and mean pressure coefficients on windward edge of the building versus wind direction.	79
Figure 5-16 Extreme negative peak and mean pressure coefficients on windward corner of the building versus wind direction.	80
Figure 5-17 Variation of wind pressure coefficients along the line at the concurrent edge for 45° wind direction	81
Figure 5-18 Variation of wind pressure coefficients along the roof centerline for 0° wind direction	82
Figure 5-19 Comparison between the present study and Alrawashdeh and Stathopoulos (2015), a) Variation of wind pressure coefficients along the roof centerline for 0° wind direction; b) Variation in wind pressure coefficients along the line at the concurrent edge for 45° wind direction	84
Figure 5-20 Comparison of extreme peak and mean pressure coefficients on the windward edge zone and corner zone between the present study and Alrawashdeh and Stathopoulos (2015)	85
Figure 5-21 Contour plots of peak pressure coefficient at 45° wind direction; A) Present study, B) Alrawashdeh and Stathopoulos (2015)	86
Figure 5-22 Comparison between the present study and Jesson et al, 2015. a) Variation of wind pressure coefficients along the roof windward edge; b) Variation in wind pressure coefficients along the line at the concurrent edge 45° wind direction	88
Figure 5-23 Comparison of mean pressure coefficients along the roof centerline for 0° wind direction between the present study and the previous downburst wind studies	89

List Of Tables

Table 1-1 Fujita Scale (F-scale)	3
Table 1-2 Enhanced Fujita Scale (EF-scale)	3
Table 3-1 Recommended Tornado Factor (TF), after (ASCE 7, 2017).....	40
Table 4-1 Testing configurations in each trial	48
Table 4-2 Dimension details of Trial 4 configurations	55
Table 4-4-3 Dimension details of Trial 5 configurations	57
Table 5-1 Downburst physical simulation characteristics of the previous studies.....	68

Chapter 1. Introduction

1.1 Overview

Severe thunderstorms (i.e., downbursts and tornadoes) have extreme damaging effect, especially in suburban areas. According to the National Oceanic and Atmospheric Administration (NOAA), there is an increase in the number of losses due to the increase in the intensity of storms. In fact, there were 1075 reported tornadoes by the end of 2020 compared to 1517 tornadoes in 2019 in USA, the increase in the intensity of these storms caused 76 human life losses in 2020 compared to 41 human life losses in 2019.

In the last few years, it was noticed that the weather climate change has played the main role in the increase of the probability of occurrence of severe wind events (i.e., downbursts and tornadoes). In fact, the climate change and global warming could increase the convective potential energy, which would decrease the vertical wind shear. Thus, this would produce more tornadoes and downbursts (Doswell et al., 2012). Over the past 60 years, the interest in understanding of the storm characteristics has been increasing. Fujita (1981) improved our understanding of thunderstorms and classified the high wind speeds in order: (1) Tornado, (2) Downburst, (3) Straight-line wind. That is to say that this order represents the level of damaging effects each high wind have.

Tornadoes are rotating columns of rising air creating a low-pressure area close to the ground and draws air radially. Tornadoes have very complex flows because they are unsteady, three-dimensional, and turbulent nature (see Fig. 1-1). Tornado intensity is measured by the so-called Fujita-scale (F-Scale) enacted by Theodore Fujita in 1971. As shown in Table 1, F0 is the low damage intensity and F5 is a severe damage intensity. Afterwards, McDonald submitted to The National Weather Service of the United States a scale named to Enhanced Fujita (EF-Scale), as shown in Table 2 (McDonald et al., 2006). The new (EF-Scale) was made to improve the (F-Scale) in terms of the damage indicators (DI) consideration. Also, the degree of damage (DOD) for each indicator. On the other hand, (Lombardo et al., 2015) noted that a reassessment is necessary to

improve EF-scale due to the lack of validation with real tornado events. Thus, the damage indicators and the degrees of damage should be enhanced to increase the safety against tornadoes.

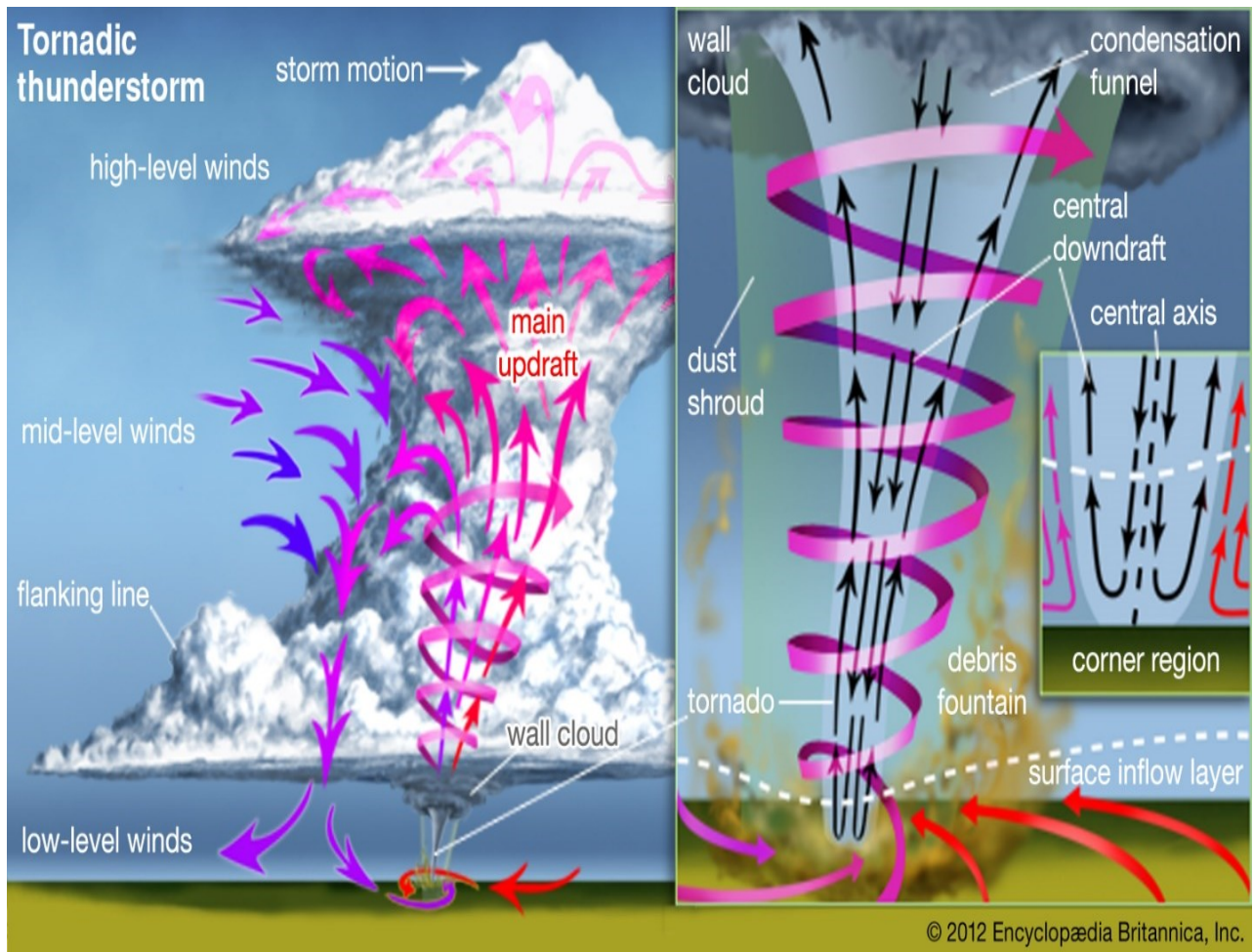


Figure 1-1 Real tornado characteristics, Image source: from Encyclopedia Britannica, Inc.
<https://www.britannica.com/science/tornado/Physical-characteristics-of-tornadoes>

Table 1-1 Fujita Scale (F-scale)

Fujita Scale (F-Scale)	Wind Speed (km/h) 3s gusts
F0	64-116
F1	117-180
F2	181-253
F3	254-332
F4	333-418
F5	419-512

Table 1-2 Enhanced Fujita Scale (EF-scale)

Enhanced Fujita Scale (EF-Scale)	Wind Speed (km/h) 3s gusts
EF0	105-137
EF1	138-178
EF2	179-218
EF3	219-266
EF4	267-322
EF5	>322

Downburst events are generated from the downdraft thunderstorm where the moist air is drawn upward in the updraft and subsided into the downdrafts. As shown in Fig. 1-2, which shows the development of the downbursts. Fujita (1985) assumed that this cycle would continue to be strengthened, and it would impact the buildings in a disastrous manner. Fujita classified the downburst as micro-burst if the wind damage is within 4 km and macro-burst if greater. Figure 1-3 shows the differences in the characteristics of the horizontal velocity distributions between the microburst phenomena with the typical atmospheric boundary layer flow.

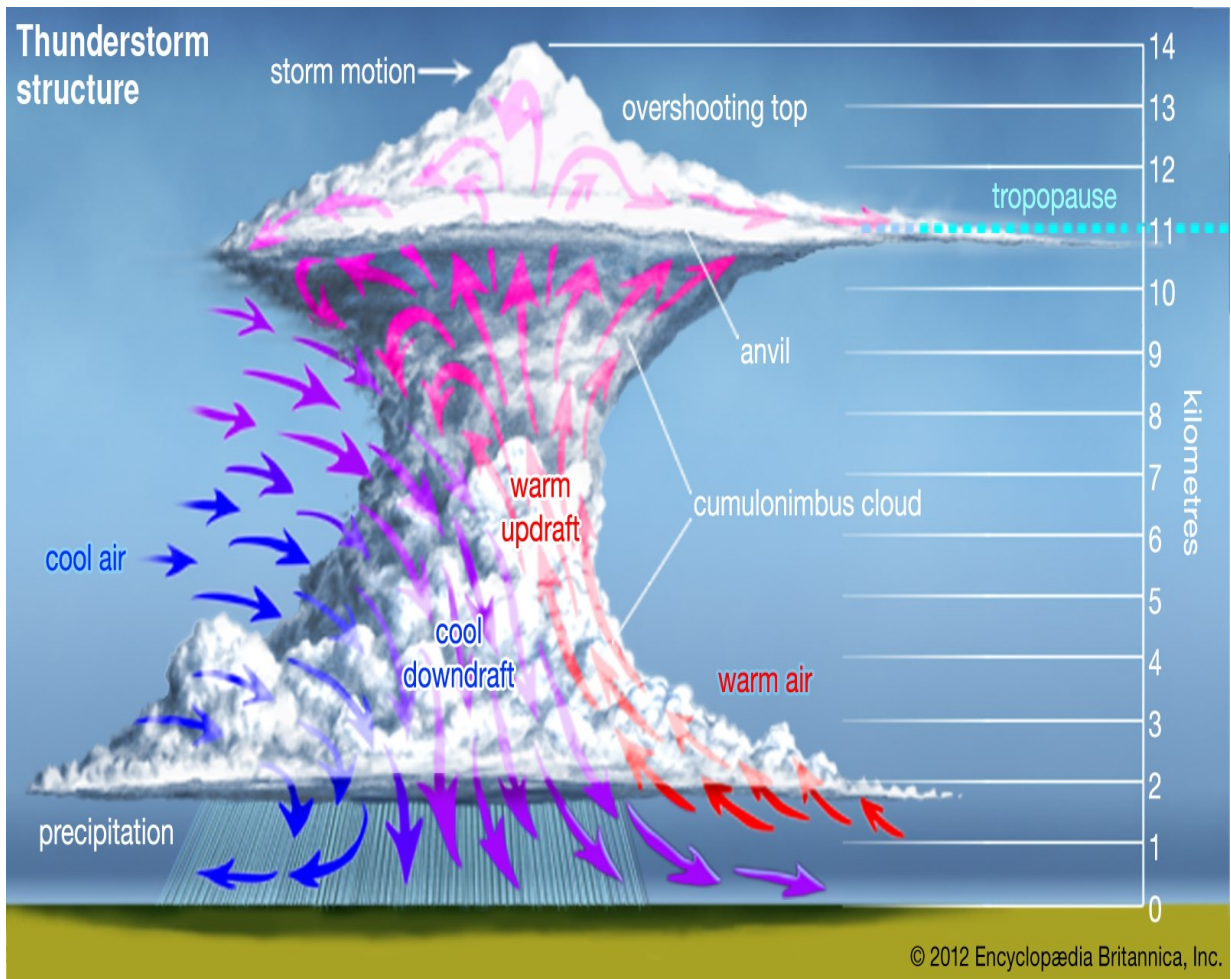


Figure 1-2 Downdraft characteristics, source. Britannica,
<https://www.britannica.com/science/updraft>

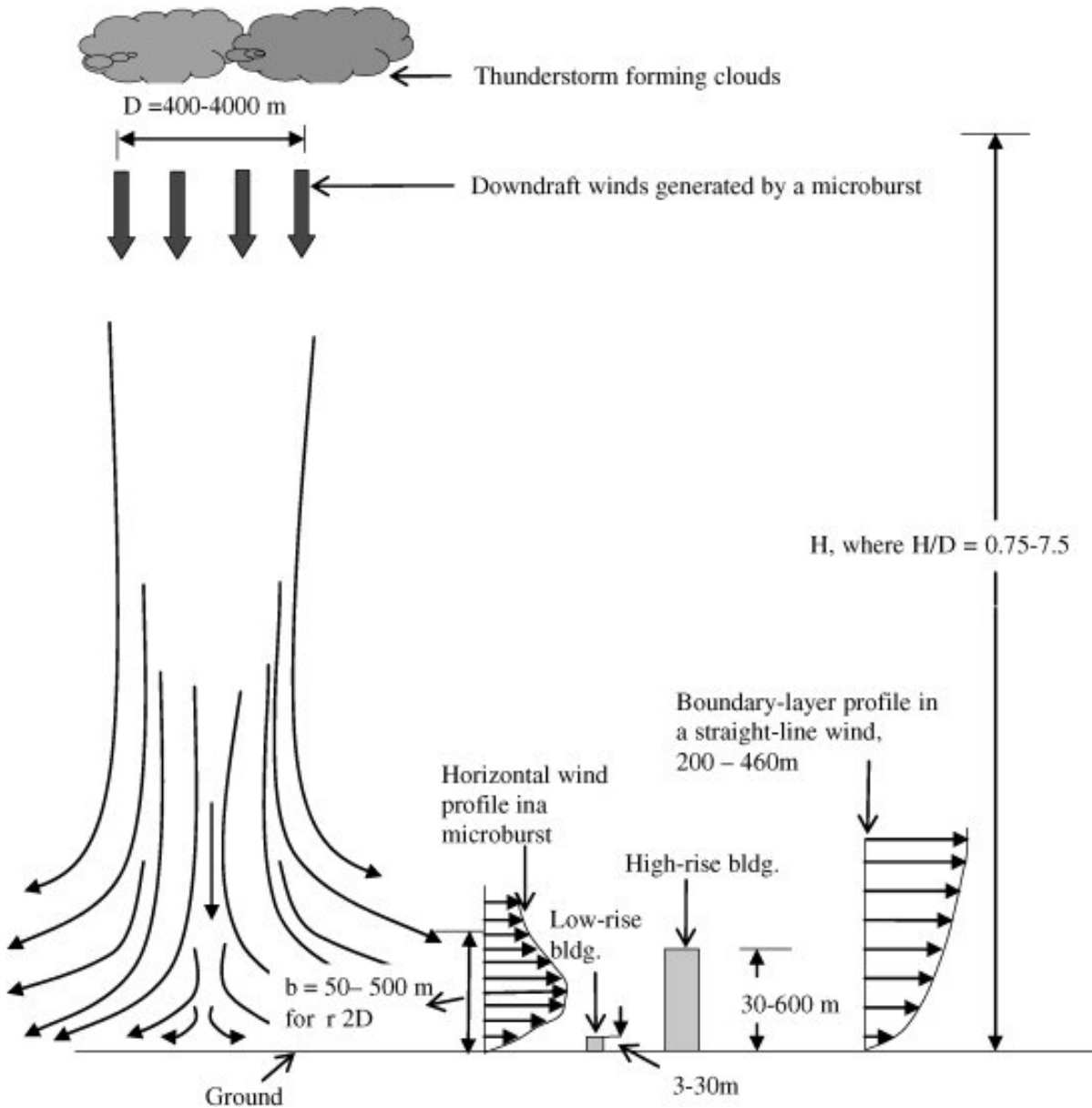


Figure 1-3 Characteristics comparison of horizontal wind profile in a straight-line with microburst, after Sengupta and Sarkar, (2008)

Several studies have investigated the effect of tornadoes and downbursts on low-rise buildings to understand the wind field characteristics of the phenomena and the aerodynamics. Low-rise buildings located in a suburban area are most severely affected by thunderstorms. Limited knowledge exists on the wind loads on low-rise buildings. Compared with an enormous number of studies on wind loads of strong straight-line ABL winds, e.g. Hatem Alrawashdeh and

Stathopoulos (2015), Stathopoulos and Saathoff (1991), there is only a limited number of studies addressing the effects of non-synoptic winds on structures. Such studies were used to develop the current wind standards and codes.

The current wind codes and standards (American Society of Civil Engineers, ASCE7; National Building Code of Canada, NBCC) provide good guidance to the structural design engineers to determine the wind pressure on a particular building due to the boundary layer winds (synoptic winds); on the other hand, little guidance for non-synoptic winds is provided to the designer to evaluate the wind load effects.

The ASCE 7 (2016) provides a section in the Commentary (C26.14) to increase the protection of buildings, in case of tornado impact. A safe room design procedure was included to protect the occupants of a building not designed to resist the effect of tornadoes; like hospitals or other buildings that their occupants cannot leave their place in an emergency case (FEMA, 2015). However, downbursts are not considered in ASCE7-16.

The NBCC (2015) defines three tornado-prone regions. These regions could experience tornado events based on the phenomena intensity and its probability of occurrence. The code also mentions that the construction details of buildings should be adequate, so that these buildings are protected against the damaging effects of tornadoes. Similar to ASCE 7 (2016), the Canadian code does not consider the downbursts.

1.2 Thunderstorm Damage

Thunderstorms are the most powerful phenomena that cause huge damage and losses in life, structures, and public infrastructure, and every year the number of losses either physically or financially increase. Figure 1-4 shows the severe damage of several buildings due to a tornado. This event was the most recent deadliest tornado in the last decade in North America. It occurred in May 2011, when a tornado with an intensity scale of EF5 crossed Joplin, Missouri, where it caused 158 fatalities. It was also the costliest event estimated to cost around \$2.8 billion in damage.



Figure 1-4 Joplin tornado damage in Joplin, Mo, May 2011, source:
<https://www.theatlantic.com/photo/2011/05/tornado-damaged-joplin-from-above/100073/>

Figure 1-5 presents a downburst event that occurred in Minnesota in 2011. Since damage with a horizontal dimension of more than 4 km affected the trees, the event was a macroburst.



Figure 1-5 Macroburst trees damage occurred in Minnesota in 2011, source: <https://www.nssl.noaa.gov/education/svrwx101/wind/types/>

1.3 Scope and Objectives

This thesis aimed to compare the previous work and expand our knowledge and understanding of both thunderstorm phenomena (tornado and downburst). The objectives of the present study can be described as follows:

1. To summarize and understand the differences of the current facilities that are capable to simulate these phenomena.
2. Due to the complexity of the nature of the phenomenon flow and due to the scarcity and the lack of the full-scale data, to make a comparison of the wind field flow of tornado and

downburst events with different simulation characteristics and facilities in order to understand the damaging effects of each flow parameter.

3. To simulate a downburst phenomenon in the boundary layer wind tunnel.
4. To compare the experimental findings of the present study (speed profile, wind load) with the ABL full-scale measurements and downburst previous studies.
5. To compare the load distribution of the thunderstorms with the boundary layer flow experiments to assess the relation in between.
6. To examine different configurations at the atmospheric boundary layer wind tunnel that could help to assess the variation of the ABL wind loads and the thunderstorm wind loads.

1.4 Thesis Outline

The following chapter presents a general review of the previous studies and physical simulation of non-synoptic wind facilities over the world. It discusses the phenomena creation concepts and the development of the simulators including their advantages and disadvantages.

Chapter 3 presents the boundary layer wind tunnel of Concordia University details. The simulation of terrain exposures in the wind tunnel is presented, as well as the wind tunnel modifications to achieve the trend of non-synoptic wind speed profile.

Chapter 4 presents the experimental analysis and results of the present study and compares the present study findings with the ABL and downburst previous studies.

Chapter 5 discusses the wind codes and standards that consider the non-synoptic winds.

Finally, Chapter 6 provides the summary and conclusion of the present study and addresses future work recommendations.

Chapter 2. Non-synoptic winds

Near-surface flow characteristics of tornadoes and downbursts are more interest to researchers. Therefore, it is important to develop a credible simulation. The current chapter reviews the previous work, the development of the available simulators and the description of their simulation characteristics.

2.1 Tornado

2.1.1 Previous work (Physical characteristics - Available facilities)

The tornado flow generated in the simulators can be controlled dynamically and geometrically. Lewellen (1962) defined three dimensionless parameters that govern the flow structure of simulated tornadoes: (i) aspect ratio (geometric parameter defined in Eq. 2.1), (ii and iii) swirl ratio and Reynolds number (kinematic parameters defined in Eq's 2.2, 2.3 and 2.4).

Aspect ratio (a):

$$a = \frac{h}{r_o} \tag{2.1}$$

where h is the inflow height and r_o is the updraft radius, as shown in Fig 2-1.

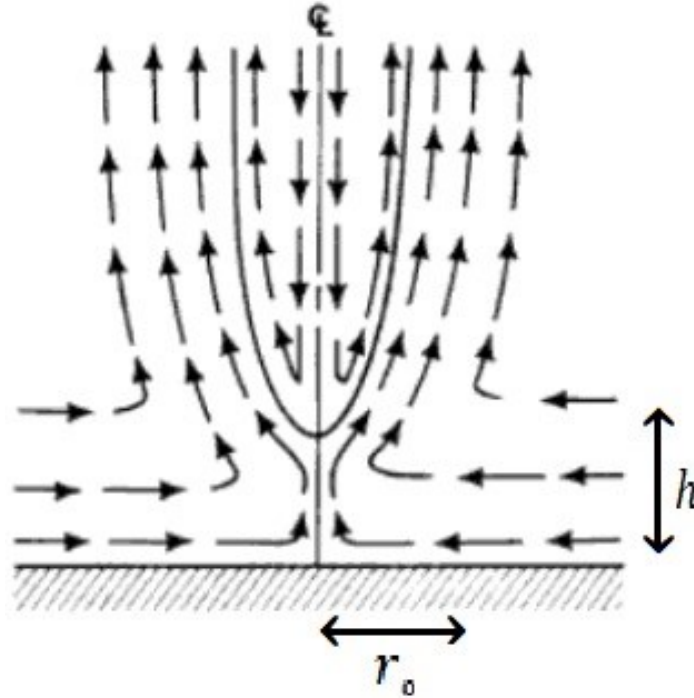


Figure 2-1 Schematic diagram of tornado showing the aspect ratio parameters (Davies-Jones, 1986)

Kinematic parameters (S and Re_r):

The swirl ratio (S) is the ratio of the angular momentum to the radial momentum of the flow, and can be calculated using the following equations:

$$S_v = \frac{\tan \theta}{2a} \quad 2.2$$

$$S_c = \frac{\pi r_c^2 V_\theta}{Q} \quad 2.3$$

where θ is the vane angle, r_c is the core radius at the maximum tangential velocity, V_θ is the maximum tangential velocity, Q is the volume flow rate, and S_v is the swirl ratio. Equation 2.2 is based on geometry (S_v) and is widely used for ward-type simulators due to its simplicity. However,

the swirl ratio may be alternatively calculated from the flow during the simulation, as per Eq. 2.3 (S_c , Haan et al., 2008).

Reynolds number:

$$Re_r = \frac{\dot{Q}}{2\pi\nu} \quad 2.4$$

Here, \dot{Q} is the volume flow rate per unit length and ν is the kinematic viscosity.

The tangential velocity profile of different simulation environments is presented in Figure 2-2. Here, the tangential velocity (V_θ) is normalized by the maximum tangential velocity ($V_{\theta max}$), while the radial distance from the core center (r) is normalized by the radius where the maximum tangential velocity occurs (r_c). Figure 2-2 shows that the tangential velocity profiles measured by (Haan et al., 2008; Razavi and Sarkar, 2018; Wang et al., 2017) follow the same trend and in particular, are in good agreement inside the core boundary ($r/r_c < 1$). The tangential velocity increases with the radial distance from the center and reaches its maximum at the core boundary ($r/r_c = 1$). Outside the core radius ($r/r_c > 1$) the tangential velocity decreases and the matching of the four considered profiles is less good. Such variance may be attributed to the different simulation parameters used in each study. Moreover, Church et al. (1979) and Davies-Jones (1973) observed that for a large radial Reynolds number, the flow characteristics of tornado vortices are independent of Re_r but highly dependent of the swirl ratio, S . Furthermore, the studies showed that the swirl ratio and the core radius are independent from the aspect ratio. The core radius is a function of the swirl ratio and increases with the swirl ratio. Recently, Refan and Hangan (2016) confirmed the abovementioned observation.

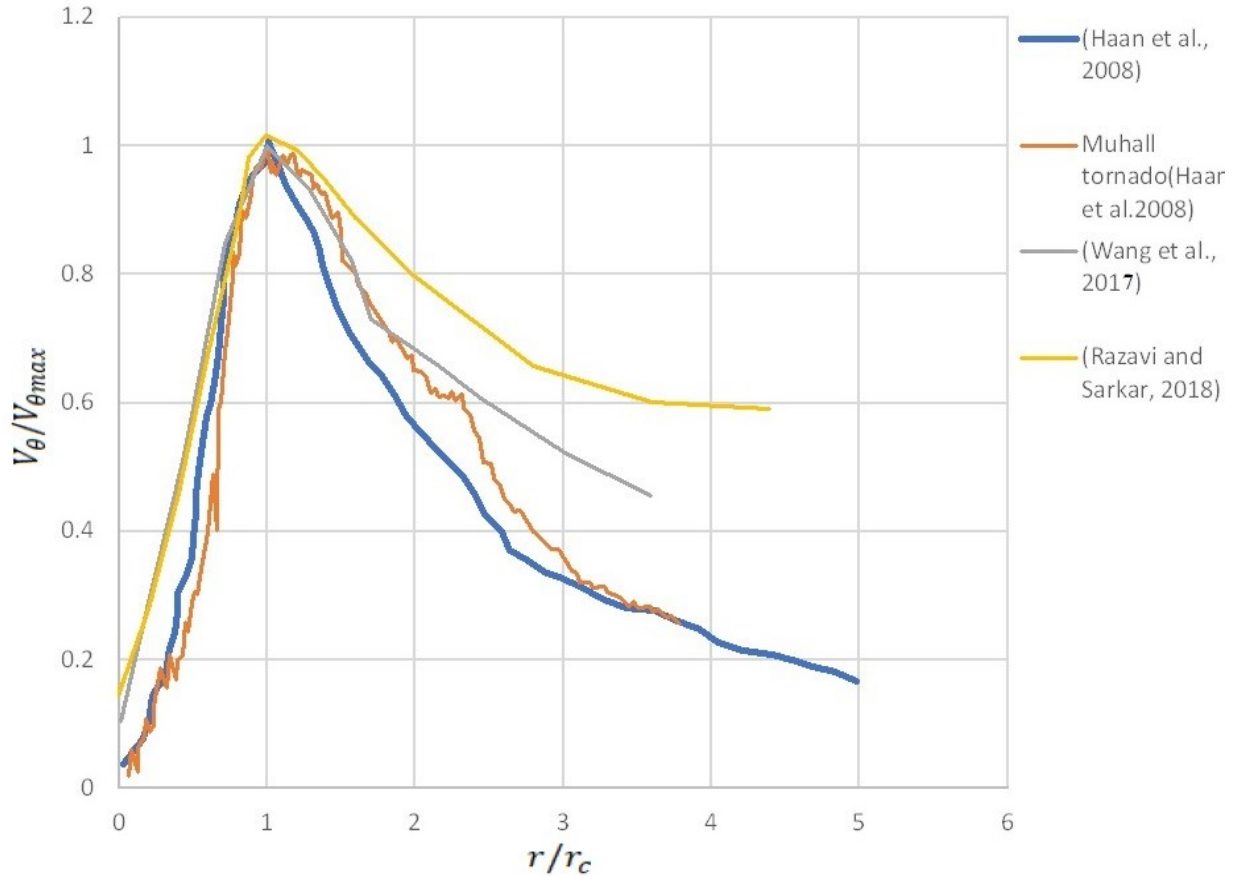


Figure 2-2 Comparison of scaled tangential velocity profiles for laboratory tornado and the Mulhall radar data (Haan et al., 2008)

A limited number of studies investigated the aerodynamic effects of tornadoes on buildings. In the last decade, most of these studies focused on the flow field characteristics of near ground tornadoes in the presence of buildings, aiming to identify the differences between tornado and ABL flows. Mishra et al. (2008) examined the influence of a simulated stationary tornado on the pressure distribution on a 30mm cube building. It was found that the pressure is significantly high when using tornado vortices flow instead of atmospheric boundary layer flow. Sengupta et al. (2008) used a cube and a tall building to quantify the influence of the translation speed, building orientation and core radius on the wind load. The study showed that the tornado translation simulation results to higher wind load compared to the case of straight-line flow and that the increase in the translation speed may affect the wind load. Also, the cube experienced a higher

uplift force at 0° wind direction compared to the case of 45° . Haan et al. (2010) investigated tornado-induced loads on a gabled roof building of 30° pitch, under the effect of a translating tornado generated at the ISU simulator. The authors compared the results with ASCE7-05, and showed that the uplift forces exceed the standard values by a factor of 1.8-3.2. Hu et al. (2011) tested a gabled roof building with a roof angle of 35° at the ISU simulator, focusing on the effects of the building orientation and the radial location from the core center. The study found that the maximum lift force coefficient occurred at building orientation $15^\circ - 30^\circ$, taking values 3 times higher than the ones provided at the ABL. Sabareesh et al. (2012) studied the effect of building location and ground roughness using a 25mm cube building model. The differences in the obtained pressure coefficients were negligible when increasing the ground roughness from 5 mm to 10 mm. Case et al. (2014) tested buildings of different geometry in the ISU simulator, aiming to examine the effect of the building shape on the tornado flow. The authors found that the building parameters (i.e. eave height, roof angle, etc..) have the most significant influence on the pressure coefficients. Cao et al. (2015) published the first study that examined the wind loads on a cooling tower using Tongji university simulator. The study demonstrated that the pressures caused by tornadoes are higher than the ones due to the boundary layer flow. Wang et al. (2018) investigated the tornado-induced pressures on a 50 mm cube model using the Tongji university simulator. The effects of the building opening on the pressure were measured and compared to the ASCE 7-10 and GB 50009-2012. The reported results showed that the effect of the opening ratio on the external pressure coefficients is negligible, whereas the effect of the opening ratio on the internal pressure coefficients is significant.

In (Haan et al., 2010; Hu et al., 2011; Sabareesh et al., 2012) the reference pressure that was used to calculate the pressure coefficient was measured far away from the tornado simulator. Instead, Mishra et al. (2008) used the mean static pressure on the ground surface as the reference pressure. Moreover, some studies use the maximum horizontal velocity as the reference velocity, while others use the maximum tangential velocity at the building height. The lack of a universal definition of the reference pressure amongst the studies, makes their quantitative comparison impossible.

2.1.2 Review of facilities

Physical simulation of wind is very important to improve, and it is also important to understand the characteristics of the phenomenon. The development of the simulation facilities reviewed in this section started over 50 years ago.

Tornado Vortex chamber (TVC) simulator

Ying, S. J., and Chang (1970) developed and designed the first tornado simulator using the basic structure of tornadoes, which are the near ground inflow layer and the vertical updraft. Afterwards, Ward (1972) improved the simulator design and introduce the Tornado vortex simulator (TVC), well-known as Ward-type simulator (see Fig 2-3). The TVC Contains three flow main regions:

- 1) Confluence region: the lower (outer) region surrounded by a rotating mesh wire provides net vertical vorticity and a radial inflow.
- 2) Convergence region: this region receives the inflow flux with the conservative angular momentum to develop significant tangential and axial velocities. It also feeds the column of swirling that forms at the region's center.
- 3) Convection region: the swirling column extends through this region.

However, the main disadvantage of the TVC simulator is that the flow measurements inside the chamber are difficult to measure, due to the access limitation. This led to a development of the simulator (Church et al., 1979). Using the fan at the top of the simulator, and the swirling at the bottom, the flow rate and the tangential velocity can be controlled independently.

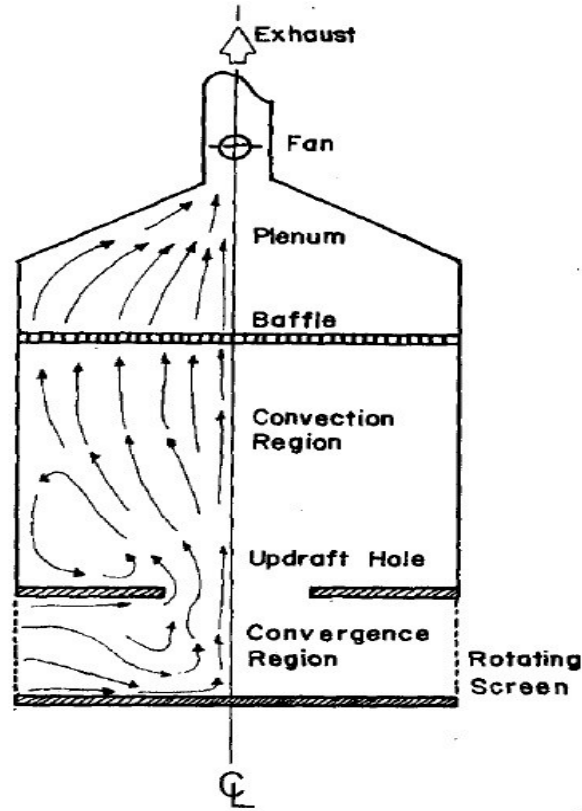


Figure 2-3 Schematic diagram of tornado vortices chamber (Church et al., 1979)

Purdue University simulator

Figure 2-4 shows the Purdue university simulator. This simulator was designed based on the TVC Simulator Concept with some modifications to allow independent control of the dynamic and geometric dimensionless parameters (Aspect Ratio, Reynolds number, and swirl ratio), while the inflow depth and the updraft radius are adjustable. geometric dimensionless parameters (Aspect Ratio, Reynolds number, and swirl ratio), while the inflow depth and the updraft radius are adjustable.

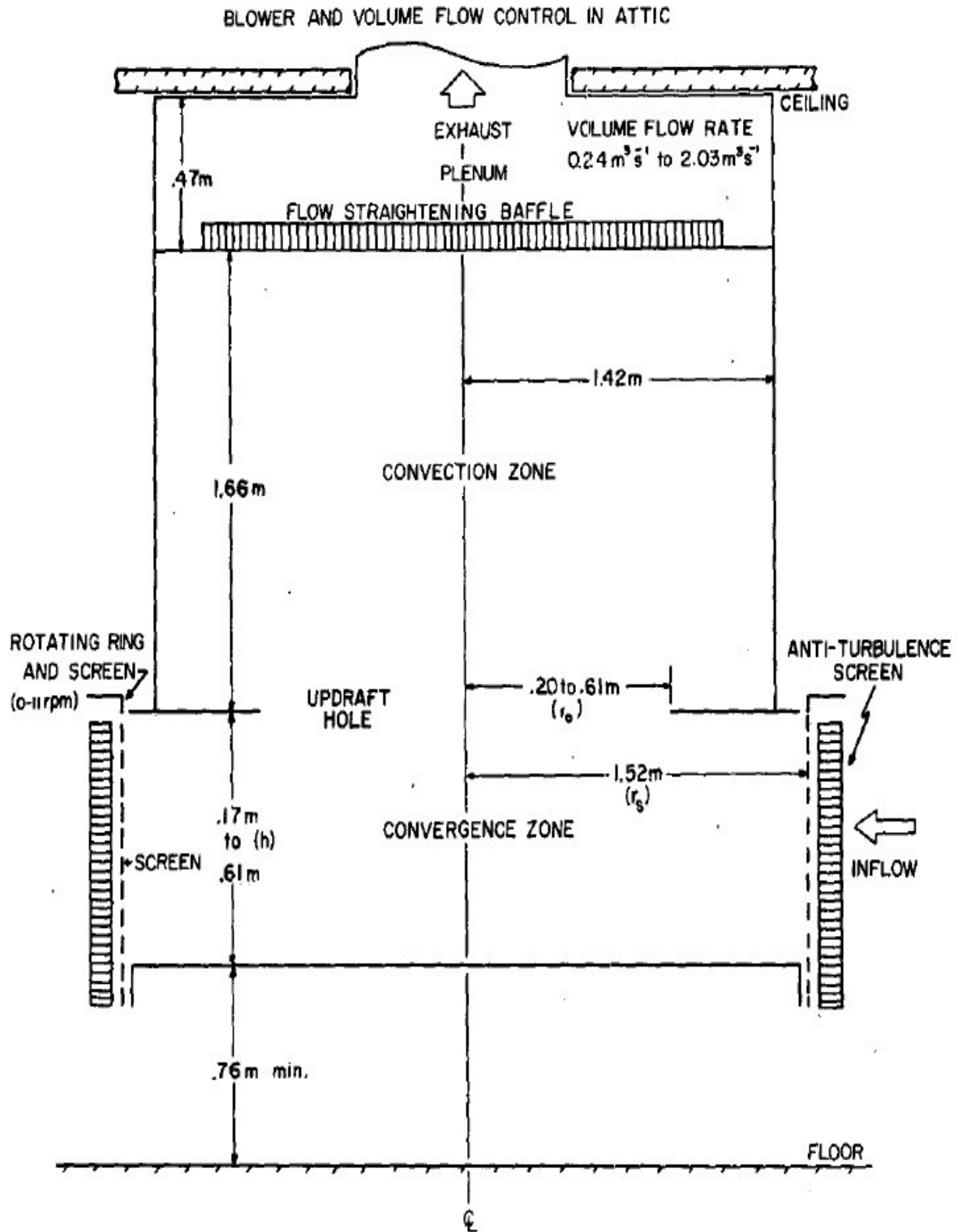


Figure 2-4 Schematic diagram of Purdue university simulator (Church et al., 1979)

Texas Tech University simulator

The Texas Tech University simulator (TTU) is a ward-type simulator designed in 2001 and modified by Mishra et al. (2008). The modified TTU (TTU -VSII) was the first simulator to be used in wind engineering applications. Mishra et al. (2008) used a small building to investigate and evaluate the mean surface pressure. In this simulator, the updraft flow is provided by a blower connected with the convective region, while the mesh wire is replaced by sixteen slotted jets. Therein, the inflow height is adjustable from 0.06m to 0.19m to control the aspect ratio. The updraft hole radius is 0.19m. Furthermore, the simulator can control the flow and the swirl ratio using a vortex blower connected at the base (see Fig. 2-5. A). The main disadvantage of TTU -VSII is that it considers a very large model scale.

Subsequently, Texas Tech university built a new large-scale ward-type simulator named VorTECH (see Fig. 2-5.B). The VorTECH simulator has eight fans at the top and 64 turning vanes mounted at the chamber periphery walls, which control the swirling intensity. The chamber diameter is 10.2 m, and the updraft hole diameter is 4 m. The aspect ratio may vary while the inflow height is adjustable up to 2 m. The VorTECH simulator solves the scaling issue of TTU -VSII by using an updraft radius which is ten times larger than one in TTU -VSII. Furthermore, this model can simulate a translation tornado with the floor moving at a speed up to 1.5 m/s.

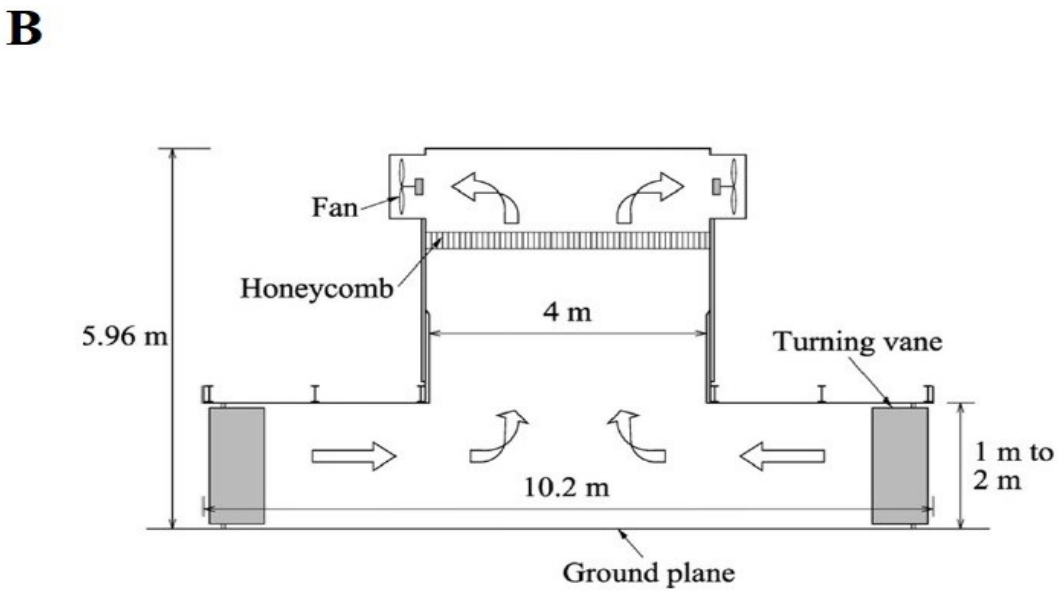
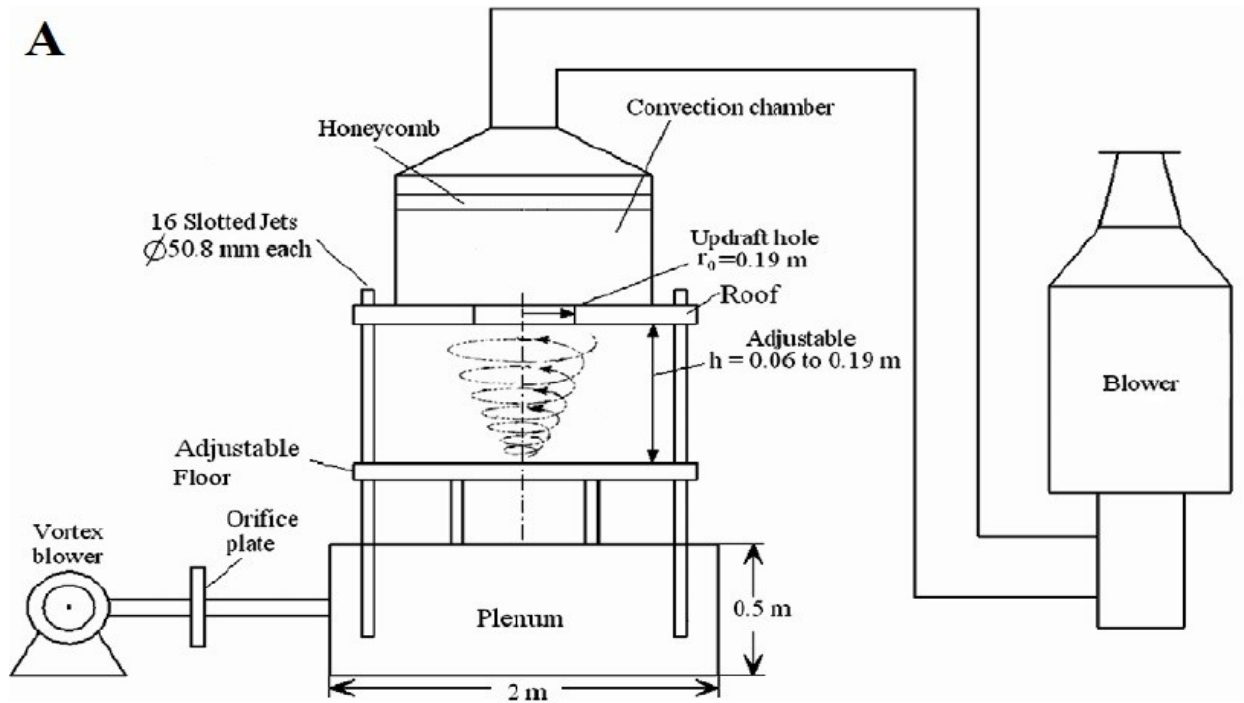


Figure 2-5 Schematic diagram of Texas tech university simulators A) TTU -VSII ((Amit R. Mishra et al., 2008) and B) VorTECH (Tang et al., 2018)

IOWA University simulator (ISU)

The IOWA University simulator was designed to meet two requirements (i) generate a translation tornado, and (ii) meet the geometry requirements and accommodate a building model to measure the building loads. It was the first simulator to have these features, using a crane at the top that can be translated horizontally at speeds up to 0.61 m/s. A fan of diameter 1.83m that can provide a maximum flow rate of 40 m³/s is mounted at the top, inside the circular duct. This facility uses the rotating forced downdraft concept, which is different than the concept of ward type simulators. The inflow feeds from the updraft flow using vans that provide the rotating force (see Fig 2-6). Note that this facility has a visualization difficulty of the structural details of tornado near the ground, due to the large vortex scale that can be generated by the large-scale simulator. Thus, a small facility named as MINI-ISU simulator was built to overcome this limitation and visualize the development of the vortices at different swirl intensities. Both the ISU and MINI-ISU facilities follow the same configuration concept but have different geometric scales as shown in Fig. 2-7.

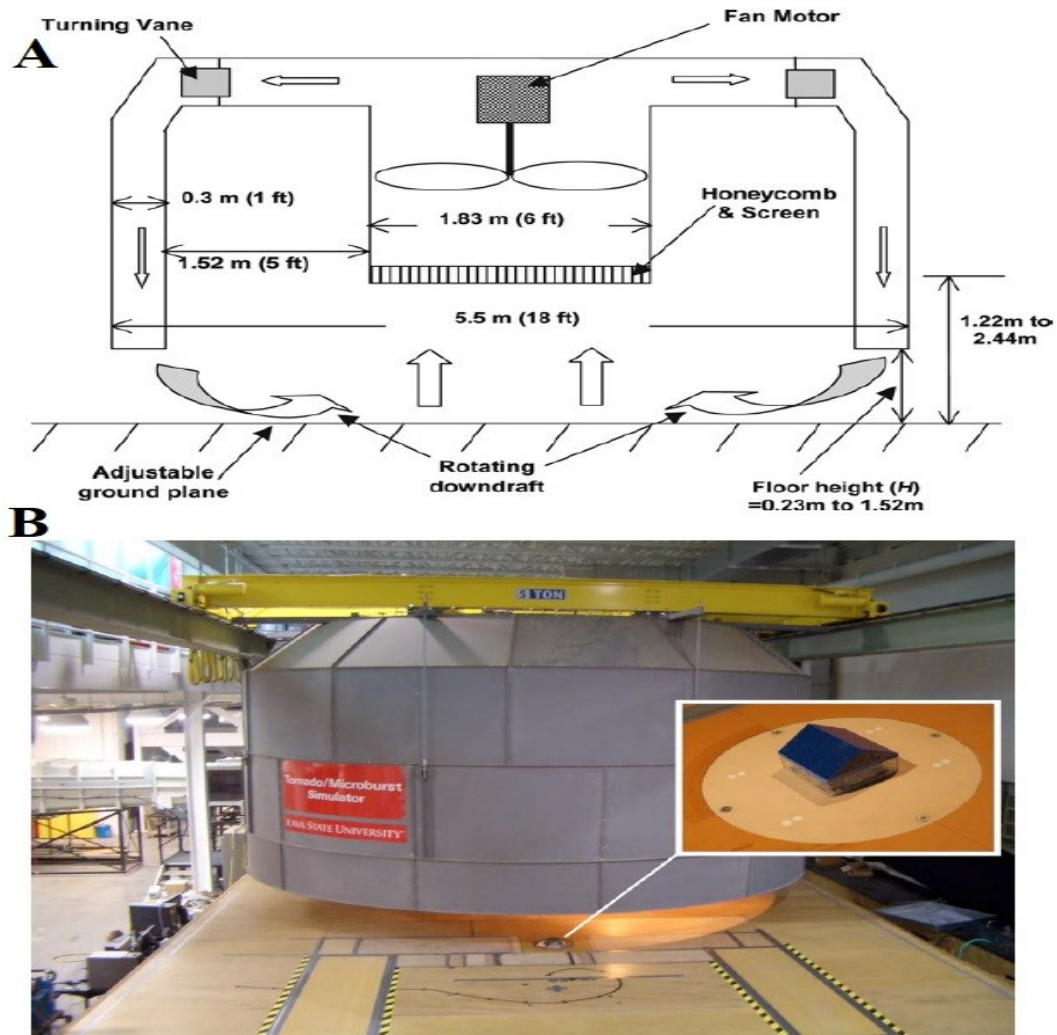


Figure 2-6 ISU Simulator A) Schematic diagram (Haan et al., 2008) and B) photo of circular duct (Haan et al., 2009)

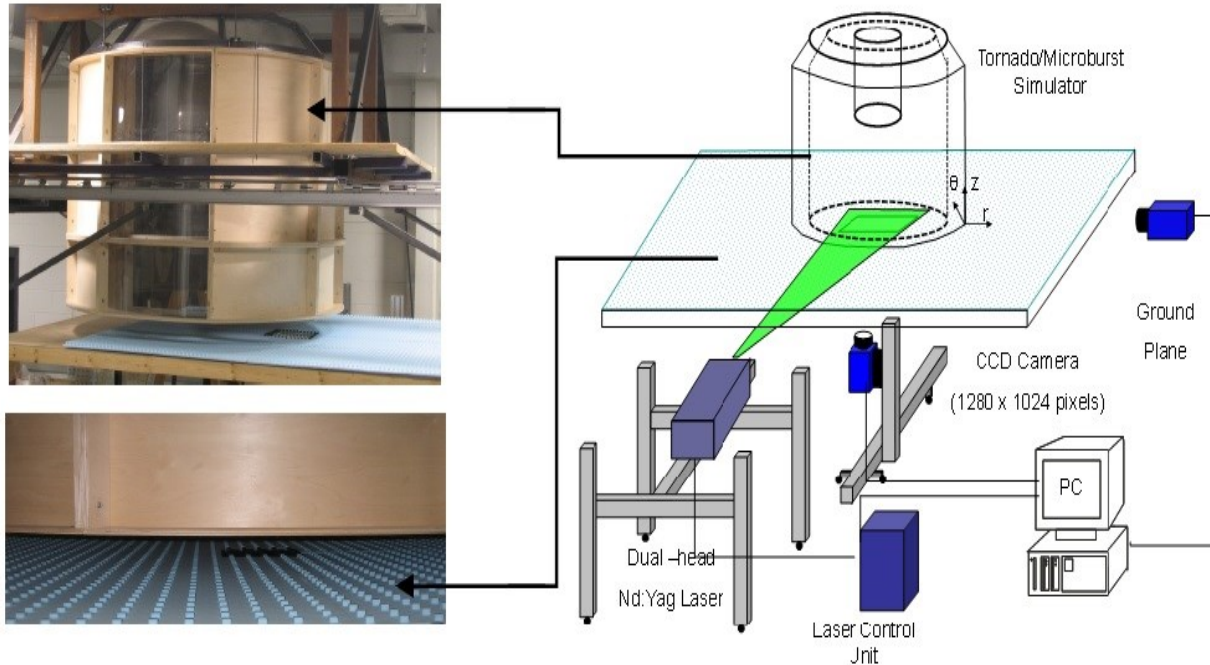
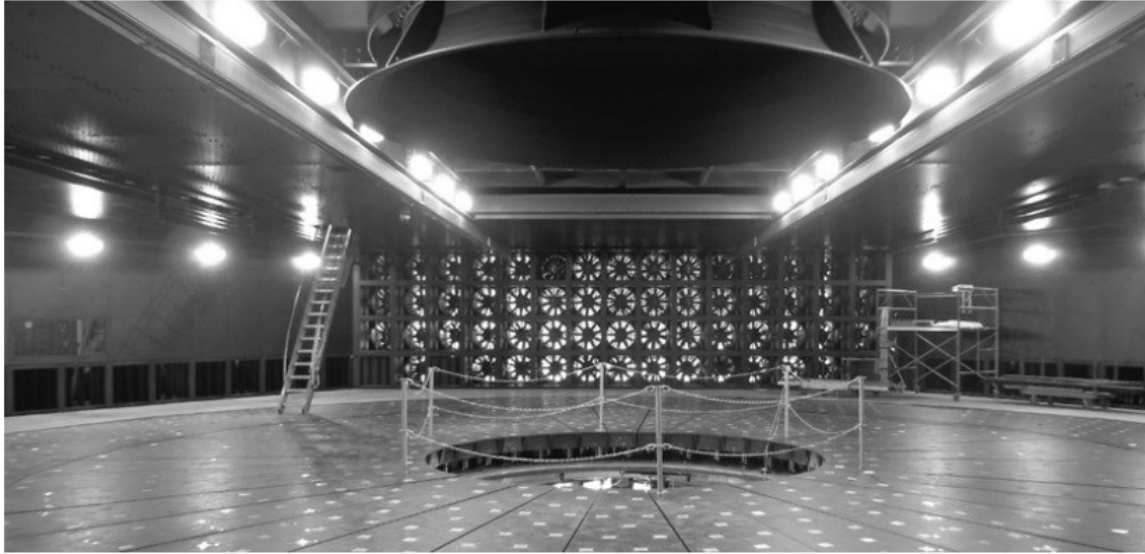


Figure 2-7 MINI-ISU simulator

The WindEEE Dome

The WindEEE Dome was constructed and designed at Western University. The simulator contains a hexagonal chamber with a diameter of 40 m, 8 fans mounted on the 6 sidewalls of the chamber and 6 fans mounted at the top, which can produce inflow or outflow through the bell-mouth (see Fig. 2-8). Tornado phenomena can be produced using two different generation methods. The first method is by producing an updraft flow using the top fans and wall vanes to generate swirl flow; the circular diameter in this case can vary from 0.6 m to 1.2 m. The second method is using the wall fans to provide inflow and the top fans to provide suction; the circular diameter in this case is at most 2.3 m. Also, the updraft hole diameter can vary between 0.14m to 0.4 m. The WindEEE Dome facility can produce translations with an associated speed of 2 m/s, whereas the swirling intensity may be controlled by the vane angles (Hangan, 2014).

A



B

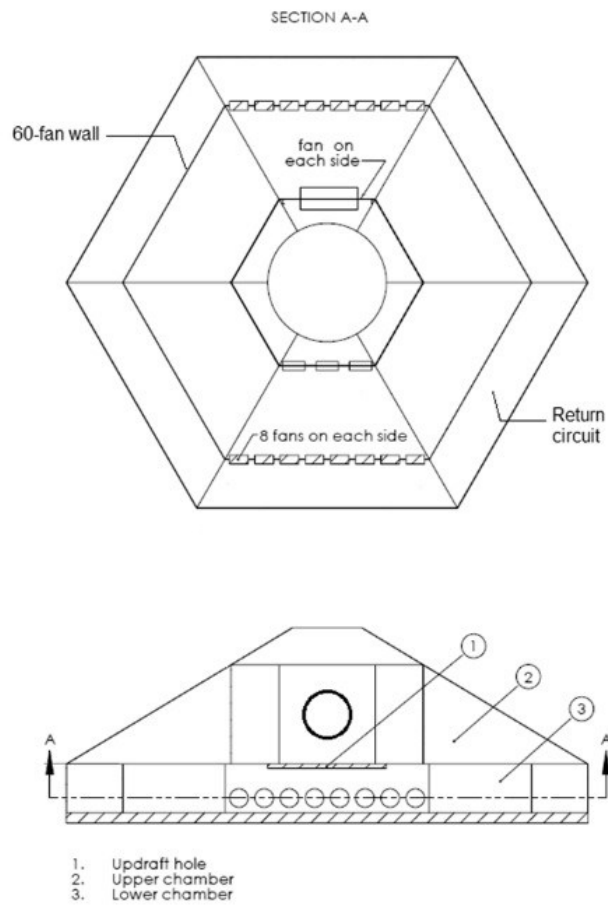


Figure 2-8 A) photo of the multi-fan system and B) Schematic diagram of WindEEE Dome, after (Hangan, 2014)

Tongji university simulator

A small-scale simulator was designed and constructed at Tongji university using the same configuration concept of the IOWA university simulator. A single fan mounted at the top of the circular duct is used to generate updraft flow with a maximum flow rate of $4.8 \text{ m}^3/\text{s}$. The updraft hole diameter is 0.5 m , and the test floor height can be adjusted between 0.15 m to 0.55 m to obtain the desired aspect ratio (see Fig. 2-9). The Tongji University Simulator facility can generate a stationary tornado.

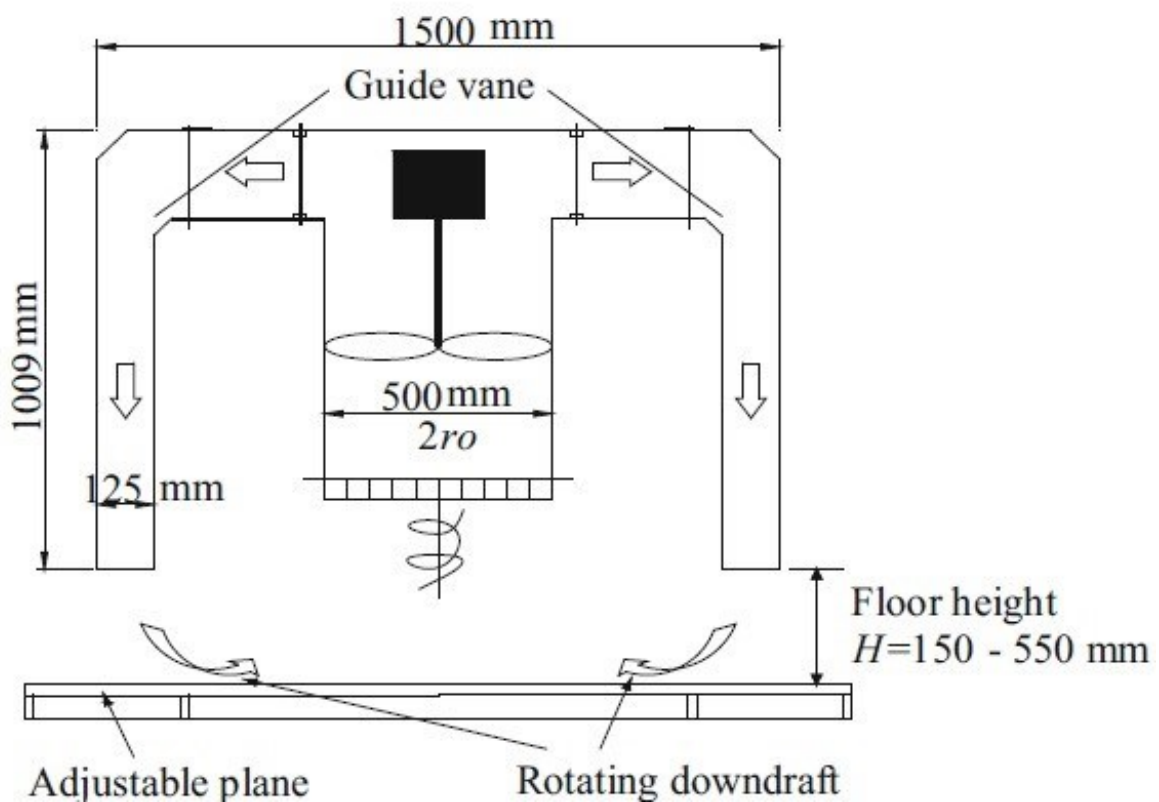


Figure 2-9 Schematic diagram of Tongji university simulator, after (Cao et al., 2018)

Tokyo Polytechnic University Simulator

A ward-type tornado simulator was developed at Tokyo Polytechnic University, with a diameter of updraft hole equal to 0.6m and an inflow height of 0.3m. the inflow height may be adjusted up and down to obtain different aspect ratios. The Tokyo Polytechnic facility can generate a stationary tornado, where the updraft flow is generated independently by a fan, which is mounted at the top of the convection region (see Fig. 2-10).

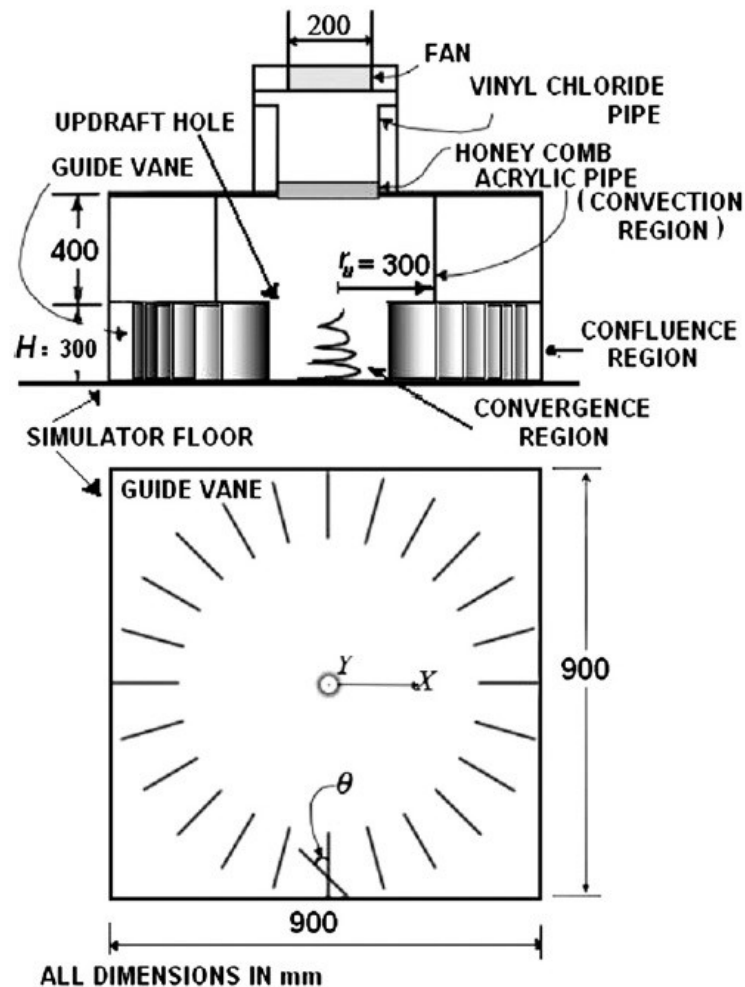


Figure 2-10 Schematic diagram of tornado simulator at Tokyo polytechnic university, after (Sabareesh et al., 2012)

2.2 Downburst

2.2.1 Previous work (Physical characteristics - Available facilities)

The physical simulation of downburst is simpler than the one of tornado. Two models can produce the downburst; the first model is the impinging wall jet model which is widely used because of its simplicity in reproducing downburst. The jet blows the air to produce radial outflow and ring vortex. The second model is the cooling source that uses a dense fluid dropping into a lower density fluid. This approach allows the formation of the negative buoyancy that leads to forming the ring vortex. The second model has geometric and velocity scaling limitation when used in wind engineering applications.

Initially, downburst simulation was limited to meteorological applications. Few studies investigated the pressure distribution of downburst phenomena on a particular structural model. Chay and Letchford (2002) investigated the pressure distribution of downburst in the presence of a cubic model (30mm*30mm) using a stationary impinging wall jet at the Texas Tech university simulator (TTU). The same building model and facility was used to simulate a translational downburst (Letchford and Chay, 2002). Mason et al. (2009) upgraded the TTU simulator and examined the effect of the pulsed jet on the building model used previously by Chay & Letchford's. Sengupta et al. (2008) conducted laboratory experiments using a translational impinging wall jet at the IOWA university simulator (ISU). This study examined the flow field and the resulting pressure on a cubic model. Zhang et al. (2013) was the first study to investigate the pressure distribution on a gabled roof building. Moreover, Zhang et al. (2014) investigated various building shapes using a steady impinging jet. Jesson et al. (2015) studied the effects of the downburst on two different building shapes using the impinging wall jet simulator at the University of Birmingham (UoB-TWS). Jubayer et al. (2016) examined the downburst-induced pressure distribution on a low-rise gabled roof building. The authors conducted a stationary simulation at WINDEEE dome in Western University, to investigate the effect of the building orientation and radial location on wind load. Lombardo et al. (2018) in Texas Tech, evaluated the wind load on the WERFL building due to a full-scale downburst event. Note that the abovementioned study considered different definitions for the reference pressure coefficient. Asano et al. (2019)

investigated the effect of the downburst on a flat-roof building using pulsed and moving simulation mechanisms, used separately and simultaneously at Tohoku University. Iida and Uematsu (2019) conducted experiments to compare the pressure distributions from ABL and downbursts.

Most of the previous studies examined the flow characteristics at a different radial location from the center of the downburst. These studies demonstrated that the radial location is the key parameter in changing the flow fluctuation. All of the studies that investigated the downburst wind flow near the ground, agree that the downburst phenomena have different characteristic from the boundary layer wind flow, where the wind speed reaches the maximum at a low height (near the ground) and starts decreasing and fluctuating after the maximum point. The contour maps of the flow showed that the flow has a vertical and horizontal flow component (V_r , V_z) in the core center ($0 \leq X/D \leq 0.5$) of the event. The flow consists essentially in a vertical flow component before impinging the ground plane. This component is very dangerous on any structures (building, Airplane, etc.). (Asano et al., 2019; Chay and Letchford, 2002; Jesson et al., 2015; Mason et al., 2009; Zhang et al., 2014) showed that once the flow has impinged the ground and diverged outwards, the mean velocity reaches the maximum at $X/D = 0.75 - 1.5$ and the wind speed starts decreasing with the height.

2.2.2 Review of Facilities

Moving Jet simulator (TTU)

The moving jet simulator (TTU) was developed at Texas Tech university. The TTU simulator is a moving jet wind tunnel that uses a 5.6 kW centrifugal blower with a 0.51 m jet outlet diameter and can produce stationary and moving downbursts. The moving events are produced by setting the blower on rails and translating them manually with a speed up to 2 m/s (Chay and Letchford, 2002, see also Fig. 2-11).

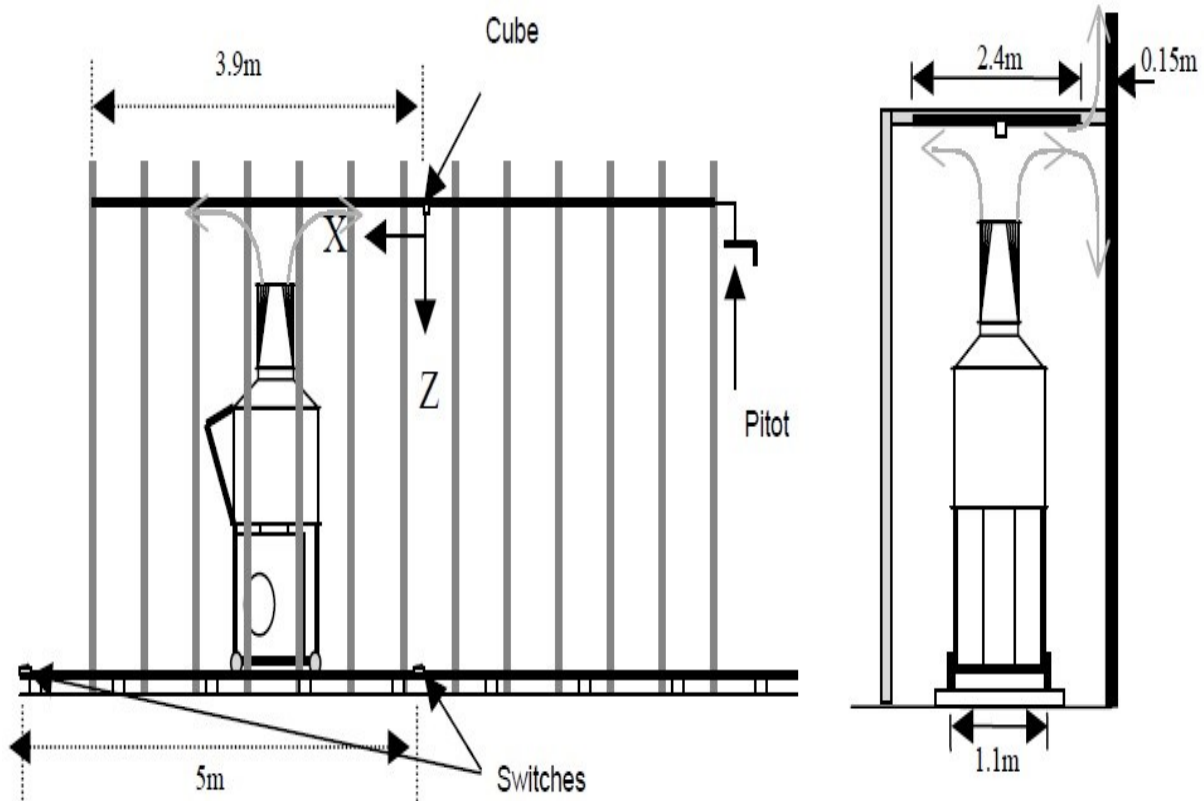


Figure 2-11 Schematic diagram of Texas Tech jet wind tunnel, after Chay and Letchford (2002)

Iowa University simulator

An impinging jet was designed and constructed to simulate stationery and translation downbursts at Iowa University. The jet diameter is equal to 1.83m. The Iowa University simulator used different scale models. Sengupta and Sarkar, (2008) used an exit nozzle diameter of 0.203m and a geometric scale of 1:2600. while Zhang et al. (2013), used a 0.61m jet diameter with a geometric scale of 1:650, see Fig. 2-12. The maximum translation speed that can be reached in the Iowa University simulator is 0.61 m/s.

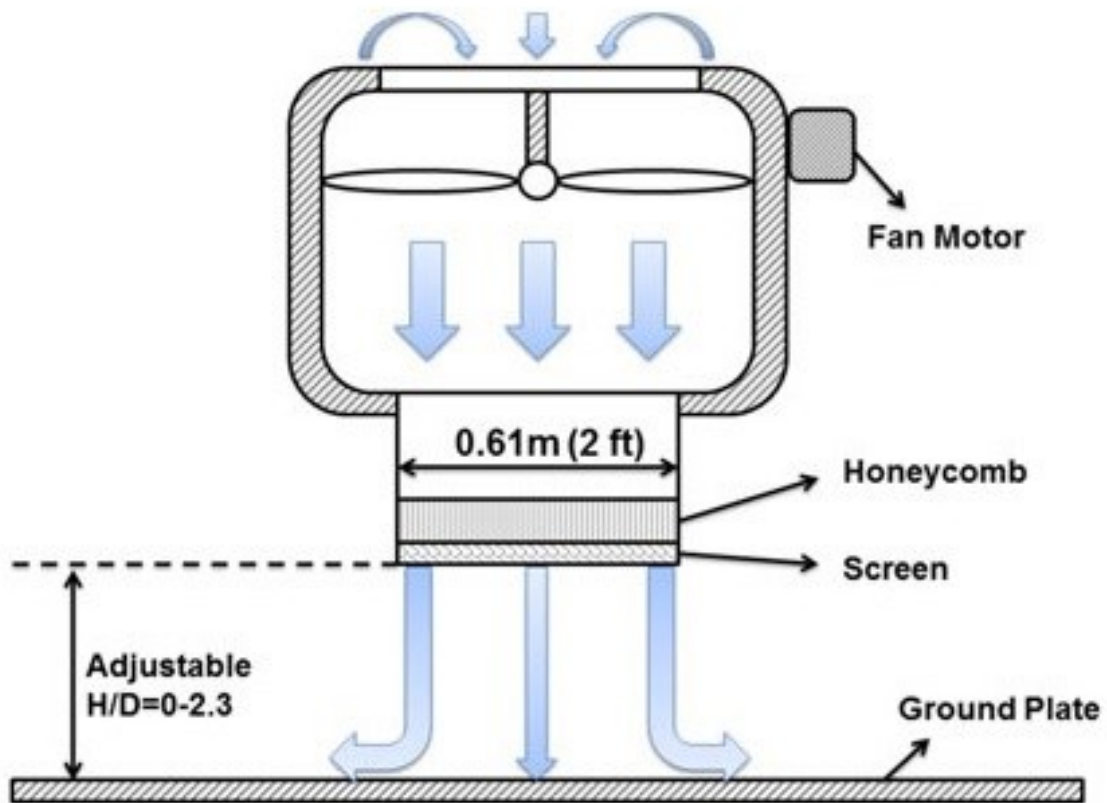


Figure 2-12 Schematic diagram of ISU microburst simulator, after Zhang et al. (2013)

University of Birmingham simulator

The University of Birmingham simulator generates downburst using nine fans with a jet nozzle diameter of 1m, and a length scale of 1:700 - 1:1000. The distance of the jet exit to the ground plan (height) is adjustable, see Fig. 2-13. The simulation of translation can be achieved using a movable platform underneath the simulator and the translation speed can reach the maximum value of 3 m/s.

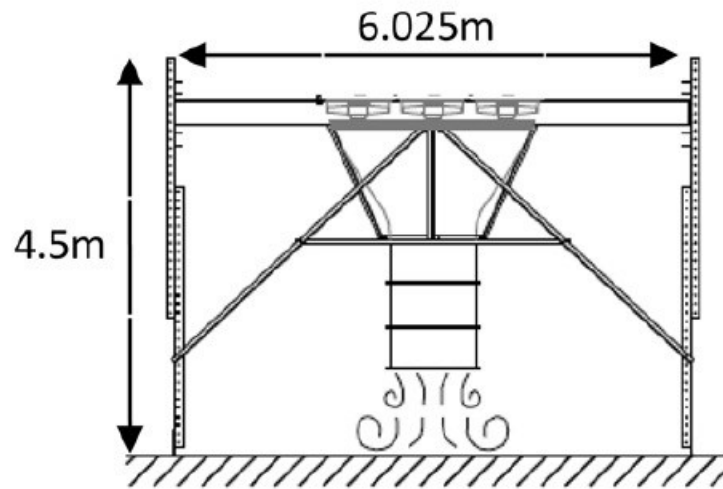


Figure 2-13 Schematic diagram of Birmingham university jet nozzle, after McConville et al. (2009)

Western university simulators

Western University has two simulators; the first simulator is the impinging jet simulator that uses a fully developed pipe with a diameter of 40 mm connected to a blower chamber. The second simulator is the WINDEEEE Dome, a large-scale simulator that connects the top fans to a bell-mouth of adjustable diameter (1.6 m – 4.5 m) to produce inflow. The wall fans are used to remove the air, see Fig. 2-14.

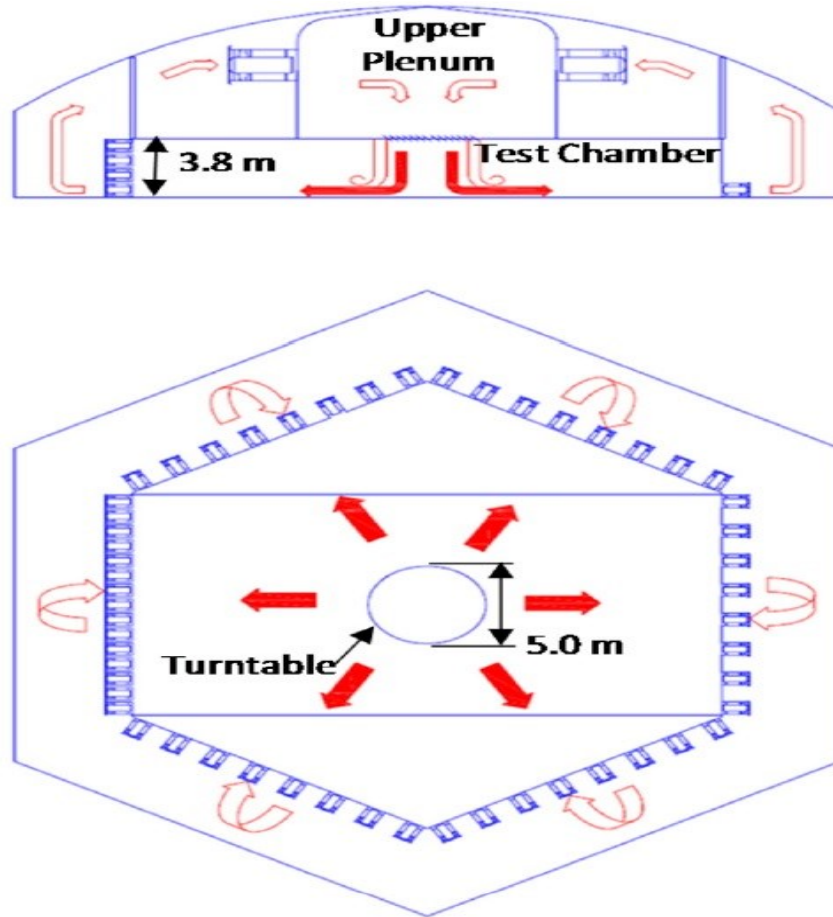


Figure 2-14 Schematic diagram of Western university downburst simulator, after Hangan et al., (2017)

Conclusively, the previous studies show differences in the simulated wind speed profile and the measured wind load. These differences may be attributed to the differences in the simulated velocity profile used in the experiments. Moreover, the effects of the simulation parameters (i.e., model dimensions, wind direction, etc....) have not been sufficiently addressed.

Chapter 3. Wind Codes and Standards - Non-synoptic Winds

In the past, little attention has been allotted to examine the effect of the non-synoptic events on buildings. Currently, only a few of the national building codes and standards are considering the risk of the non-synoptic winds. There are few recommendations and guidelines provided to the designers to protect the buildings from this risk. This Chapter presents the current guidelines and recommendations provided.

3.1 National Building Code of Canada (NBCC)

The National Building Code of Canada (NBCC 2015) version and the previous version (NBCC 2010) provided the same comments and recommendations about tornadoes in the commentary I part.

NBCC (2015) defines three tornado prone regions in Canada based on the tornado intensity and tornado probability of occurrence. As shown in Figure 3-1, the Fujita scale (see Table 1-1) has been used to describe the wind speed ranges. These regions can be described as following:

- 1) “Regions prone to significant tornadoes”: Severe tornado with a high-speed and tornado intensity of F2-F5 and probability of occurrence per km² exceeding 1×10^{-5} per year.
- 2) “Regions prone to tornadoes”: Tornado intensity of F0-F2 and probability of occurrence per km² exceeding 1×10^{-5} per year.
- 3) “Regions where tornadoes are possible”: Represent the regions that have a probability of occurrence per km² not exceeding 1×10^{-5} per year.

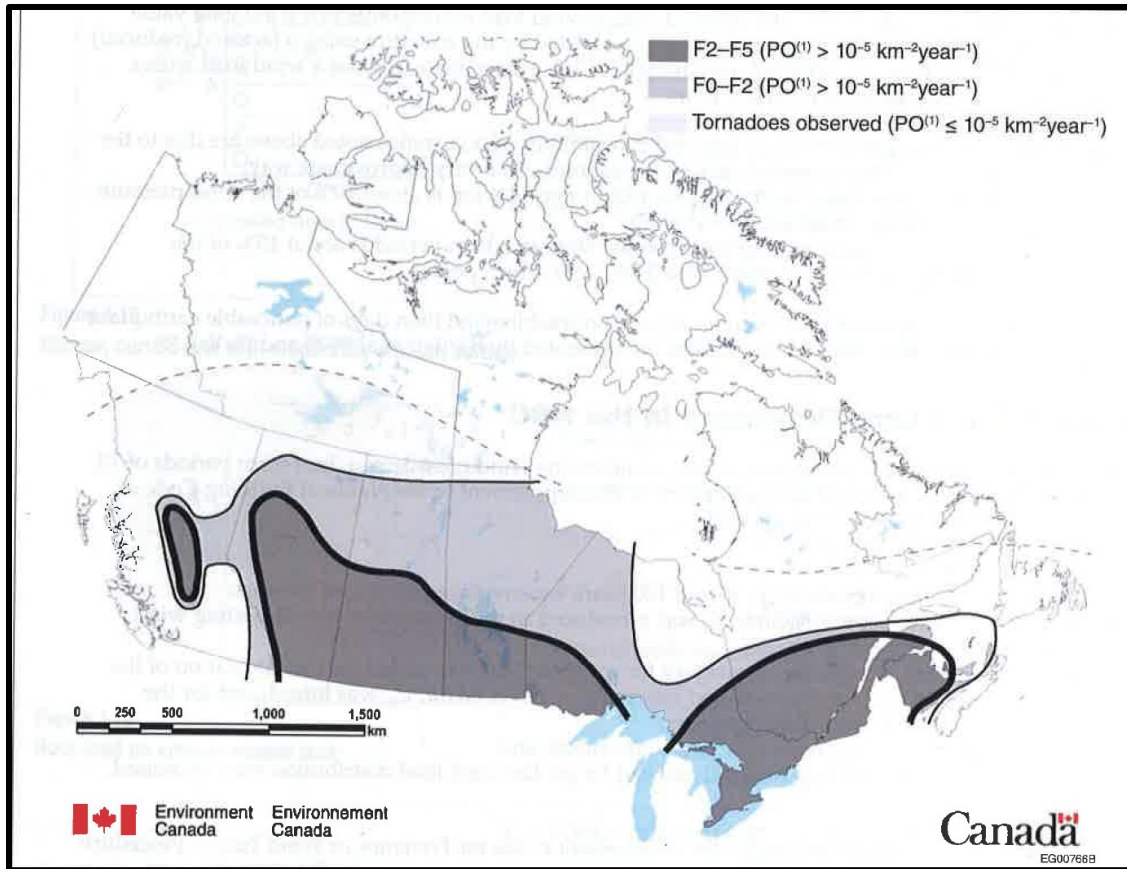


Figure 3-1 Tornado-prone regions of Canada, after (NBC2015, 2015)

(Allen, 1986, 1984) investigated the damage that occurred due to real tornado events. More than 90% of the physical losses that occurred was because of the details of the buildings that did not satisfy the construction details. The floors anchorage into the foundation and the roofs anchorage through the concrete walls should be designed following the standards. So that, NBCC (2015) recommends that the previous details should be designed according to an uplift wind factor of 2 kPa on the roof, 1 kPa of lateral wind on the windward wall, and 2 kPa of suction wind on the leeward wall.

3.2 American Society of Civil Engineers (ASCE 7)

The American Society of Civil Engineering standard versions of ASCE 7-98 to ASCE 7-10 have not considered the non-synoptic winds. In the commentary part, the standards have provided some references that show guidance for tornado resistance design. In addition, these versions provide a velocity map corresponding to the probability of occurrence of 10^{-5} (see Fig. 3-2).

The latest version (ASCE 7-16) has not considered the non-synoptic winds. However, the standard provides a section in the commentary part (C26.14), which shows a guidance to design and protect buildings in order to reduce the building damage probability and increase the protection level in case of a tornado occurrence.

Figure 3-3 shows the recorded tornado that has an intensity rate of EF3-EF5 between 1950-2013. These events represent 5% of the total recorded tornado in the United States, the EF3 rated tornado has a percentage of 4% of the total recorded events, and 1% for the rated EF4-EF5; whereas 95% were rated as EF0-EF2.

Federal Emergency Management Agency (FEMA) has recommended a wind speed map that is shown in Figure 3-4. These speeds are used to calculate the wind pressure caused by a tornado to protect a specially designed room. The commentary part provides two methods to calculate the wind pressure and following the recommendations from (FEMA). The first method is the extended method, which is based on the pressure parameters. The second method is the simplified method, which is based on reducing all the changed parameters to a single multiplier. These methods follow the same equation and methodology as those used in chapters 26, 27, 30 of the standards.

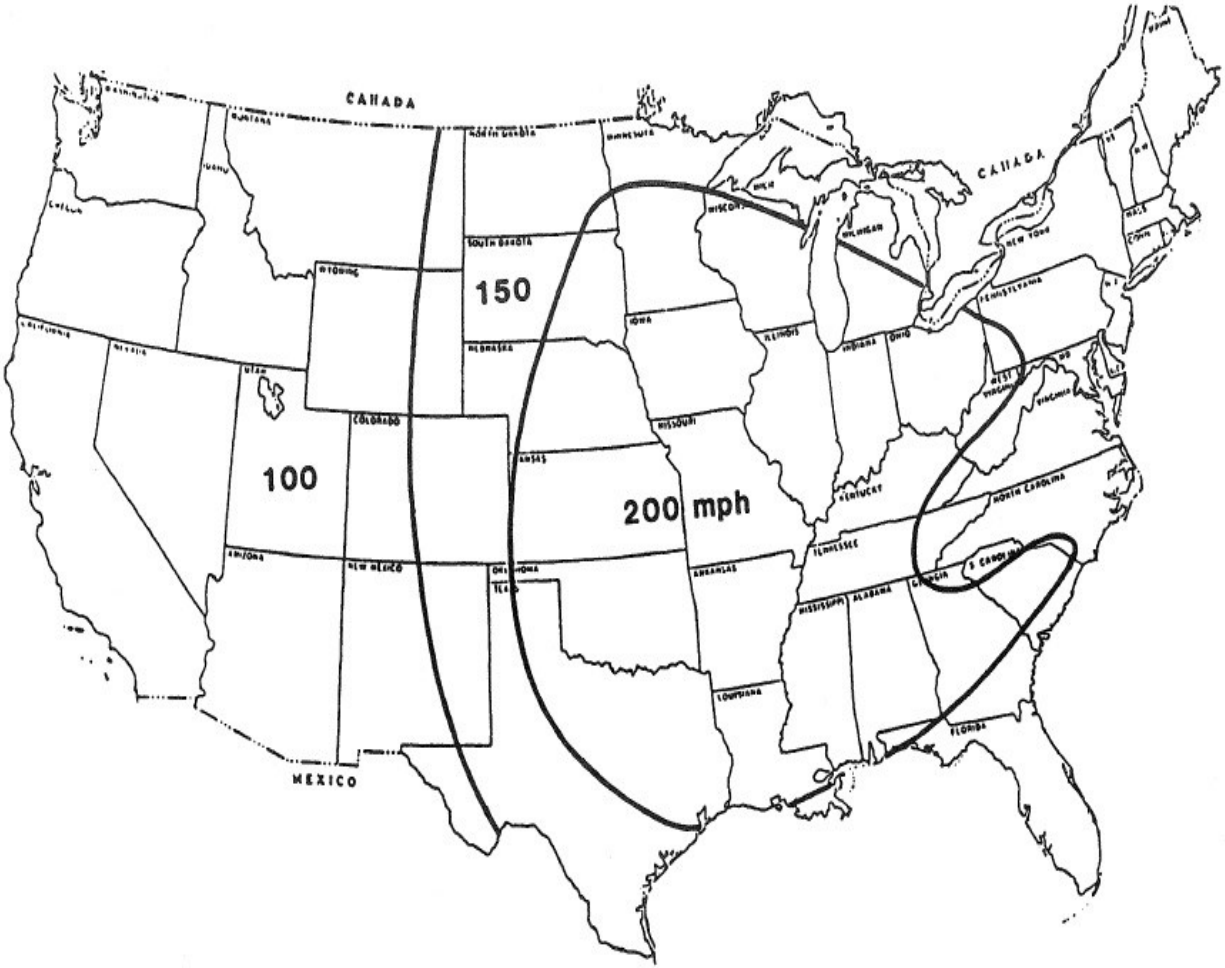


Figure 3-2 Tornado Gust Wind Speed with Annual Probability of 10^{-5} , after (ASCE/SEI 7-10)

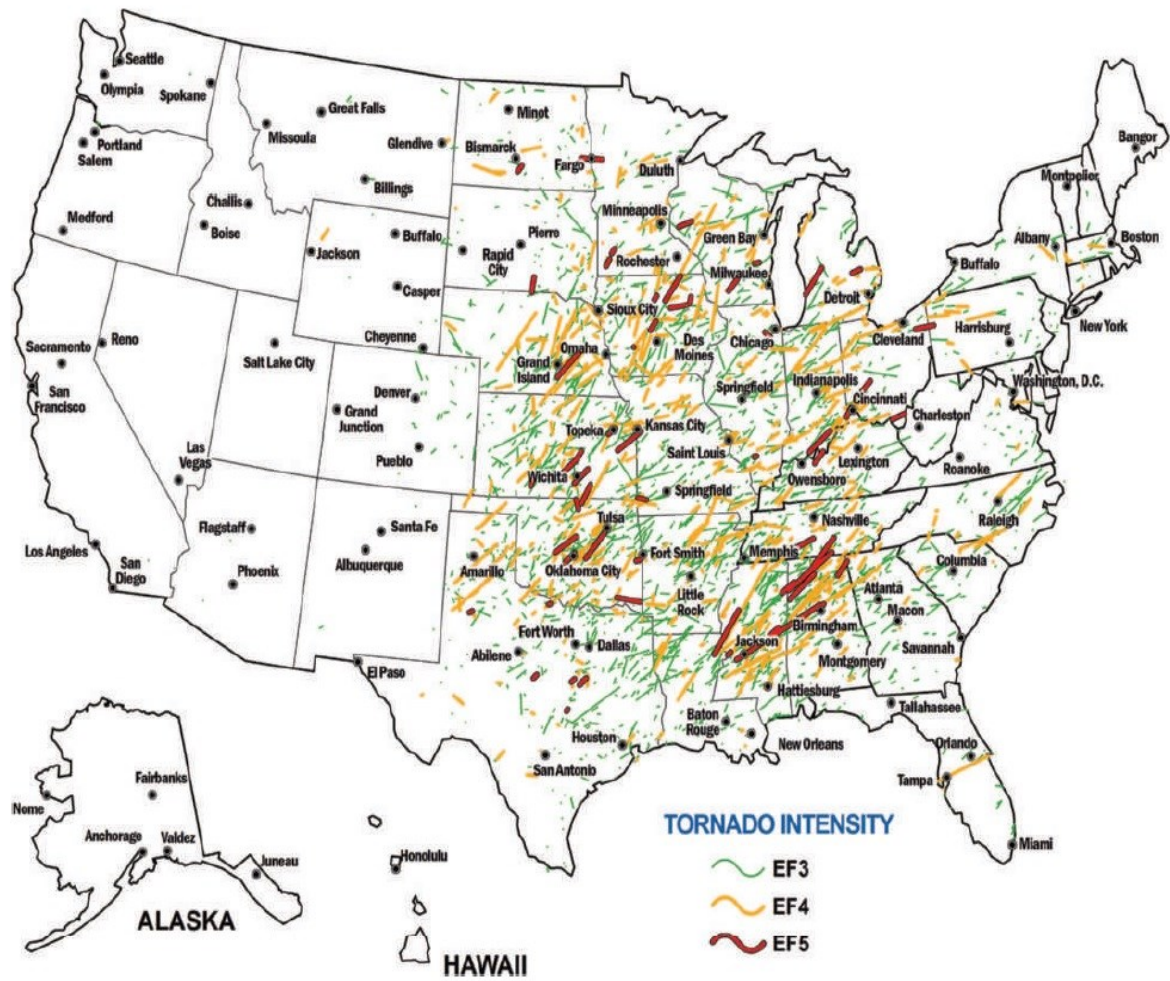


Figure 3-3 Recorded tornadoes between 1950–2013, with a rating of EF3–EF5; after, (ASCE 7, 2016)

3.2.1 The Extended Method

This method uses the upper range of EF-Scale as tornado design wind speed. Tornado may cause a smoother terrain than the original terrain. Thus, it is recommended that the pressures should be determined based on Exposure C conditions.

The velocity pressure equation used for tornado is the same as the straight-line wind (C26.14-1):

$$q = 0.00256k_d k_z k_{zt} k_e V^2 \quad (3.1)$$

k_d : is the directionality factor, this factor considers reducing the probability of maximum wind coming from any given direction, and the pressure coefficient occurring for any given wind direction. In the case of a tornado, both previous conditions did not seem to apply, so that k_d taken as 1.

k_z : is the velocity pressure exposure, based on Exposure C or D as appropriate

k_{zt} : is the topographic factor, Since the complexity of tornado wind speed is not yet understood, the topographic factor is set as 1.

k_e : is the ground elevation factor, sets 1 or based on Table 26.9-1, P-268

Then, the velocity pressure should be calculated using:

$$q = 0.00256k_z V^2 \quad (3.2)$$

The gust-factor (G) value is derived from the gust effect without calibration. So, G-factor was calculated by dividing the rigid building G-factor (0.85) by the calibration factor (0.925). thus, G=0.9 should be the minimum value for tornado design.

Tornado pressure equations for main wind force resistance system (MWFRS) and component and cladding (C&C) are the same as the straight wind:

For (MWFRS): equation (C26.14-2) should be used:

$$p = q_h G C_p - (\pm 0.55) \quad (3.3)$$

$G = 0.9$ or higher if appropriate from current methods
 $C_p =$ ASCE 7 values per Chapter 27

For (C&C): equation (C26.14-3) should be used:

$$p = q_h \left[(0.9 \times (GC_p)) - (\pm 0.55) \right] \quad (3.4)$$

$(GC_p) =$ ASCE 7 values for the appropriate zone.

3.2.2 The Simplified method

This method uses a factor that compensates the pressure factors effect. After a series of calculations, a single factor named the Tornado Factor (TF) provided to be used to calculate tornado wind pressure. Table 3-1 shows the Tornado factor that could be used for different building enclosures and terrain exposure.

Tornado pressure can be estimated using equation (C26.14-4):

$$p = q_i [(GC_p) - (GC_{pi})] \times TF \quad (3.5)$$

The pressure part values $q_i [(GC_p) - (GC_{pi})]$ are taken from chapter 27, and the velocity pressure q_i calculated using the upper end of EF-scale velocity.

On another way, $q_i [(GC_p) - (GC_{pi})]$ can be used directly from chapter 27, and velocity scale should be made with the design tornado speed as follow:

$$p = q_i [(GC_p) - (GC_{pi})] \times \left(\frac{v_{tornado}}{v_{design}} \right)^2 \times TF \quad (3.6)$$

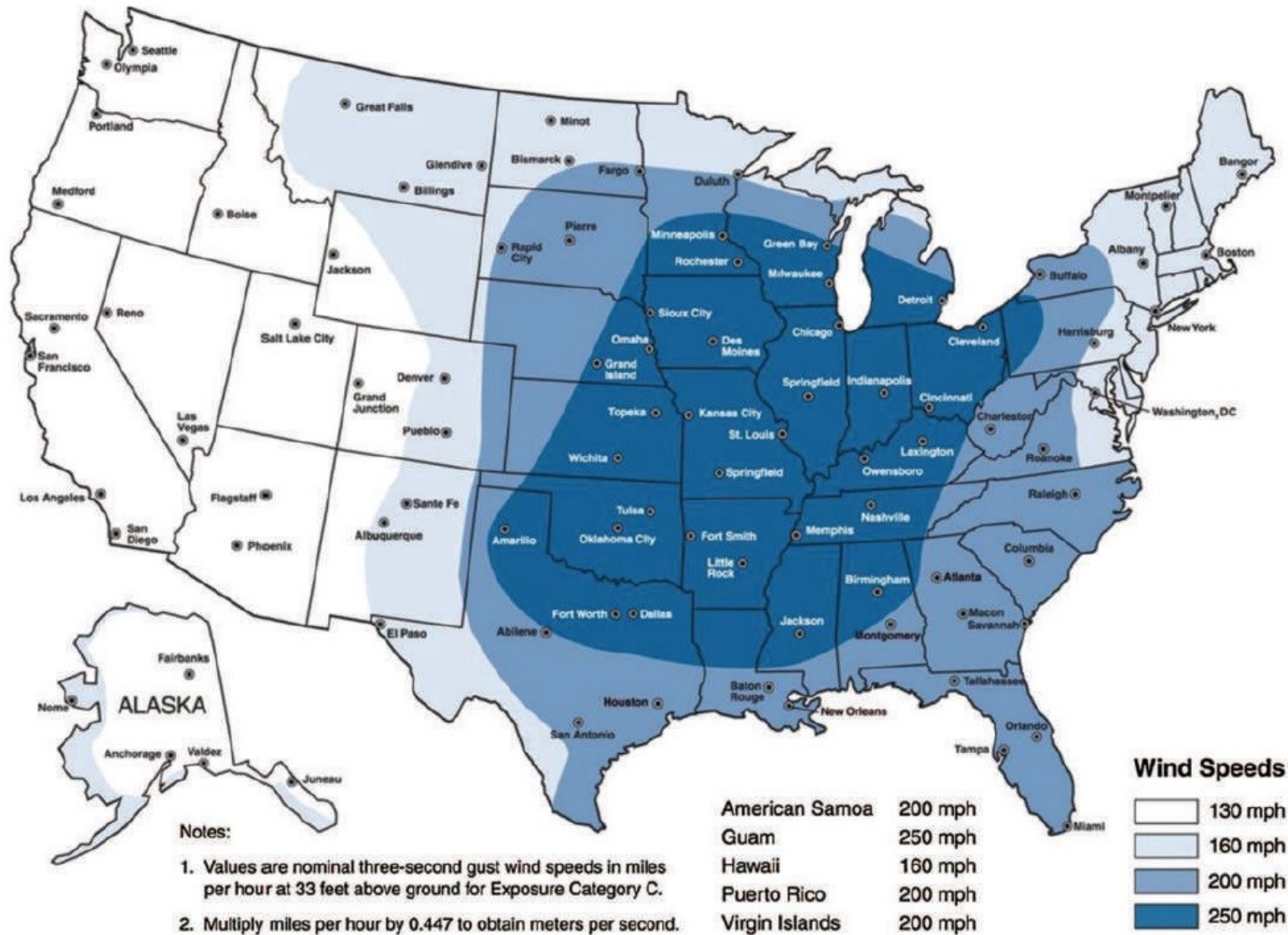


Figure 3-4 Design wind speed map (FEMA, 2015)

Table 3-1 Recommended Tornado Factor (TF), after (ASCE 7, 2017)

Original Enclosure Classification	Loading	Original Exposure B	Original Exposure C or D
Partially enclosed buildings	MWFRS	1.8	1.2
	C&C	1.6	1.1
Enclosed buildings ^a	MWFRS	2.5	1.6
	C&C	2.1	1.5

^aThe tornado factors to be used to increase the design loads on elements of enclosed buildings are based on the effects of high internal pressures. High internal pressures have a much greater effect on elements that typically receive less wind, so the net effect of these increase factors is typically much higher than would result if the building were designed for the specific tornado loads or if the tornado factors for partially enclosed buildings were used with partially enclosed building designs.

Chapter 4. Experimental Methodology

Thunderstorm wind has a different velocity profile than straight-line wind. The main difference is that the wind velocity increases until it reaches its maximum at a low height (near the ground). After this point, wind velocity decreases as the height increases. Furthermore, to generate velocity profile with the same trend of thunderstorm profile, several configurations were tried out at the boundary layer wind tunnel (BLWT) at Concordia University using different roughness elements and flow obstructions. This chapter presents a description of the boundary layer wind tunnel at Concordia University and the modification of the test configurations.

4.1 Description of the facility – applications

The boundary layer phenomenon is primarily generated due to the free-flow wind interaction with the surface friction including submerged bodies. In general, the wind speed increases with height above the ground surface while the turbulence intensity decreases.

“The correct model test for phenomena in the wind must be carried out in a turbulent boundary layer, and the model-law requires that this boundary layer be to scale as regards the velocity profile” (Jensen, 1958)

The wind tunnel is a reliable tool to predict the wind effects on buildings (Davenport and Isyumov, 1967). It is considered as the main tool to aid the designers to evaluate and examine the wind effect on buildings.

4.1.1 Building Aerodynamics Laboratory at Concordia university

The boundary layer wind tunnel at Concordia university is used to create the wind velocity profile of the present study. A centrifugal blower with a maximum flow rate of 40 m³/s (86400 cfm). can be generated. Open circuit design with a cross-section of 1.8 m x 1.8 m (width x height) where the height can be reduced to 1.4 m to achieve the desired exposure, and 12 m in length (see Fig. 4-1). The wind speed can be adjusted manually from 3 m/s to 14 m/s. The floor of the wind tunnel is covered with a polypropylene carpet and the ceiling is made of suspended wooden panels of adjustable height. Different terrain exposures can be achieved using additional floor panels with specific roughness elements (see Fig. 4-2). A measurements turntable with a diameter of 1.2 m placed at the test section allows measuring the wind flow from different direction. A honeycomb mesh was placed in front of the blower to remove the turbulence created by the fan, more details are provided by (Stathopoulos, 1984).

The Building Aerodynamics wind tunnel at Concordia University has two main measurements systems:

The first system is the velocity flow field instrument that can measure the wind speed and turbulence intensity profiles using Turbulent Flow Instrumentation by 4-hole Cobra Probe. This instrument is capable to quantify the three velocity components (X, Y, Z). The Copra Probe can be automatically adjusted vertically and horizontally, to allow the measurements at various heights and horizontal locations. In addition, the measurements were conducted at a sampling duration of 30 seconds. The length scale is the ratio of the thickness of the simulated wind tunnel boundary layer flow to the corresponding boundary flow in the field, which is similar to the ratio of the wind tunnel model to the prototype. The selected length scale is 1:400. For example, a height of 5 cm developed over the wind tunnel floor is approximately equivalent to 20 m boundary layer thickness in full-scale.

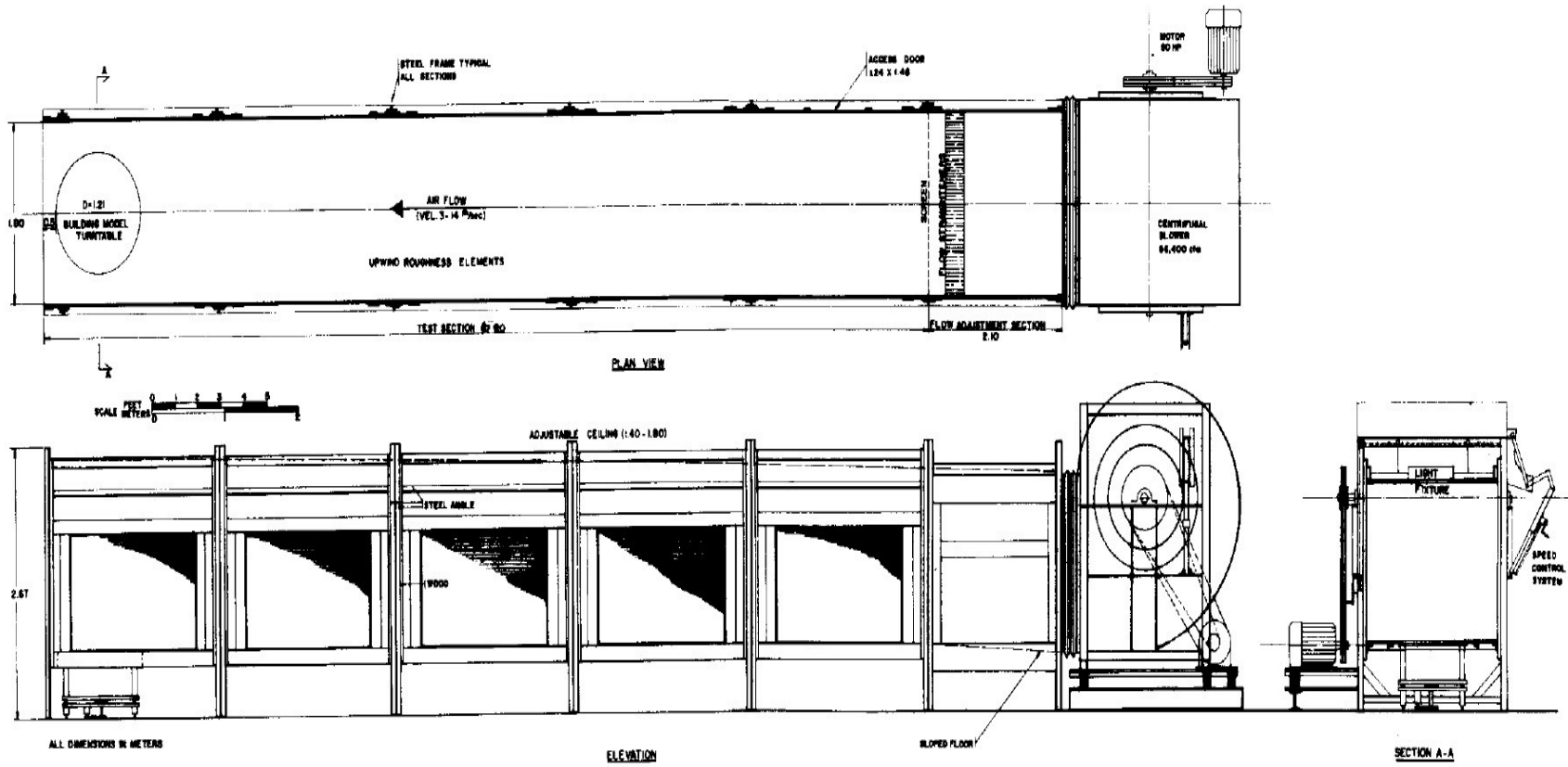


Figure 4-1 Construction view of Concordia University wind tunnel (Top and side view)

The free-stream wind speed (gradient velocity) in the wind tunnel was set at 11.0 m/s at a velocity scale of 1:3, to simulate the full-scale gradient velocity of 33.0 m/s at the atmospheric boundary layer height. Corresponding to the length scale of 1:400 and the velocity scale of 1:3, the time scale was determined as 1:133. These calculations are estimated based on the following equation.

$$\frac{VT}{L} \Big|_{Full-scale} = \frac{VT}{L} \Big|_{Wind\ tunnel}$$

The second measurement system is the pressure measurement instrumentation consisting of a Digital Service Module (DSM 3400). The DSM 3400 is connected to eight electronic scanners of 64 channels each. The scanners read the pressure signals coming from the connected model pressure taps. The DSM receives these signals from the scanners and converts them into readable data on the computer monitor. For purging purposes, compressed air is connected to the system. The pressure signals are measured for a period of 27 seconds on the wind tunnel scale, corresponding to a one-hour full scale. and sampling frequency of 300 Hz.



Figure 4-2 Front view of the Boundary Layer Wind Tunnel at Concordia University

4.1.2 Atmospheric Boundary Layer velocity profile (ABL)

Different terrain exposures can be simulated by adding floor panels with specific roughness elements (see Fig. 4-3). exposure B (suburban exposure) can be simulated using roughness elements that contain polystyrene cubes and eggboxes. On the other hand, Exposure C (open country exposure) can be simulated using a thick carpet. Figure 4-4 shows the variation of mean wind speed and turbulence intensity with height, the height Z is normalized by the gradient height, Z/Z_g , for both exposures. The mean wind speed at any height, \bar{V}_Z , is presented with respect to the mean gradient speed, \bar{V}_g . Where \bar{V}_g and Z_g are the velocity and height above which the velocity maintains a constant value. Z_g represents the thickness of the atmospheric boundary layer.

Figure 4-4 shows a smooth increase in the velocity profile in either exposure B or C, the main difference is the gradient velocity that could be reached in exposure C at a height lower than that of the suburban terrain. This is due to the higher roughness in exposure B where the wind takes a longer vertical distance to readjust to the unobstructed wind speed. On the other hand, the turbulence intensity of the suburban terrain was greater than that of the open country exposure, due to the same cause mentioned above.

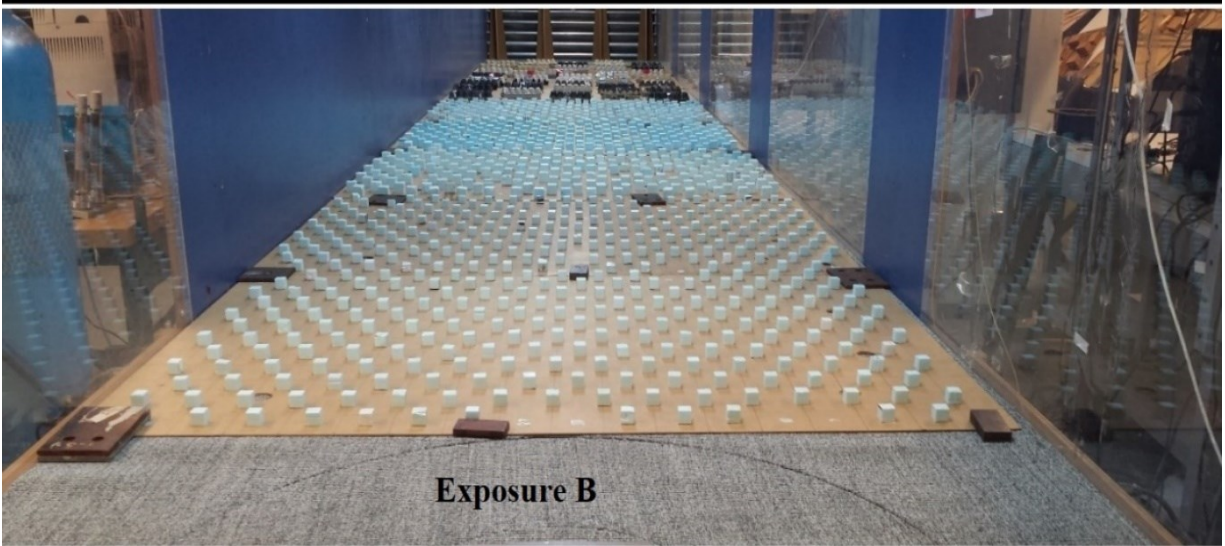


Figure 4-3 Exposure C and Exposure B at the wind tunnel of Concordia University, after (Aldoum and Stathopoulos, 2020)

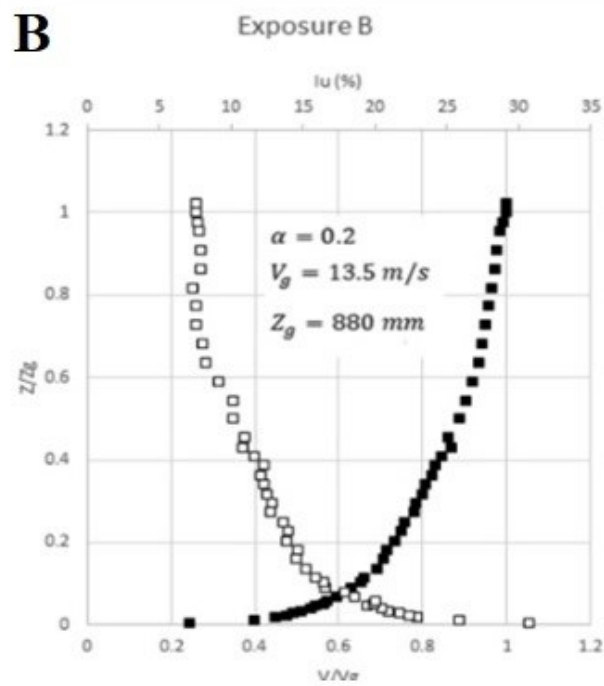
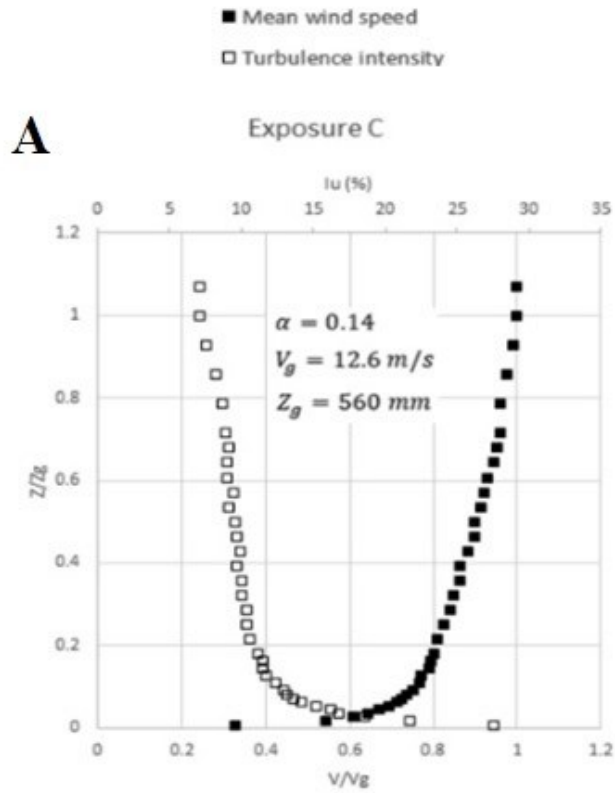


Figure 4-4 Vertical mean wind speed and turbulence intensity for exposure C and exposure B, after (Aldoum and Stathopoulos, 2020)

4.2 Modification of flow simulation attempts

Tornadoes and downbursts are three-dimensional dynamic flows. In the case of tornadoes, the swirling flow leads to a flow of higher complexity compared to the case of downbursts. Therefore, it is very difficult to simulate a tornado and achieve such complex flow characteristics in typical boundary layer wind tunnels. In the present study, a downburst-like profile has been established in the BLWT of Concordia University.

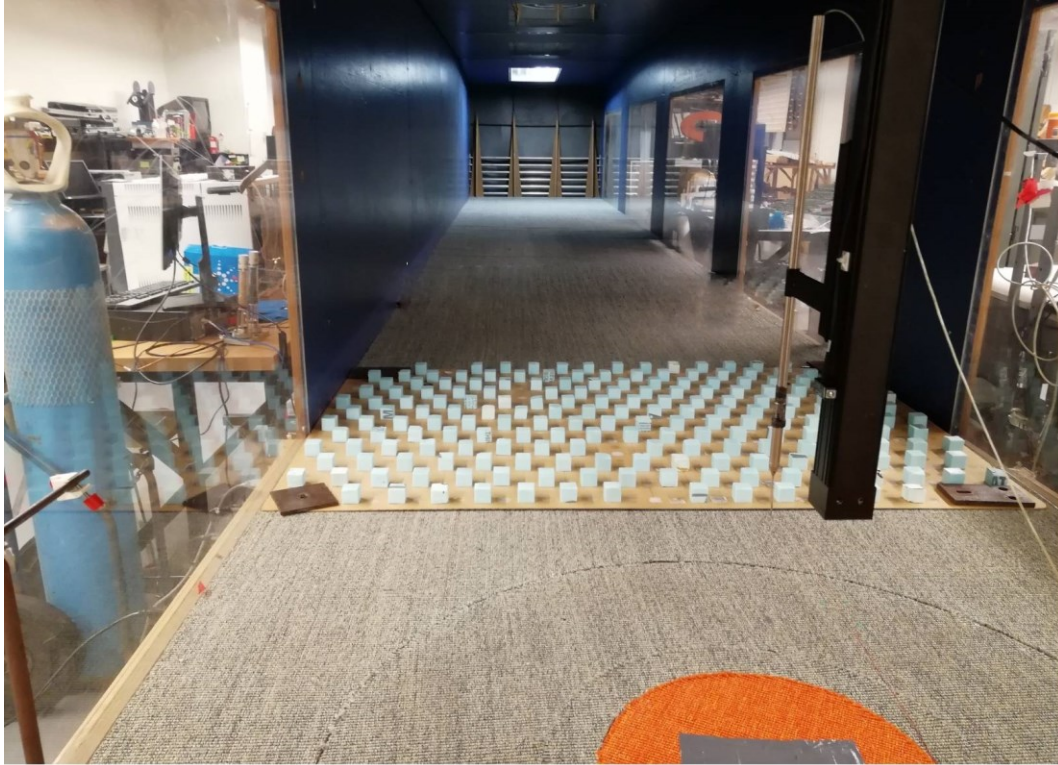
This section presents the modifications made at BLWT at Concordia University in order to simulate non-synoptic wind profiles. Using different roughness element panels and obstacles with the open country exposure, 18 different experimental configurations were conducted to achieve the trend of the thunderstorm wind profile. Table 4-1 shows the number of testing configurations considered in each of the five trials performed.

Table 4-1 Testing configurations in each trial

Trial #	Number of configurations
Trial 1	2
Trial 2	2
Trial 3	1
Trial 4	9
Trial 5	4

In the first trial (Trial 1), one roughness element panel and two roughness element panels have been used and placed close to the measurement location, as shown in Figure 4-5. These configurations have been developed using different distances between the roughness elements and the measurement location to understand how these elements affect the velocity profile.

A



B

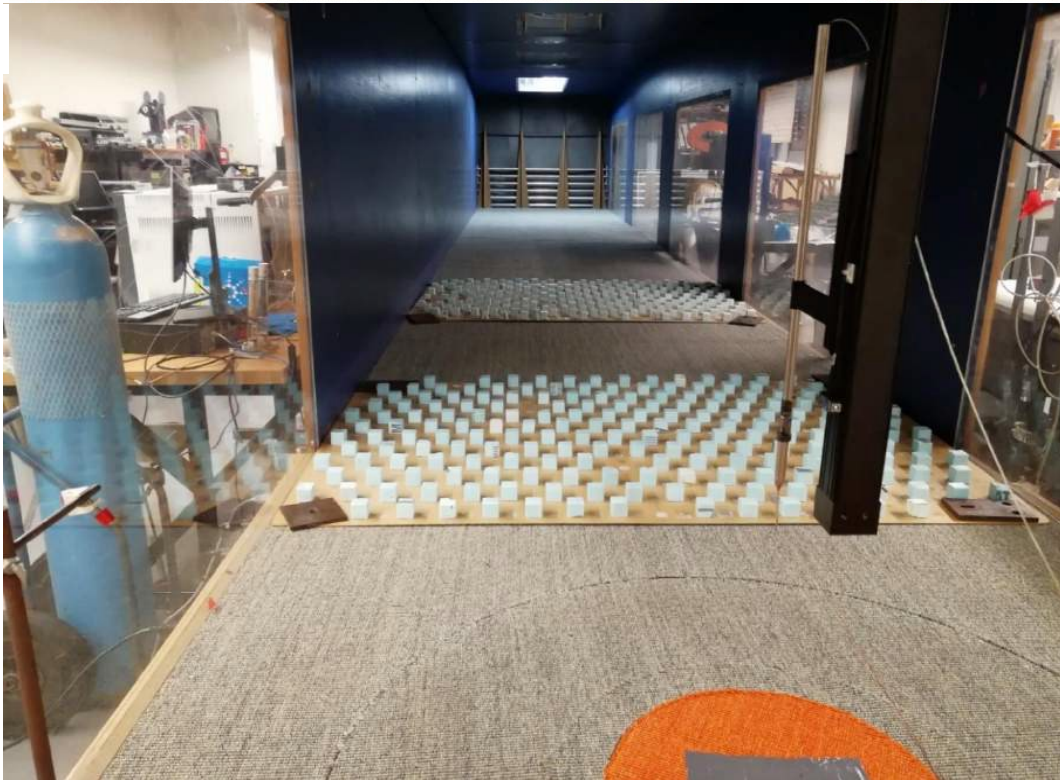


Figure 4-5 Trial 1 configurations at BLWT of Concordia University; A) one roughness element panel B) two roughness element panels

In the next trial (Trial 2) which was done in the wind tunnel, a wood obstacle with a height of 10 cm was used to accelerate the velocity at a low height. This trial includes different configurations, such as the wood obstacle, placed at 2 m from the measurement point with two roughness element panels shown in Figure 4-6. The difference in those configurations was materialized by removing the four boards of triangular shape (spires).

The following trial (Trial 3) the wood obstacle alone was placed very close to the measurement location. This configuration aimed to investigate the effect of the wood obstacle position with respect to the measurement point, see Figure 4-7.

The previous trials have helped to understand how the obstacles and the roughness element panel position affect the velocity profile. Different attempts have been made in the following trial (Trial 4). A circular rod with an inner diameter of 7.5 cm and outer diameter of 8 cm without the rectangular spires, as shown in Figure 4-8. The tests have been conducted on three different configurations, where the circular rod has been placed at a certain height above the carpet level. Figure 4-9 shows top and side views of the test configuration where D represents the horizontal distance between the circular rod and the measurement point. H_1 is the vertical height of the circular rod above the carpet. Table 4-2 shows the test specifications.

A



B



Figure 4-6 Trial 2 configurations at BLWT of Concordia University; A) with spires, B) without spires



Figure 4-7 Trial 3 configuration at BLWT of Concordia University

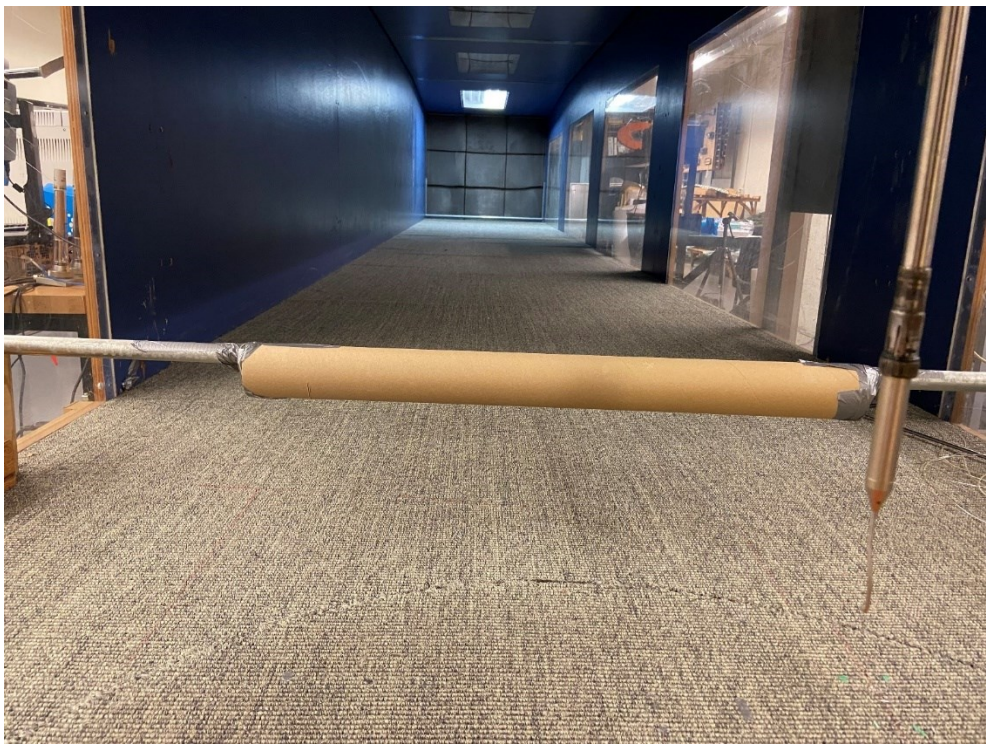


Figure 4-8 Typical configuration of Trial 4 at BLWT of Concordia University

Through the configurations of Trial 4, the wind velocity profile and the turbulence intensity show encouraging results. The velocity profiles were different than the atmospheric boundary layer profile and met the thunderstorm velocity profile partially in some configurations. Therefore, some modifications for trial 4 were necessary.

Trial 5 aimed to enhance the results of trial 4. In this trial, two circular rods have been used and the spires have been installed in their original place at the fan outlet. Four different configuration setups have been used. Figure 4-11 presents the top and the side views sketch that shows the test configuration where D represents the horizontal distance between the circular rod and the measurement point. $H1$ is the vertical height of rod 1 and $H2$ is the vertical height of rod 2 above the carpet, where X is the distance between the rods. Table 4-3 shows the test specifications.

Moreover, in trial 5, the distance between the first rod and the measurement point, and the height of the rod1 was located at a $D=50$ cm and $H1=15$ cm, respectively. These dimensions were used in trial 4 (Set 1 and configuration III) - see Table 4-2 - and produced a better profile than the other dimensions (in trial 4).

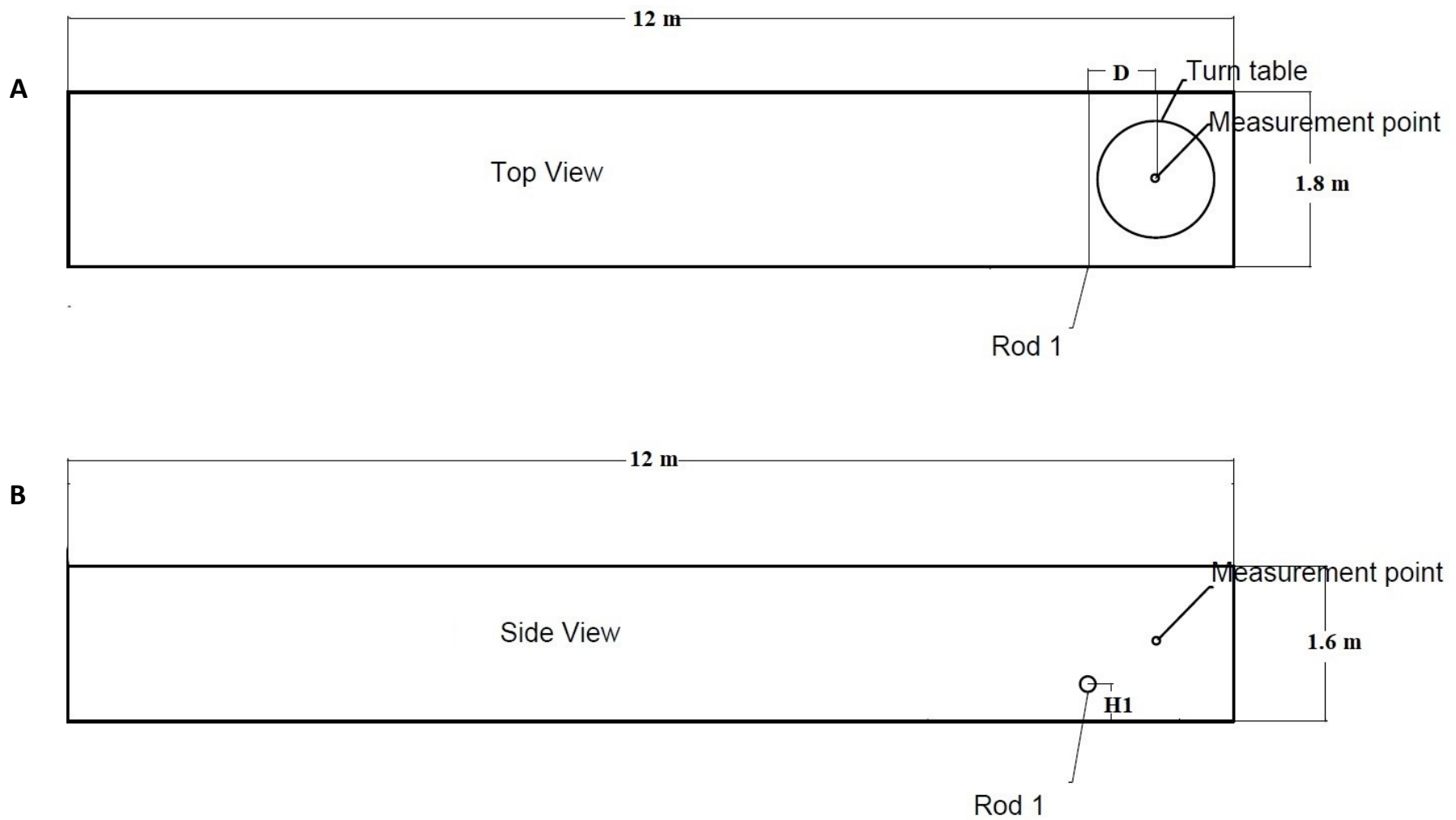


Figure 4-9 A cross section of the BLWT at Concordia University shows Trial 4 modifications: A) top view, B) side view

Table 4-2 Dimension details of Trial 4 configurations

	H1 (cm)	D (cm)		
		Set 1	Set 2	Set 3
Configuration I	5	50	60	70
Configuration II	10	50	60	70
Configuration III	15	50	60	70

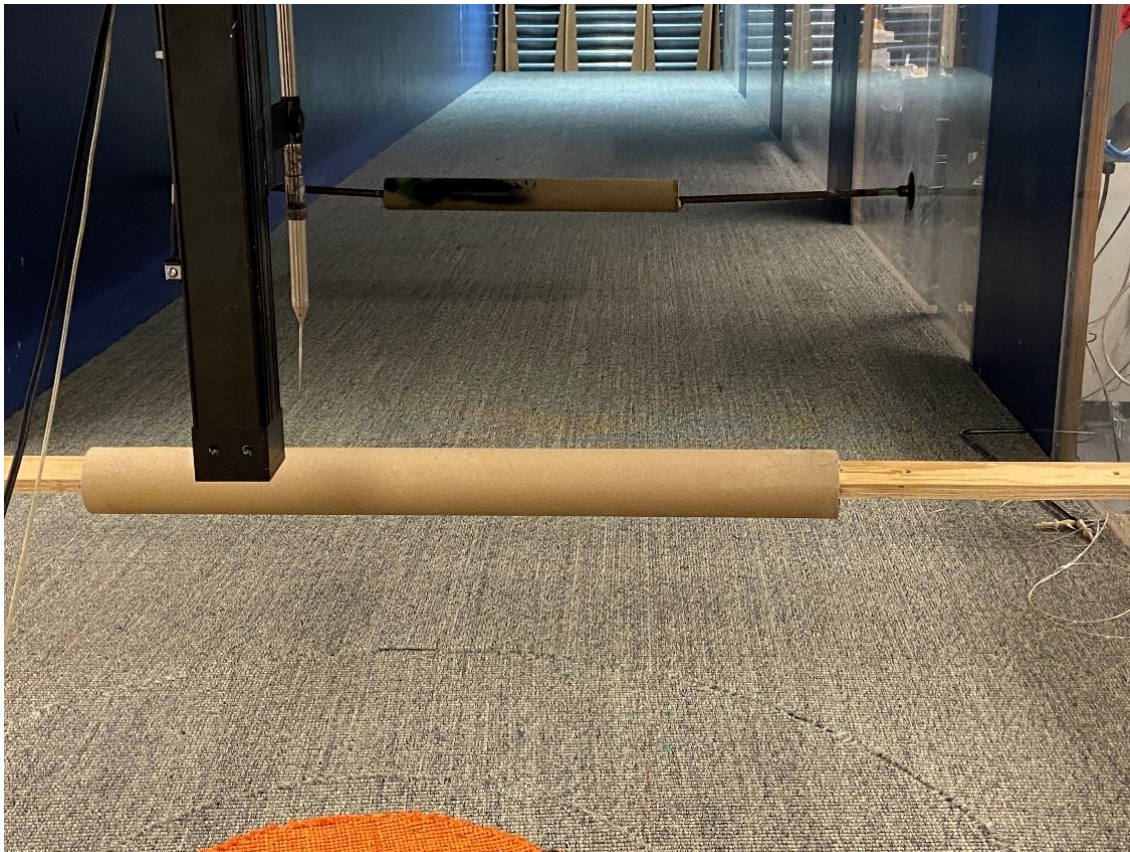


Figure 4-10 Typical configuration of trial 5 at BLWT of Concordia University

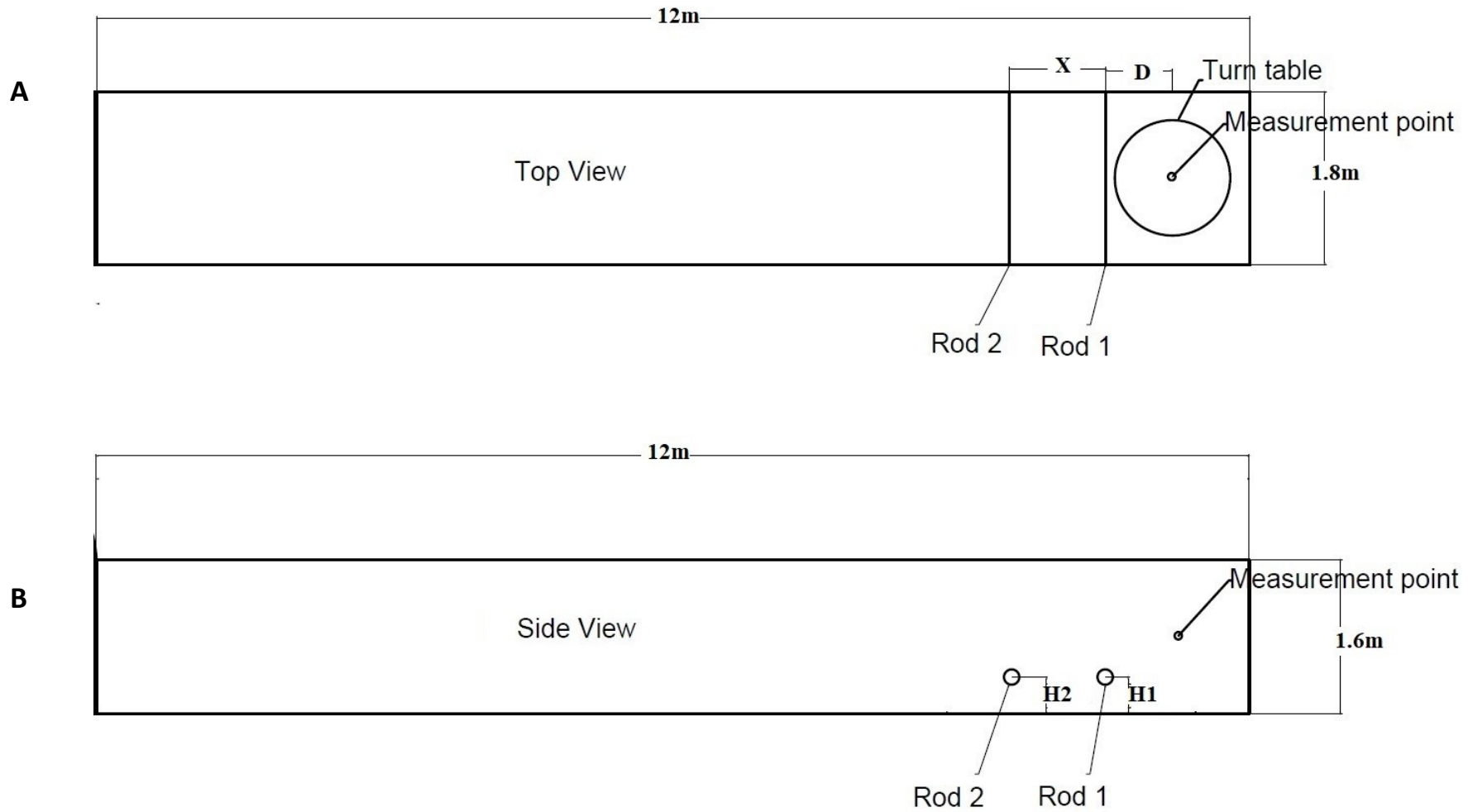


Figure 4-11 A cross section of the BLWT at Concordia University shows Trial 5 modifications: A) top view, B) side view

Table 4-4-3 Dimension details of Trial 5 configurations

	H1 (cm)	H2 (cm)	X (cm)	D (cm)
Configuration I	15	20	200	50
Configuration II	15	20	150	50
Configuration III	15	20	100	50
Configuration IV	15	0	200	50

4.3 Model Configuration

Wind tunnel tests have been conducted for a low-rise building model with flat square roof (150 mm x 150 mm) with full-scale equivalent dimensions 60 m x 60 m. The model is made of Plexiglass and is equipped with 124 roof pressure taps. Figure 4.12 shows the perspective view of the pressure tap layout on the roof of this basic model. A flexible plastic tube of 550 mm length with interior and exterior diameter of 2.18 and 1.37 mm respectively were used to connect each roof pressure tap with the pressure transducer. The 124 tubes connected to the basic model were divided into 2 groups: the first one includes 63 tubes while the second one includes 61 tubes. Thus, the 63 pressure taps of the first group were connected to the first 63 pressure channels on the pressure scanner (ZOC33/64Px), while the remained pressure channel was allocated to the Pitot tube in order to measure the reference free-stream velocity pressure.

As shown there, the highest density of pressure taps is at the windward corner of the roof. Also, the taps are placed as close as possible to the roof edges. The distance from the first line of pressure taps to the adjacent roof edge is 0.01 of the building width of 60 m model (0.6 m in full-scale). The wind directions considered in this study are also indicated in this figure, such that the wind direction at 0° when the wind was normal to the windward edge of the model plan and increase in clockwise direction to complete a quarter cycle (0° to 90°) at increments of 15° . The building model was tested at an equivalent full-scale height of 10 m and 20 m (25 mm, 50 mm wind tunnel scale, respectively), by sliding the model downwards within a precise tightly fit slot in the turntable.

The pressure scanners are calibrated to scan the pressure signals at frequency of 300 Hz (300 samples per second) for a total period of 27 seconds on wind-tunnel scale or 3600 seconds in full-scale. The instantaneous surface pressures over the entire roof have been measured in the test section of the wind tunnel for all wind directions in terms of time history wind load. The measured pressures have been normalized by the mean dynamic pressure measured at reference height to express them as non-dimensional pressure coefficients.

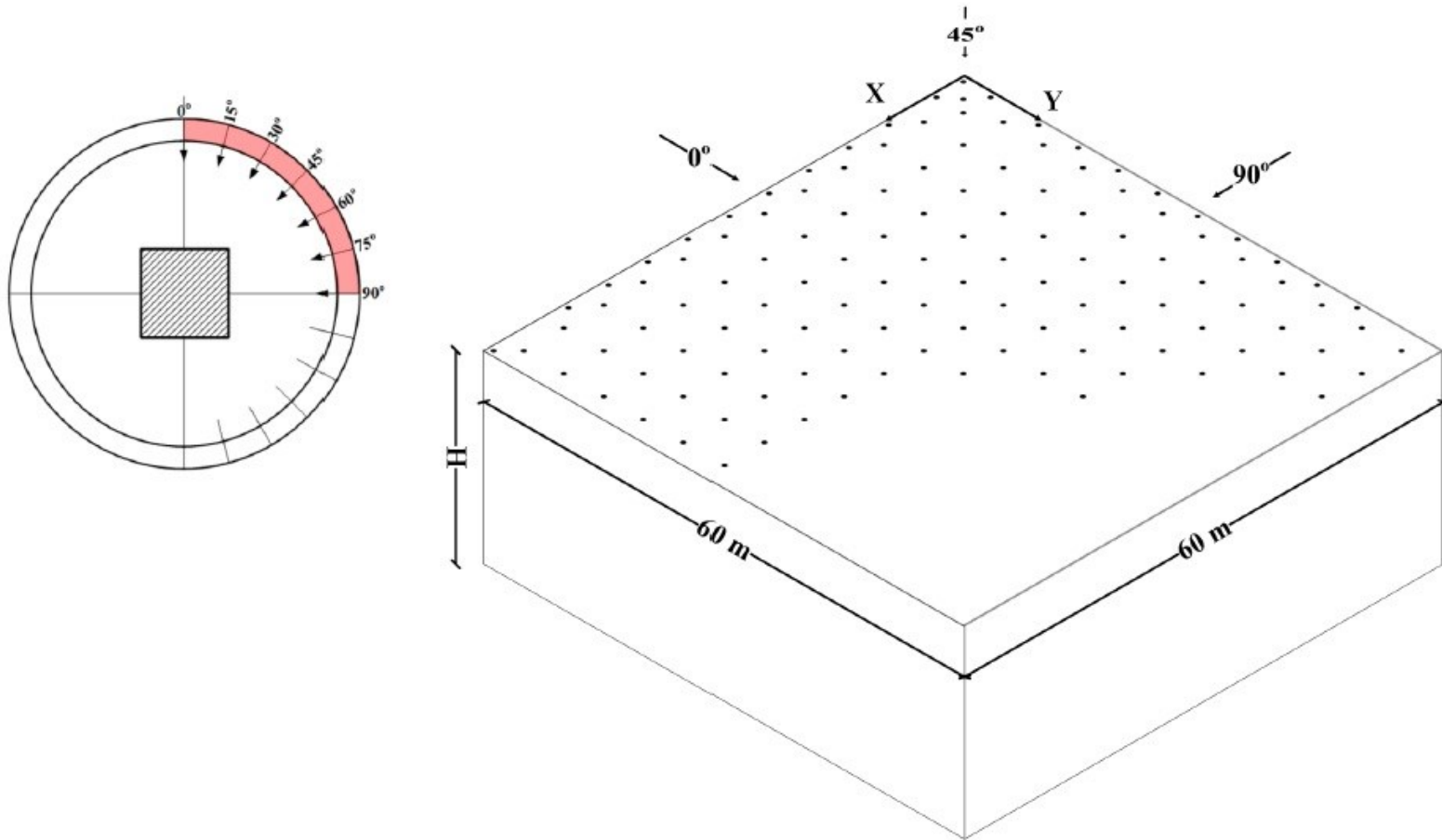


Figure 4-12 60m x 60m building model with pressure tap layout on the roof

The external wind pressure coefficient at measurement pressure tap (i) is defined as:

$$\text{Pressure coefficient: } C_{p_i}(t) = \frac{p_i(t) - p_s}{\bar{q}_z}, \quad \bar{q}_z = \frac{1}{2} \rho \bar{V}_H^2 \quad 4.1$$

in which C_{p_i} is the instantaneous wind pressure coefficient at pressure tap (i), P_i is the wind pressure at tap (i), P_s is the static pressure at reference location, \bar{q}_z is mean value of the dynamic pressure at reference height Z_{ref} , ρ is the density of the air and \bar{V}_H is the mean value of the wind velocity at roof height. In the present study, the reference height was taken at the position of the Pitot tube in the free stream ($Z=600$ mm).

The $P_i(t) - P_s$, which represents the wind pressure acting at the particular pressure tap (i), was derived directly by the laboratory transducer (ZOC33/64Px), as the differential pressure between the instantaneous pressure at measurement pressure tap (i) and the static pressure from Pitot tube during the measurement process. The overall peak 1-h full-scale equivalent time history record is defined as the average of the maximum 10 values. This method provides reliable extreme peak for the recorded peaks. The mean pressure coefficients are taken as the averaged values of the samples in the time history. Finally, the sign of the wind pressure coefficient indicates the direction of wind pressure on the surface of building model; positive value indicates wind pressure acting towards the surface and negative value indicates wind pressure acting away from the surface (suction pressure). As another way of checking the measurement results, the dynamic pressure measured using the Cobra probe is compared with dynamic pressure using the pitot tube through the DSM module at every test.

Chapter 5. Experimental Results and Analysis

Eighteen wind tunnel test configurations were considered to investigate the velocity profiles and wind pressures on a flat roof low-rise building model, tested in the wind tunnel of Concordia University. The results of such tests are presented in this chapter. The distribution of the horizontal velocity and the most critical pressure coefficients on roof are important to define appropriate design wind loads. For simplicity, the pressure measurement results are provided in terms of non-dimensional pressure coefficients.

5.1 Mean wind speed and turbulence intensity

This section presents the velocity, and the turbulence intensity profiles that were conducted for different configuration trials on BLWT at Concordia university. As mentioned previously, many configurations have been used to simulate a velocity profile close to the non-synoptic wind profile. Moreover, this section compares the present study with the non-synoptic full-scale data (Hjelmfelt M, 1988), as well as with the atmospheric boundary layer wind tunnel data (H. Alrawashdeh and Stathopoulos, 2015).

In the first three trials, five configurations were tested, none of which met the target profile. It is important to note that, these configurations are important since they enhanced our understanding of the flow characteristics and the influence of obstacles on the produced profiles.

The results extracted from trial 4, which included nine different configurations, showed promise in simulating the wind profile of the downburst phenomenon. Figures 5-1 and 5-2 present comparisons of the velocity profiles of configurations II & III in trial 4. In the present study, the velocity U has been normalized by the maximum velocity at the step, U_m . The height Z is normalized by Z_m , i.e., the height where the maximum velocity at the step (U_m) occurs. The ABL data has been extracted from the study of (Hatem Alrawashdeh and Stathopoulos, 2015)

As previously stated, Trial 5 was established to further enhance the results obtained by trial 4. Figures 5-3 through 5-6 present comparisons of the velocity profiles of the best configurations that have met the target of the non-synoptic winds with the full-scale data and ABL (i.e., trial 5) at different configurations.

Figure 5-5 represents the configuration of two circular rods with the height of $H_1 = 15$ cm and $H_2 = 20$ cm respectively, and the distance in between of $X = 1$ m. This configuration provided the closest profile data to the full-scale data and the best configuration that could be used to simulate the thunderstorm phenomena. The atmospheric boundary layer (ABL) wind speed increases gradually until it reaches the maximum speed at the gradient height. Unlike the ABL, the experimental velocity data increase and reach a high wind speed at the step point. After reaching this point, the velocity starts to decrease. The maximum velocity at the step occurred at a very low height ~ 5 cm corresponding to a height of ~ 20 m in full-scale (assuming the length scale is 1:400), which agrees with the findings of the full-scale data (Hjelmfelt, 1988).

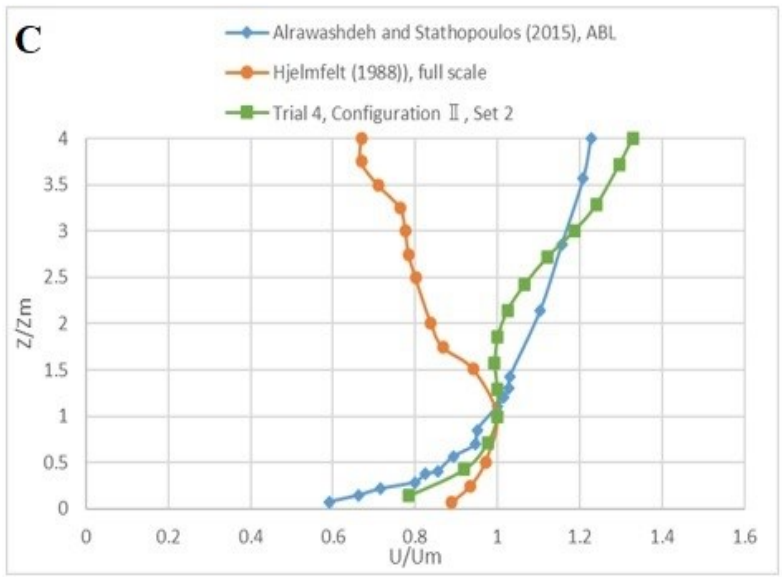
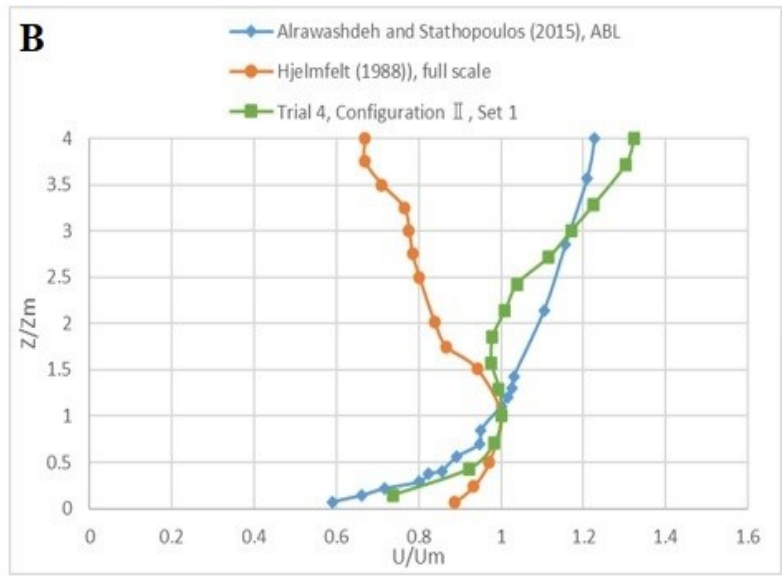


Figure 5-1 Velocity profile of trial 4, Configuration II; A) Test Configuration, B) Set 1, C) Set 2.

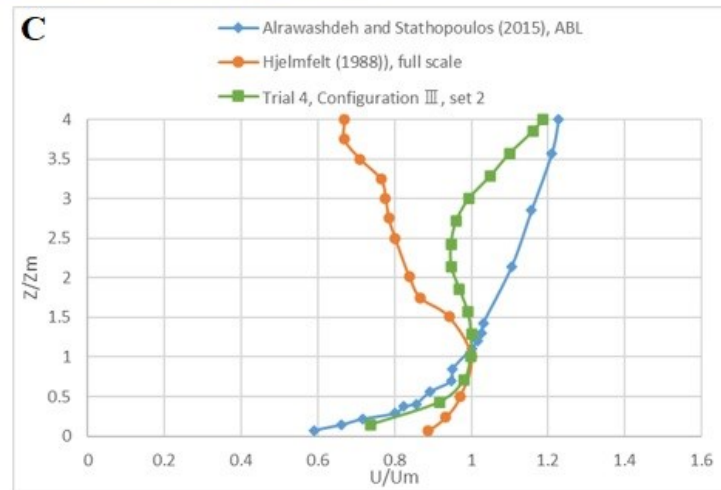
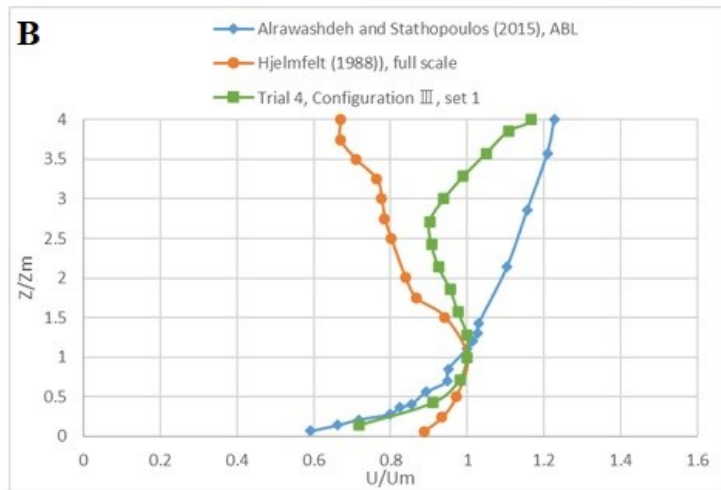


Figure 5-2 Velocity profile of trial 4, Configuration III; A) Test configuration, B) Set 1, C) Set 2.



—◆— Alrawashdeh and Stathopoulos (2015), ABL
 —●— Hjelmfelt (1988)), full scale
 —■— Trial 5, Configuration I

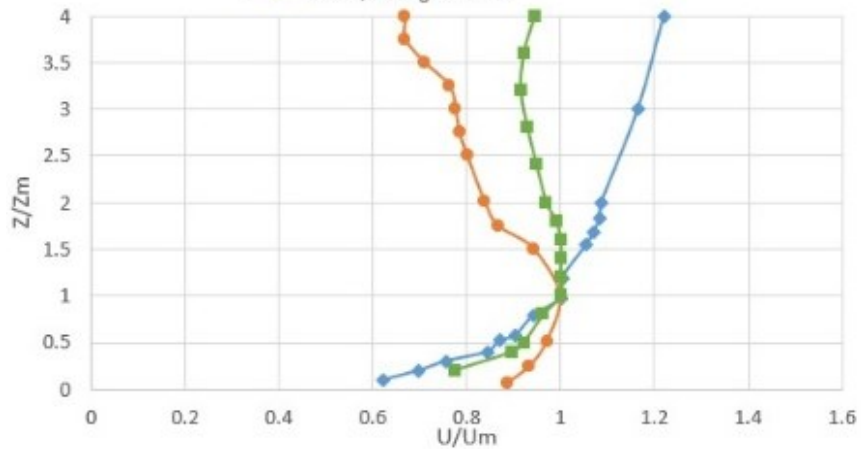


Figure 5-3 Velocity profile of trial 5, Configuration I. (H1=15 cm, H2=20 cm, X=2 m)



—◆— Alrawashdeh and Stathopoulos (2015), ABL
 —●— Hjelmfelt (1988)), full scale
 —■— Trial 5, Configuration II

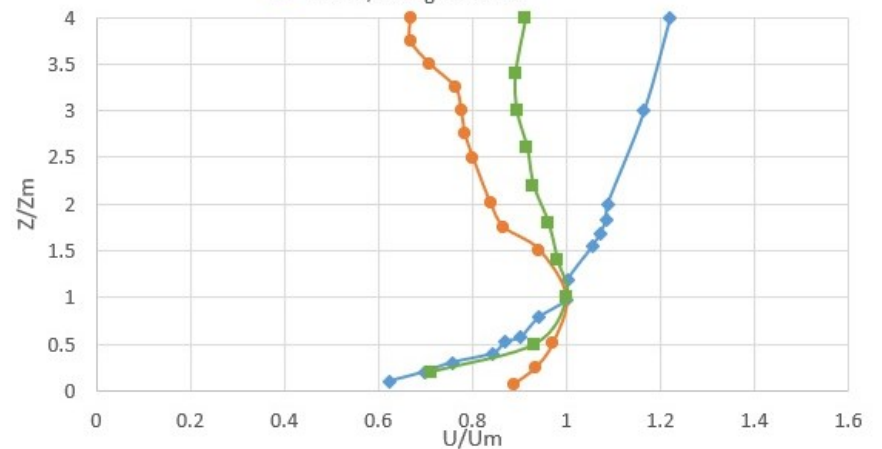


Figure 5-4 Velocity profile of trial 5, Configuration II. (H1=15 cm, H2=20 cm, X=1.5 m)

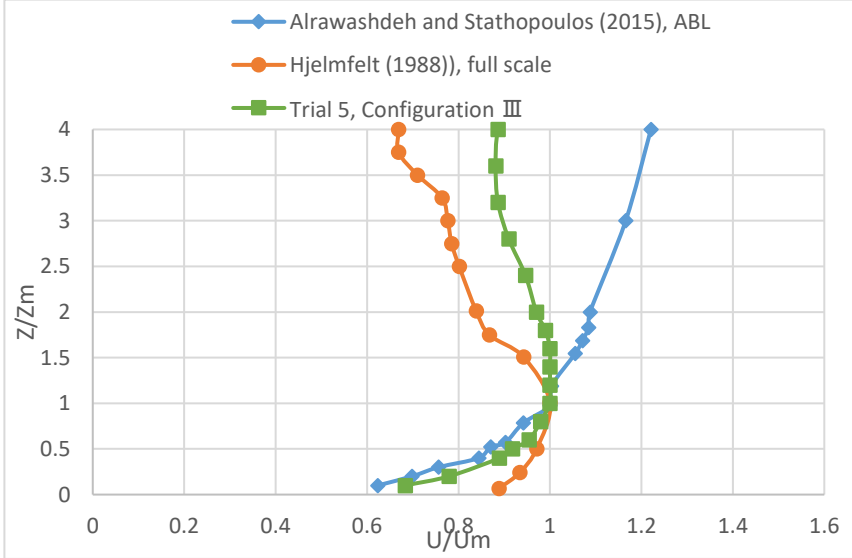


Figure 5-5 Velocity profile of trial 5, Configuration III. (H1=15 cm, H2=20 cm, X=1 m)

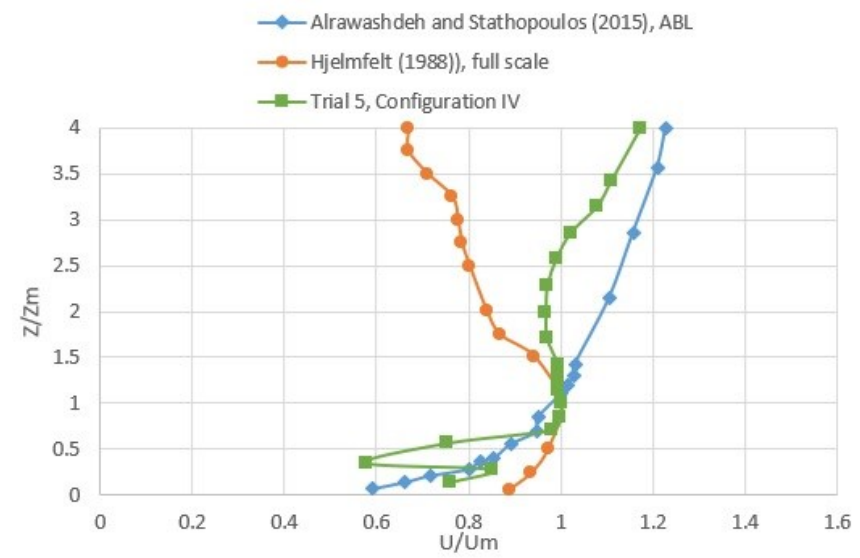


Figure 5-6 Velocity profile of trial 5, Configuration IV. (H1=15 cm, H2=0 cm, X=2 m)

Figure 5-7 presents a quantitative comparison of the velocity profiles measured in the present study (Trial 5-Configuration III), with the previous studies of downburst and the full-scale and ABL data. As shown in the figure, except for the ABL profile, all the velocity profiles have the same trend as the thunderstorm phenomena profile. However, the comparison also shows differences in the fluctuation of the velocity among the studies. This might be due to the nature of the flow and the differences in the simulation characteristics of the studies as shown in Table 5-1.

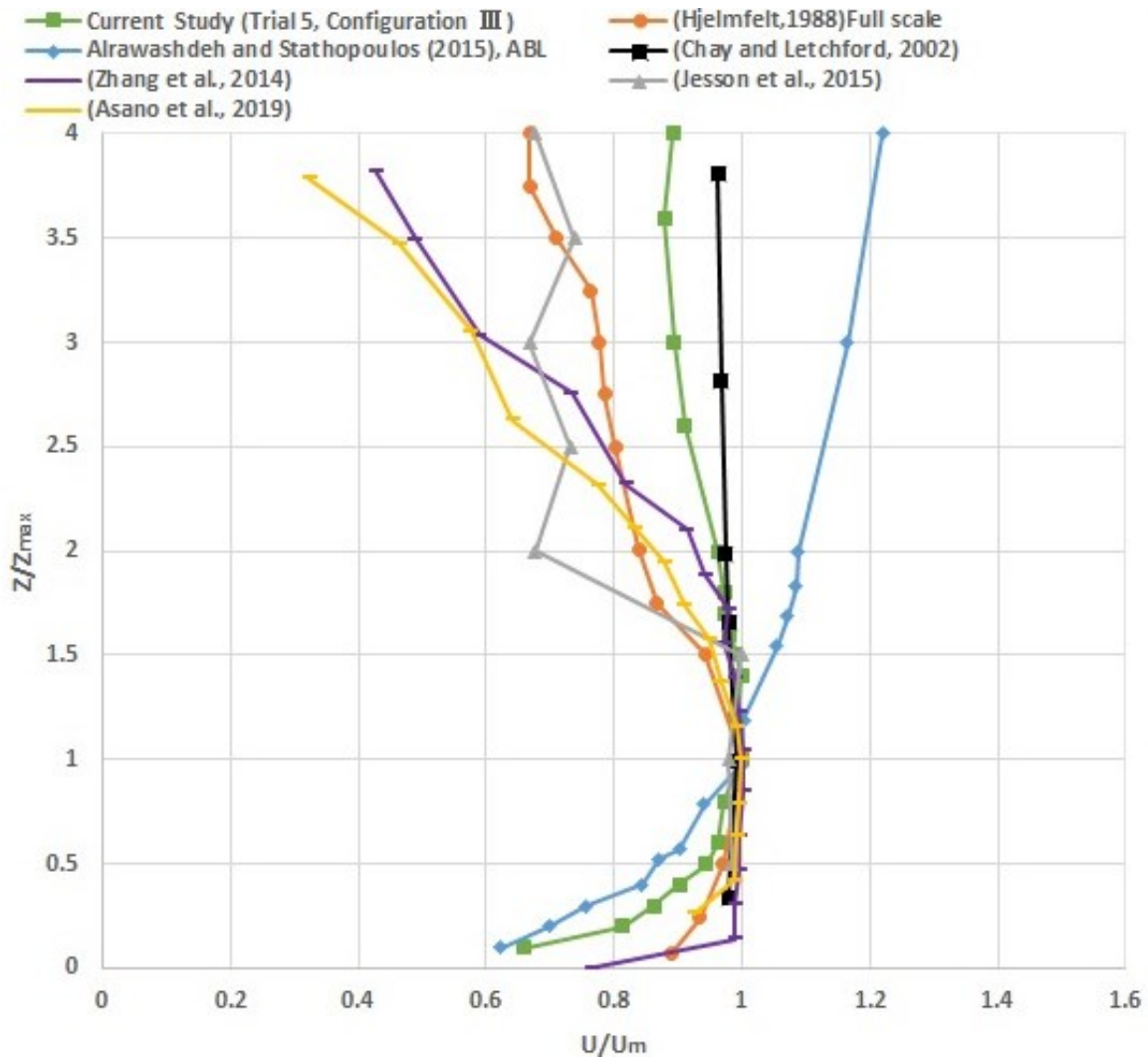


Figure 5-7 Comparison of the vertical wind velocity profiles between the present experiment and the corresponding previous studies.

Table 5-1 Downburst physical simulation characteristics of the previous studies

Study	(Chay and Letchford, 2002)	(Zhang et al., 2014)	(Jesson et al., 2015)	(Asano et al., 2019a)
Flow	steady impinging-jet	steady impinging-jet	Pulsed impinging-jet	Pulsed impinging-jet
Jet diameter D (m)	0.51	0.6	1	0.6
Cube size (mm)	30	45	60	Flat roof 80*80*40
Geometric Scale	1:3000	1:650	1:1600	1:2000
Blockage ratio	0.68%	0.258%	1.23%	2.26%
Nozzle Height (h)	1.7D	2D	2D	1.67D
X/D	1	1	1.5	1
V_{max}/V_{jet}	1	1.2	1.6	1.38
Z_{max} (mm)	5.5	36.6	20	15
D/B	17	13.3	16.7	7.5
H/X	0.0588	0.075	0.04	0.067
H/ Z_m	5.5	3.4	3	2.67
H/D	0.059	0.075	0.06	0.13
X/ Z_m	93	16.4	75	40

B: Model size.

H: Building Height.

X: Radial distance from the center.

Z_m : vertical distance above the ground where V_x max occurred.

h: Nozzle Height above the ground.

Blockage ratio: plan area / jet area.

$\frac{D}{B}$ = Jet Diameter

$\frac{H}{B}$ = model size B

$\frac{H}{X}$ = Building Height

$\frac{H}{D}$ = Radial distance from center

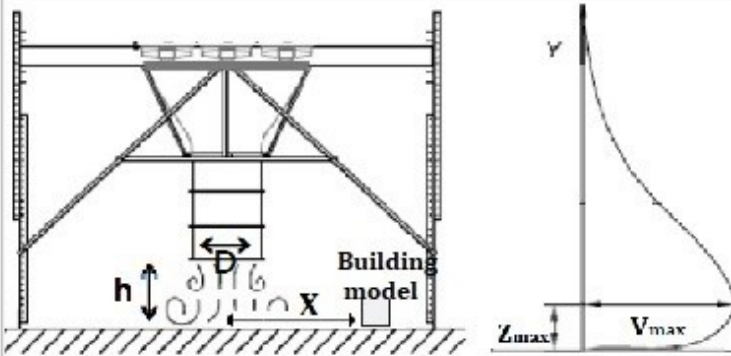
$\frac{H}{D}$ = Building Height

$\frac{H}{D}$ = Jet D

$\frac{H}{Z_m}$ = Building Height

$\frac{H}{Z_m}$ = Vertical distance above the ground

where U_{max} occurred



Birmingham university jet nozzle, after (McConville et al., 2009)

Furthermore, suburban exposure (exposure B) has been used to clarify the exposure effect of the velocity profile. Figure 5-8 indicates the wind speed in exposure B, which increases at a lower rate than it does in exposure C. This is because the roughness element height in exposure B is higher than that in the exposure C. Moreover, the shape of the profile has changed, and the step effect is lower in exposure B than exposure C.

Figure 5-9 presents the turbulence intensity (TI) of the present study compared with the previous studies of downburst and ABL winds. The turbulence intensity in those studies has been measured using the standard deviation divided by the mean velocity. TI results at the roof height of all the studies are very close, except, the ABL is a bit higher than the other studies. However, at a high level above the ground, the turbulence intensity is shown to be higher in Chay and Letchford (2002) than the other studies. Also, it is worth to note that exposure B has a higher TI than exposure C, as shown in Fig 5-9. This explains the changes in the roughness height.

Figure 5-10 presents the power spectral density of the longitudinal turbulence component calculated at height of 10 cm above the wind tunnel floor. Both power spectra provided were extracted at Concordia University wind tunnel for Configuration III of trial 5 (used in the present study) and for the standard open exposure (ABL). The experimental spectra of different wind events (i.e., ABL and downburst) are different. Clearly, the wind energy of the downburst profile is greater than the corresponding spectra of the ABL profile.

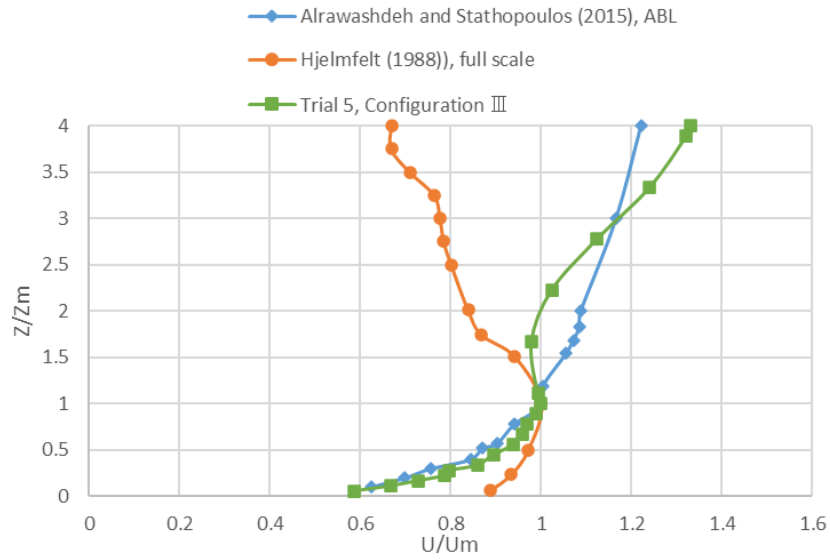


Figure 5-8 Velocity profile of exposure B.

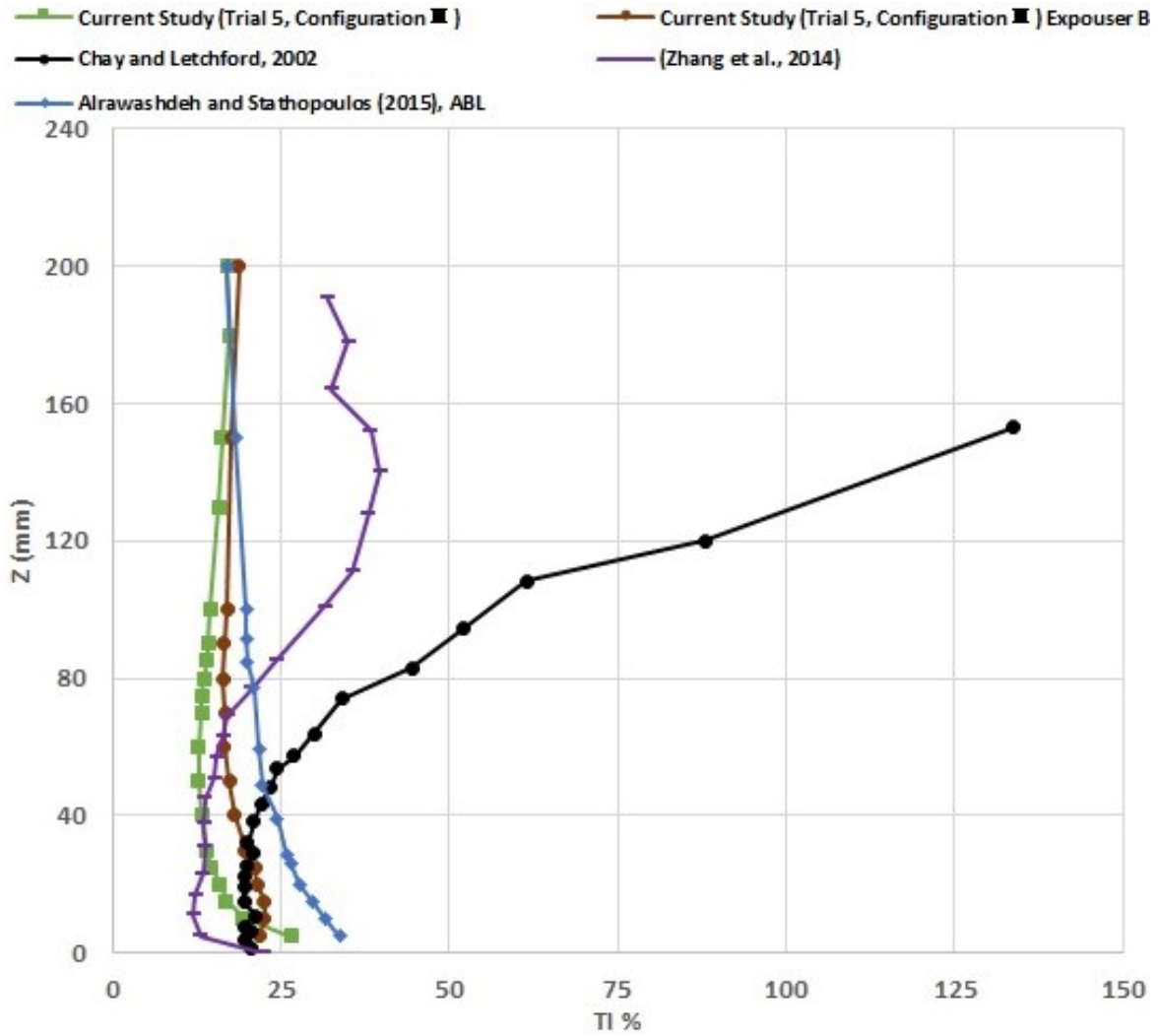


Figure 5-9 Comparison of the longitudinal turbulence intensity profiles between the present experiment and the corresponding previous studies

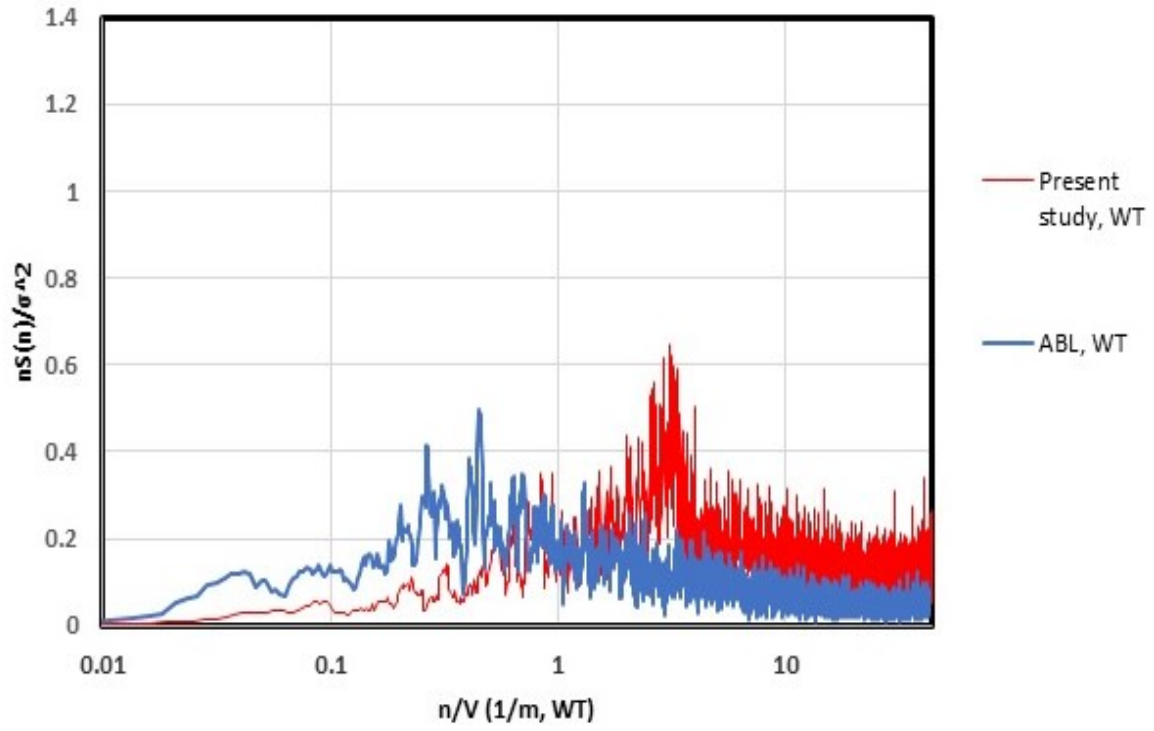


Figure 5-10 Power spectral density of longitudinal turbulence component evaluated at one-sixth the gradient height

5.2 Wind load measurements

In this section, the experimental findings are presented in terms of contours of most critical pressure coefficients over the roof, extreme local pressure coefficients for each wind direction. In addition, comparisons of the experimental results with previous studies of ABL and downburst are included.

5.2.1 Contours of the most critical pressure coefficients

The building models have been tested for 7 wind directions: 0° , 15° , 30° , 45° , 60° , 75° and 90° to obtain the most critical wind pressures on the roof of the building. Figures 5-11 through 5-14 show contours of most critical mean and peak pressure coefficients among all wind directions for two building heights, 5 m and 10 m.

The contours show wind pressure coefficients of the roof, which is the area equipped with pressure taps. All contours were created by the mapping software “surfer 22”, contour intervals are 0.2 for mean pressure coefficients, C_p , and 0.5 for peak pressure coefficients, $C_p C_g$. Contours of mean and peak pressure coefficients for each wind direction are presented in Appendix A and Appendix B.

As shown in the figures

, the pressure coefficients decrease from the highest value on the roof corner to relatively smaller pressure coefficients along the windward edges. The pressure coefficient values increase through the last part of the windward edge to reach higher value on the other corner of the roof than the middle part of the edge. Toward the interior zone along a line normal to the windward edge, the pressure coefficients decrease from the windward corner along the line. At the leeward corner, the pressure coefficient comes to increase, as shown in the figures.

These fluctuations of the pressure coefficients are due to the flow separation that happens at the windward edges and causes high wind pressures on corner and edge zones compared to those on the interior zone.

In addition, these figures show that the height of the building is a significant factor that affects the values of pressure coefficients. Thus, the taller the building the higher the pressure coefficients and the larger the area that receives high wind pressures. This is because of the higher wind velocity at the height of 5 cm than 2.5 cm on the velocity profile extracted from the wind tunnel.

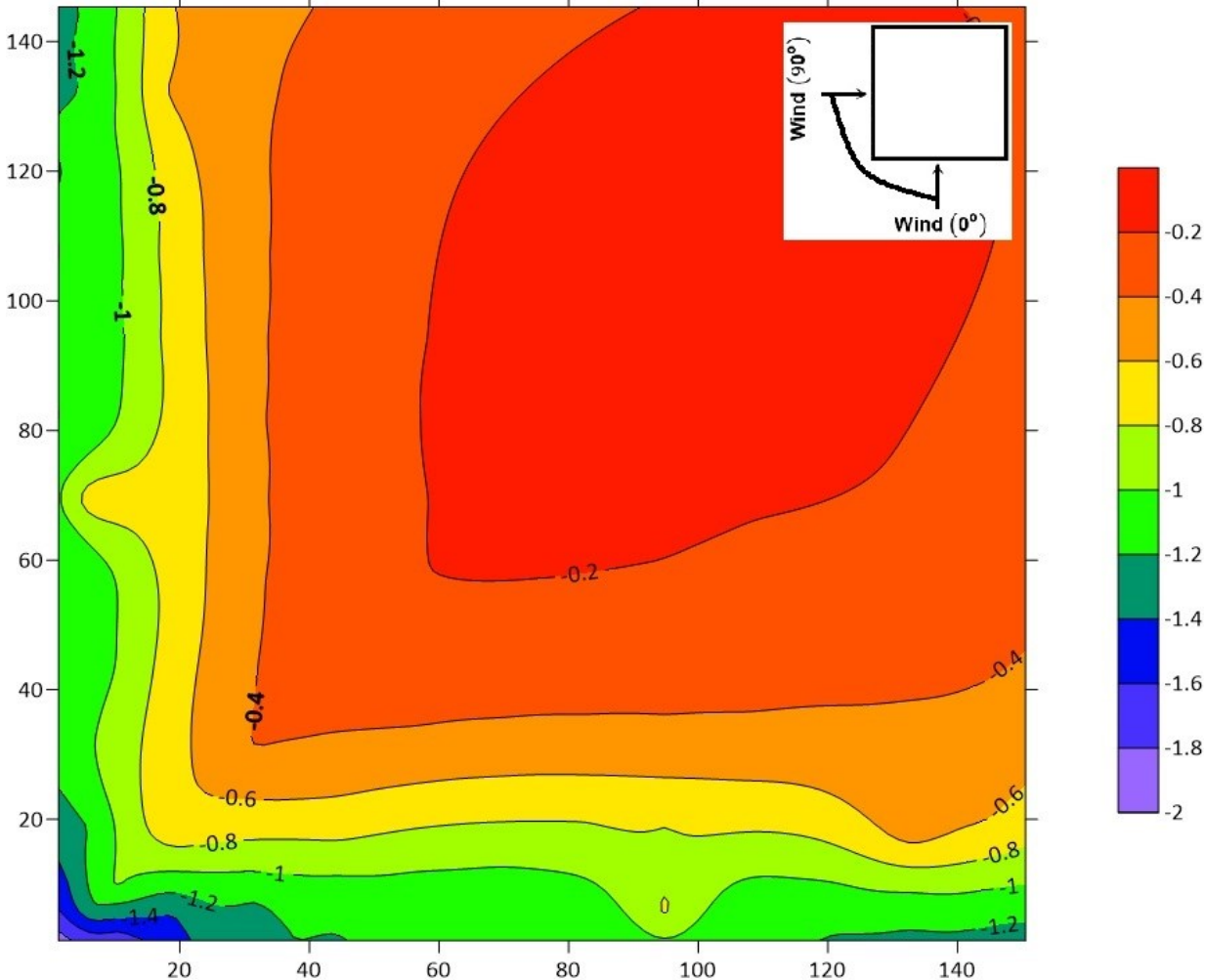


Figure 5-11 Contours of most critical mean pressure coefficients (C_p) for all wind directions ($H=10$ m)

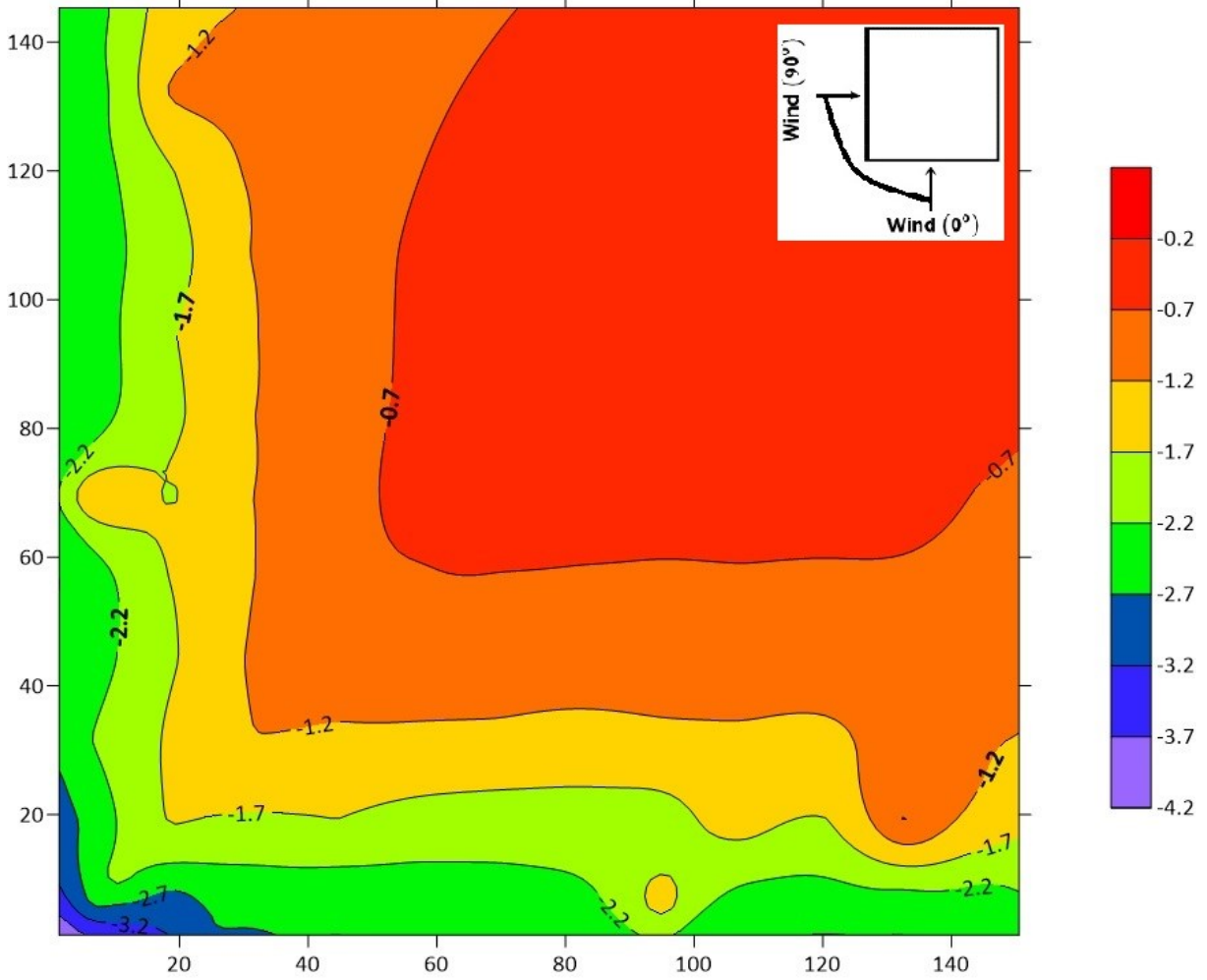


Figure 5-12 Contours of most critical peak pressure coefficients ($C_p C_g$) for all wind directions ($H=10$ m)

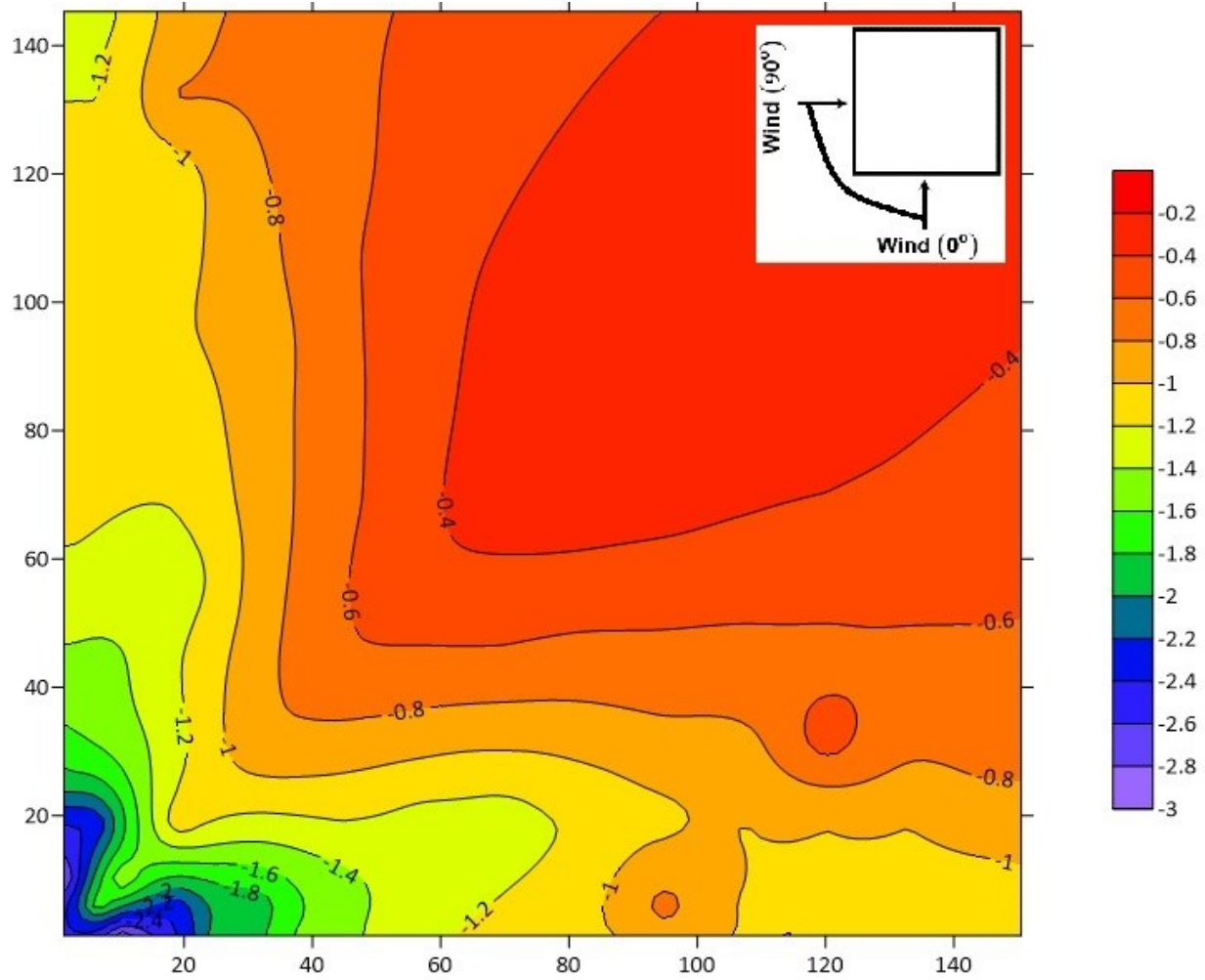


Figure 5-13 Contours of most critical mean pressure coefficients (C_p) for all wind directions ($H=20$ m)

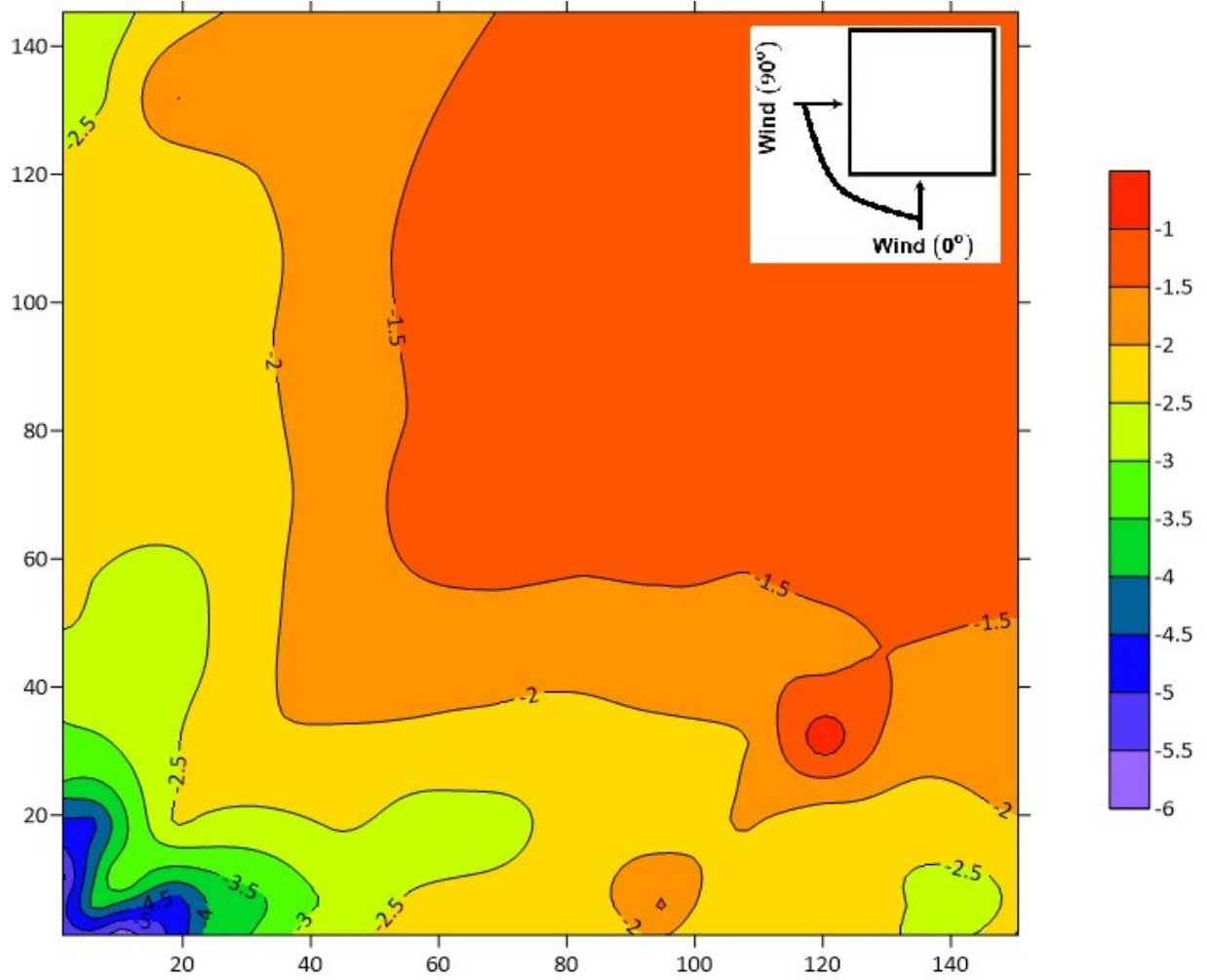


Figure 5-14 Contours of most critical peak pressure coefficients ($C_p C_g$) for all wind directions ($H=20$ m)

5.2.2 Local pressure coefficients

The variations of extreme negative peak and mean pressure coefficients on windward edge and corner of the roofs were evaluated as a function of the wind direction and compared for two buildings height. Figure 5-15 presents the mean pressure coefficients and the extreme negative peak pressure coefficients over the edge zone, whereas Figure 5-16 presents the mean pressure coefficients and the extreme negative peak pressure coefficients over the corner zone with the wind direction. The comparisons were carried out for wind directions between 0° and 90° with 15° increments.

Figure 5-15 shows the fluctuation of the extreme negative peak and mean pressure coefficients with the wind direction along the windward edge. The minimum pressure coefficient values are observed at the building orientation of 15° and 30° . Moreover, the figure shows that the building height has a significant effect on the variation of the pressure coefficients with the building orientation. For the building of 20 m, C_{pCg} at the wind azimuths of 0° and 30° was -2.8 and -4.9 respectively, whereas for the building height of 10 m, C_{pCg} for the same wind azimuths was -2.7 and -3 respectively.

Figure 5-16 presents the magnitude of extreme negative peak and mean pressure coefficients over the windward corner. Values of pressure coefficients vary with the wind direction, the variations of the peak pressure coefficient values for the building height of 20 m are higher than the values of the building height of 10 m. It should be noted that the values of the windward corner are higher than the windward edge zone, thus the windward corner is the most critical zone that could be affected by the wind.

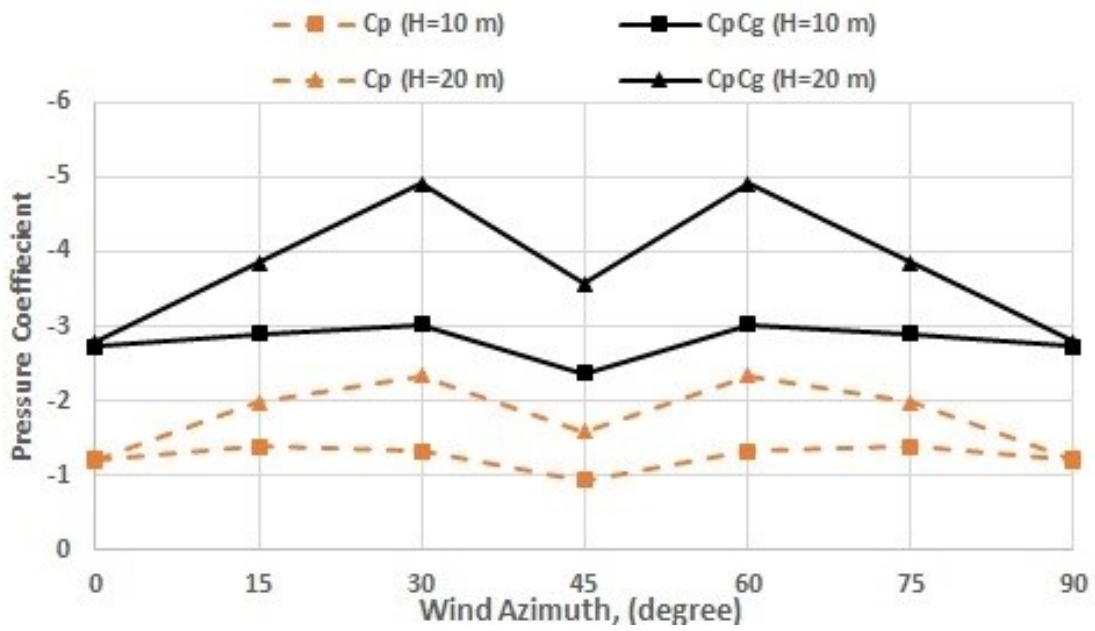
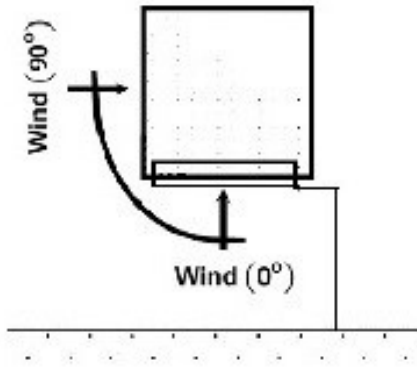


Figure 5-15 Extreme negative peak and mean pressure coefficients on windward edge of the building versus wind direction.

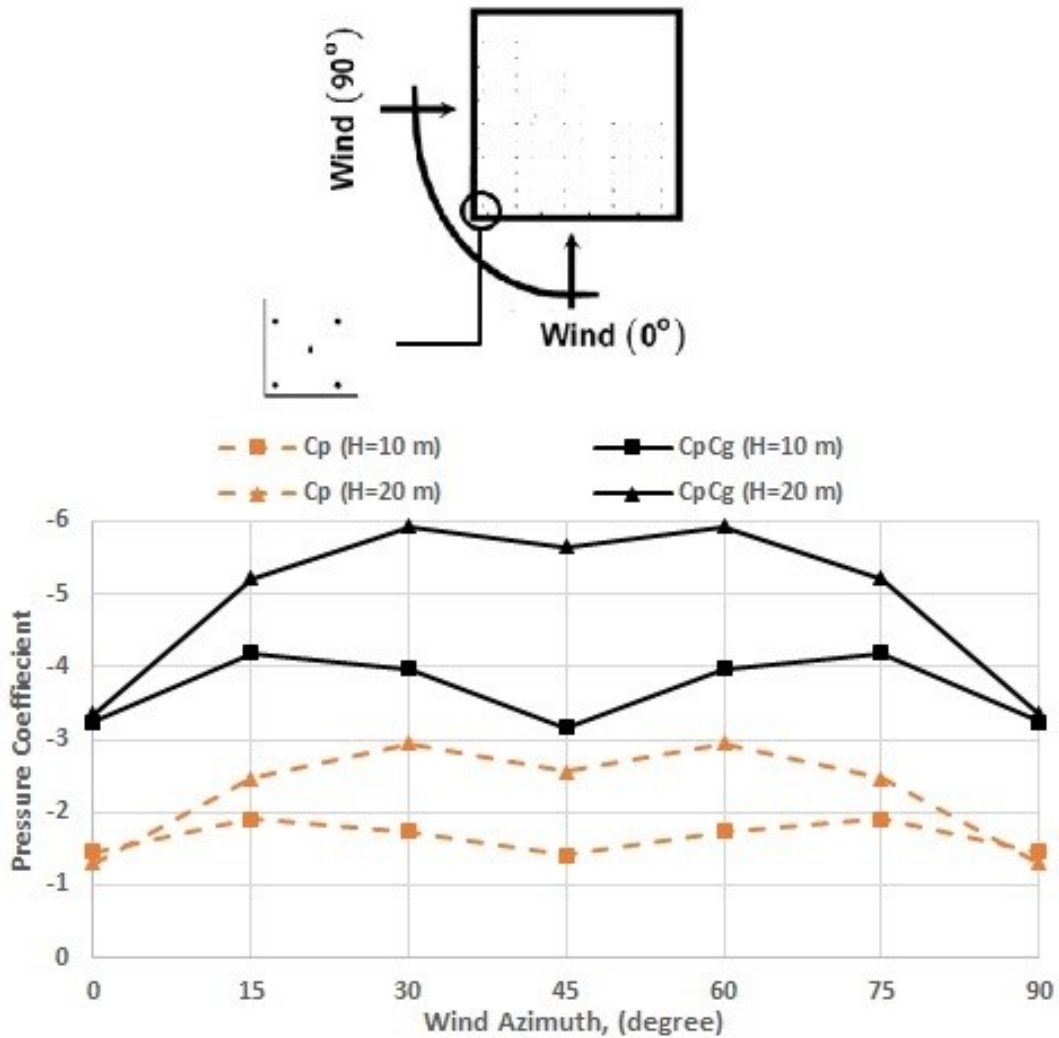


Figure 5-16 Extreme negative peak and mean pressure coefficients on windward corner of the building versus wind direction.

Figures 5-17 and 5-18 show comparisons of the peak and mean pressure coefficients of two building heights with different pressure taps group. Figure 5-17 presents the values of the pressure taps line near the concurrent roof edge for 45° wind direction, whereas Figure 5-18 presents the values of the centerline pressure taps along the roof for 0° wind direction.

Figure 5-17 shows that the two building heights have the same behavior in general. The higher building has slightly higher mean and peak pressure coefficients at $Y/L < 0.4$, except that at the windward corner the variation of the mean and peak values was high. CpCg of the building of 20

m was -5.6 comparing with -3.2 for the building height of 10 m, this is attributed to the height difference of the buildings and the development of the conical vortices along the edge when the wind strikes at an azimuth of 45° .

Figure 5-18 shows the highest suction near the windward edge decreases with increasing distance from the windward edge. The variation of the peak and mean values of the different height buildings are also decreased with the distance from the windward edge.

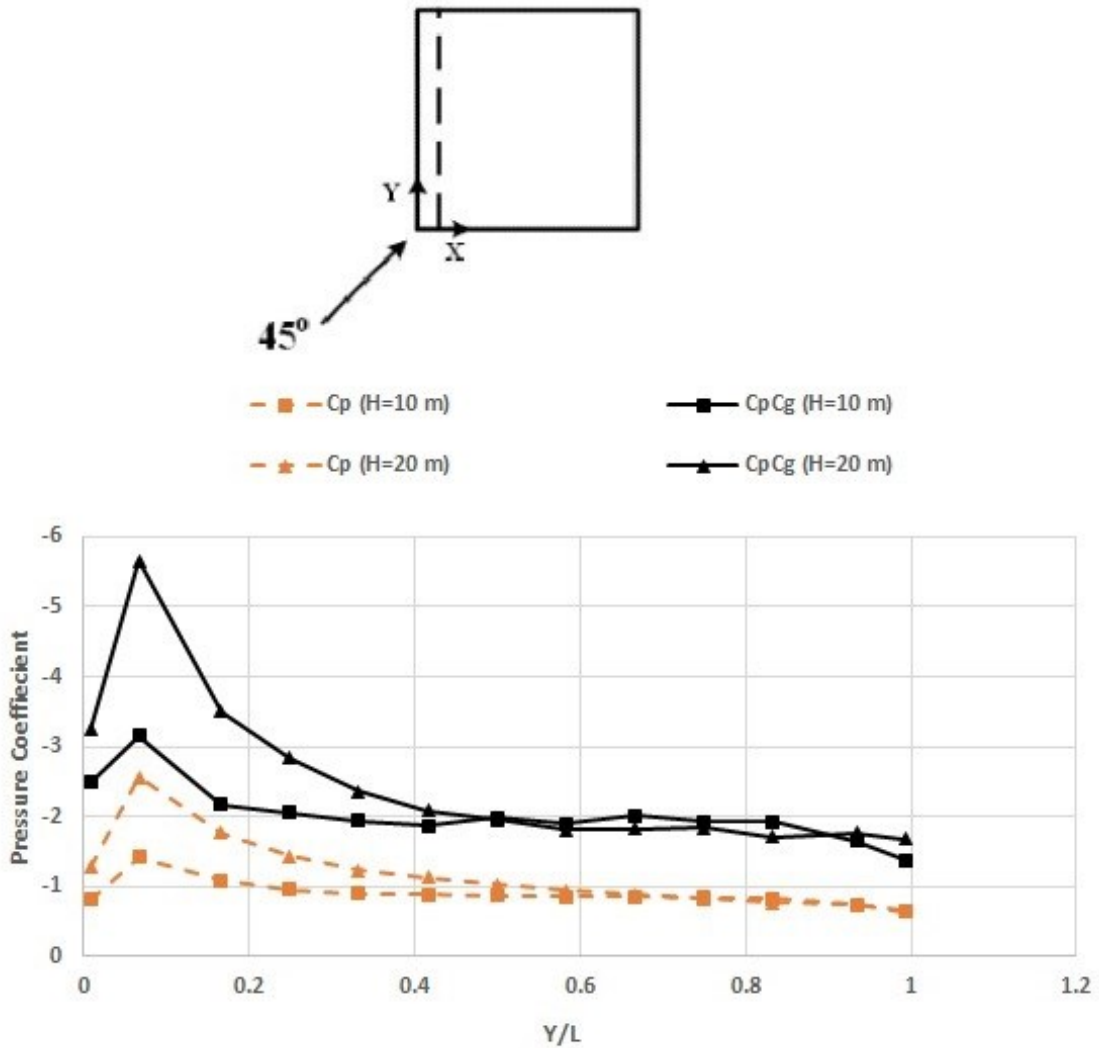


Figure 5-17 Variation of wind pressure coefficients along the line at the concurrent edge for 45° wind direction

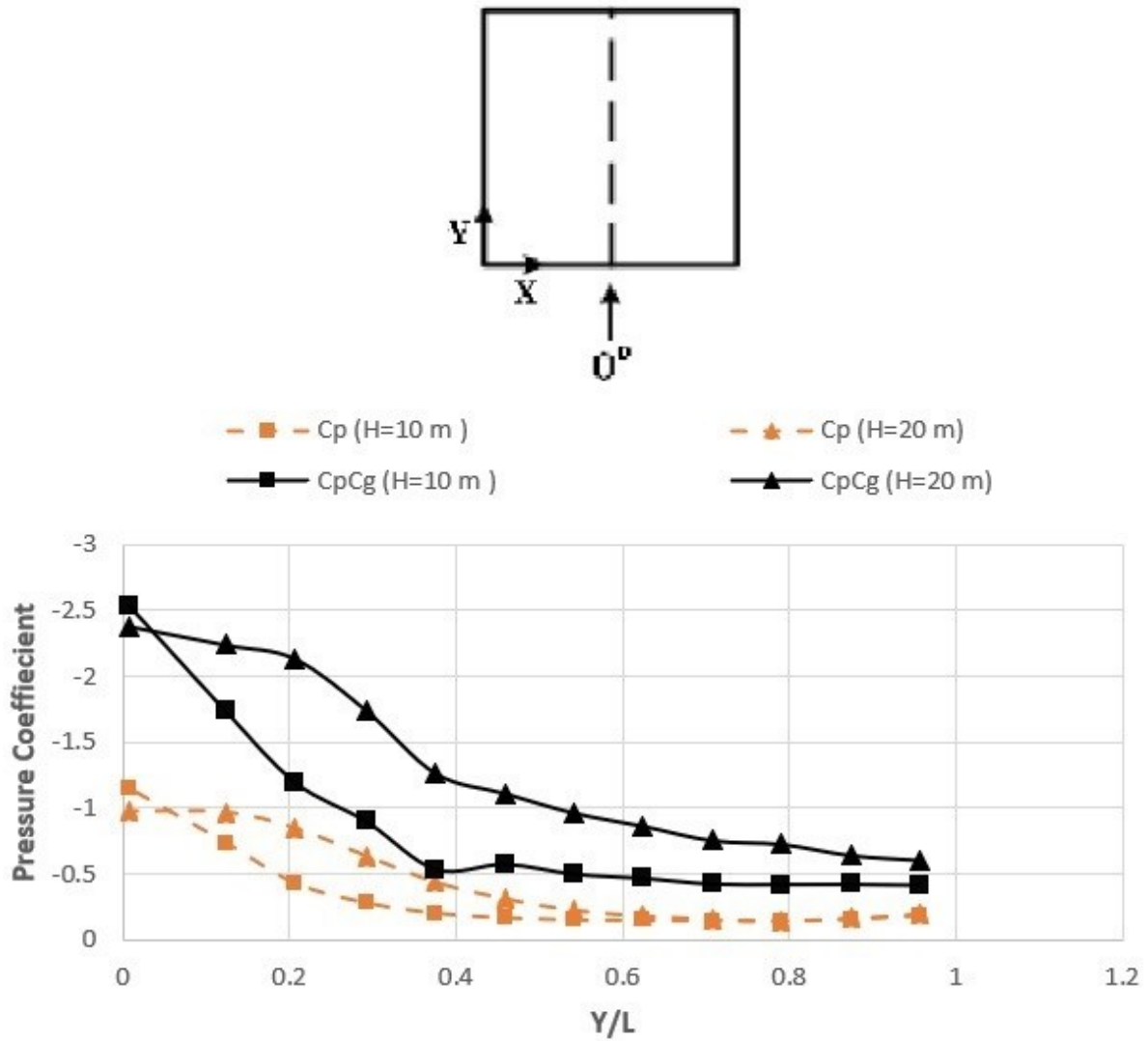


Figure 5-18 Variation of wind pressure coefficients along the roof centerline for 0° wind direction

5.2.3 Comparison with ABL previous studies

The building height of 10 m has been selected in this section to compare the results of the present study with the atmospheric boundary layer previous study of Alrawashdeh and Stathopoulos (2015), which used the same model utilized in the present study. The comparisons are presented in Figure 5-19 and Figure 5-20.

Figure 5-19a presents the variation of the mean and peak pressure coefficients along the roof centerline for 0° wind direction. Results of both studies are close with a bit higher values reported by Alrawashdeh and Stathopoulos (2015) at the first half of the roof ($Y/L < 0.5$).

Figure 5-19b presents the variation of the mean and peak pressure coefficients along the line at the concurrent edge for 45° wind direction. Disagreement appears of the peak and mean values at the leading edge, perhaps because of the development of the conical vortices over the edge. Afterward, the mean pressure coefficient values are in very good agreement along the entire line; whereas the peak pressure coefficient values after a third of the entire line ($Y/L > 0.3$) are in better agreement.

Figure 5-20 presents comparison of the extreme mean and peak pressure coefficients for the roof edge and the roof corner zones with the different wind direction. The values of the mean pressure coefficient are in very good agreement. The values of the peak have some differences as the most critical values were recorded at the wind direction of 30° in the present study, whereas it was recorded at the wind direction of 0° in Alrawashdeh and Stathopoulos (2015). At the corner zone, as of the edge zone, the mean pressure values are in very good agreement. The peak values pattern are also in good agreement with a bit higher values in Alrawashdeh and Stathopoulos (2015).

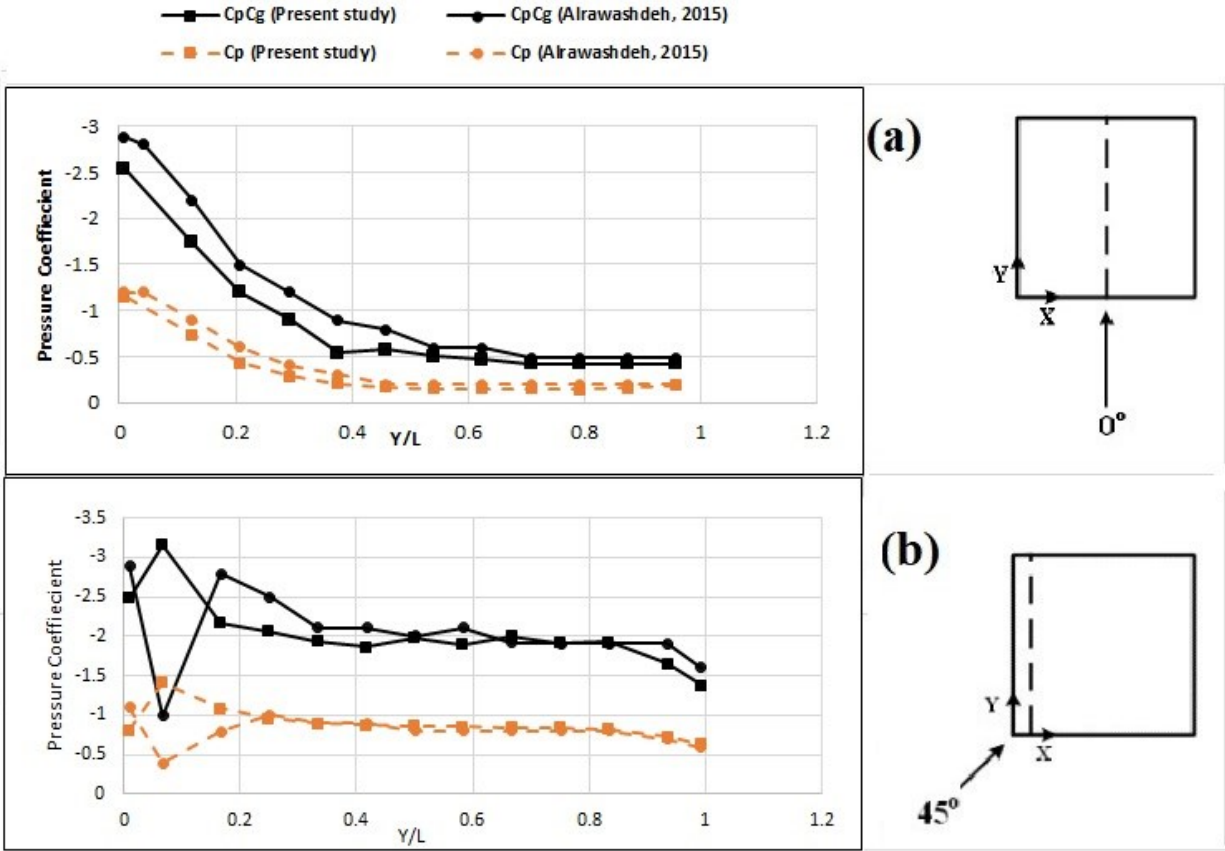


Figure 5-19 Comparison between the present study and Alrawashdeh and Stathopoulos (2015),
 a) Variation of wind pressure coefficients along the roof centerline for 0° wind direction; b)
 Variation in wind pressure coefficients along the line at the concurrent edge for 45° wind
 direction

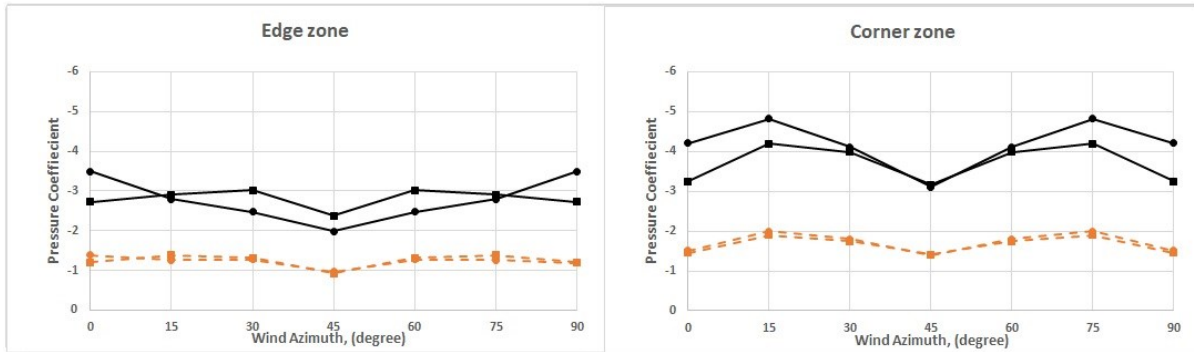
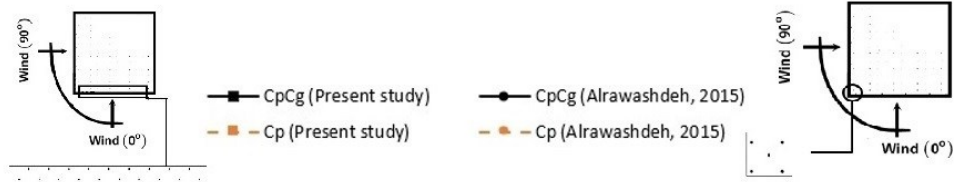


Figure 5-20 Comparison of extreme peak and mean pressure coefficients on the windward edge zone and corner zone between the present study and Alrawashdeh and Stathopoulos (2015)

Figure 5-21 presents contour comparisons of the peak pressure coefficients for 45° wind direction. The data show that, in the present study, the pressure coefficient values at the corner are lower than those reported in Alrawashdeh and Stathopoulos, (2015), whereas the values away from the corner are slightly higher than those reported in the ABL study.

Conclusively, the present study shows differences in the peak pressure coefficients compared to the ABL study of Alrawashdeh and Stathopoulos (2015). The differences in the pressure distribution could be attributed to the different velocity profiles defined in each study. However, the mean pressure coefficients obtained in both studies are very similar.

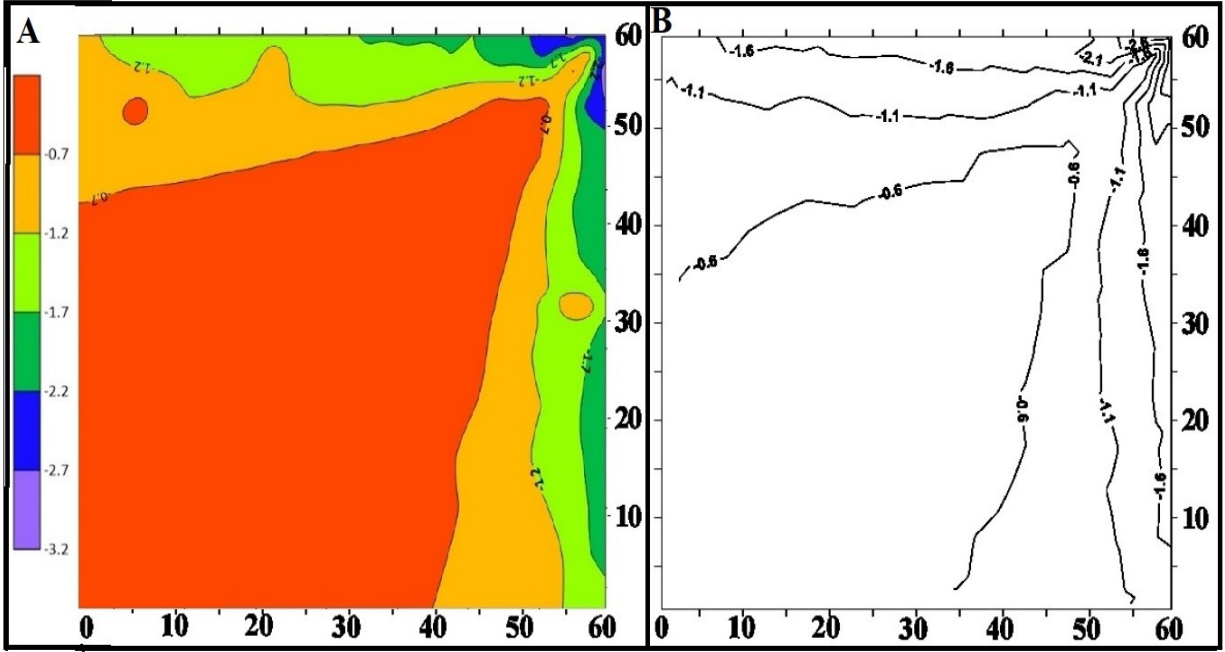


Figure 5-21 Contour plots of peak pressure coefficient at 45° wind direction; A) Present study, B) Alrawashdeh and Stathopoulos (2015)

5.2.4 Comparison with downburst previous studies

The building height of 50 mm (20 m full-scale) has been selected in this section to compare the results of the present study with the downburst studies. These comparisons are presented in Figure 5-22 and Figure 5-23. It should be noted that the values from the present study were converted to 3-s gust wind for comparison purposes.

Figure 5-22 presents the comparison of the present study with the study of Jesson et al (2015). A 60 mm cubic building was used in this study to investigate the wind load caused by downburst phenomena.

Figure 5-22a shows the variation of the mean pressure coefficients along the roof windward edge for 0° wind direction, the comparison shows a very good agreement over the left corner ($X/B < 0.2$). Somewhat higher values were reported in the study of Jesson et al. (2015) over the entire line. Figure 5-22b shows the variation in mean pressure coefficients along the line at the concurrent edge 45° wind direction, the maximum value of Jesson et al. (2015) occurred farther from the leading edge compared with the present study. The pressure coefficient values in Jesson et al. (2015) are higher than those in the present study. This is due to the lower velocity that occurred at the higher building height in the downburst wind speed profile.

Figure 5-23 presents a comparison of mean pressure coefficients along the roof centerline for 0° wind direction between the present study and the previous downburst studies wind. The figure shows a good agreement at the roof leading edge, the values reported in the present study are very close to those in the other studies at first quarter of the roof ($Y/L < 0.25$). Less agreement appears after $Y/L = 0.25$ where the pressure coefficient of the present study decreases along the entire line, this is maybe due to the differences of the simulation mechanism.

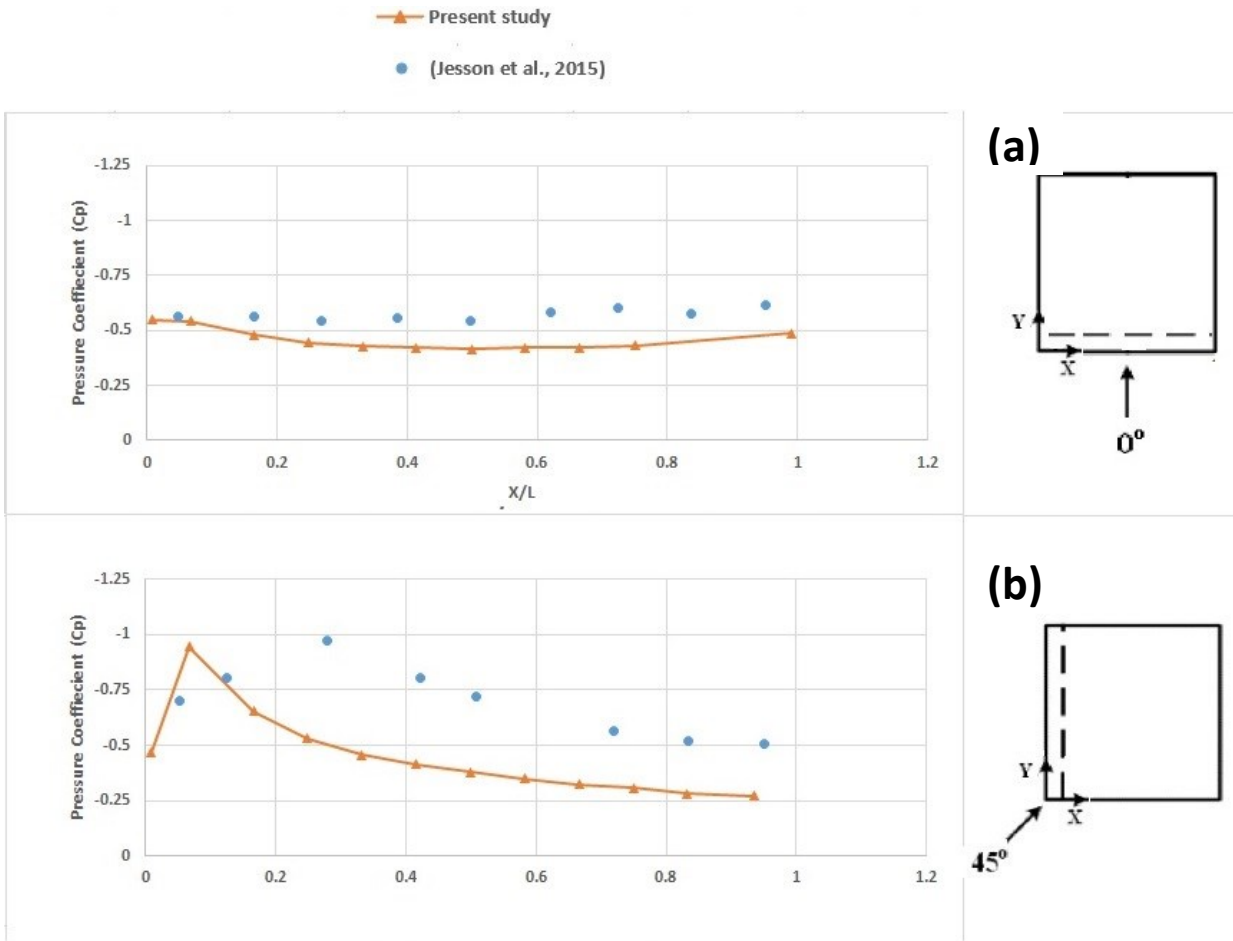


Figure 5-22 Comparison between the present study and Jesson et al, 2015. a) Variation of wind pressure coefficients along the roof windward edge; b) Variation in wind pressure coefficients along the line at the concurrent edge 45° wind direction

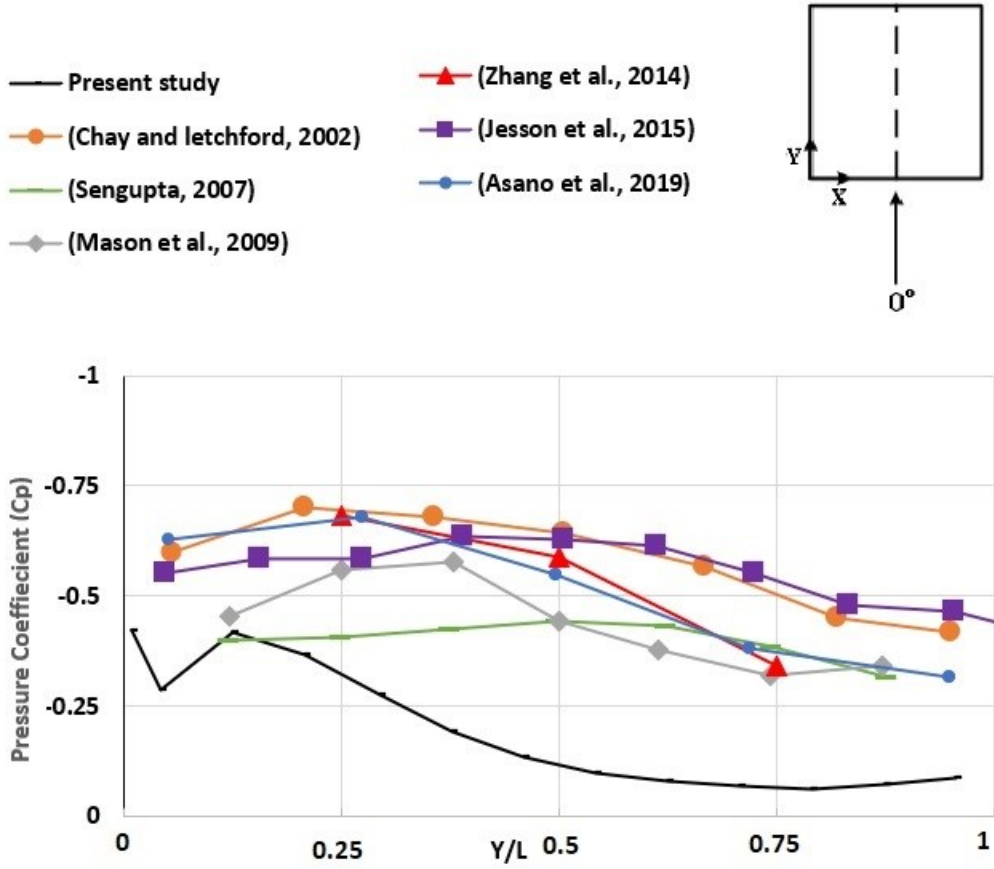


Figure 5-23 Comparison of mean pressure coefficients along the roof centerline for 0° wind direction between the present study and the previous downburst wind studies

Chapter 6. Conclusions and future work

6.1 Conclusions

Non-synoptic wind damage is a threat not only on buildings, as several kinds of damage occurred, also the economic and fatality losses increase year after year. The necessity of examining wind loads on buildings under the effect of the downburst arises because the wind engineering codes and standards do not generally consider non-synoptic winds in their current versions.

The wind tunnel at Concordia University was used to simulate the downburst phenomena. After many trials with different configurations, the wind speed profile of the downburst was produced and compared with the available full-scale data.

A model of a building with plane dimensions of 60 m x 60 m and two different heights: 10 m and 20 m was tested in the wind tunnel of Concordia University for seven wind directions. The experimental results are presented in terms of contours of most critical pressure coefficients, extreme local pressure coefficients versus wind direction. The results were compared with ABL and downbursts past studies. The following are conclusive remarks of the present study:

1. The peak pressure coefficients on the roofs' leading edge under downburst flows show higher values than the ABL flow at critical wind direction (i.e., 45°); whereas the most critical wind load values on the roof corners and edges are comparable for the same building model under the considered wind events.
2. Wind loads developed within the roof corner and edge zones for the building height of 10 m are very close, whereas the values of the building height of 20 m are different. Thus, the building height is a very important factor in defining the loading zones of the roofs.
3. The distribution of the wind pressure coefficients only within the windward edge is almost comparable with the data of the previous studies on downbursts. This comparison led to the necessary work that could help to provide more data to understand how the buildings could behave under different wind phenomena.

Ultimately, in this study a different mechanism was used to simulate the downburst phenomena. Also, significant differences were noticed among the results of the previous studies on the downburst. These differences may be due to the differences of the simulation mechanism, since most of the studies have used different simulation parameters that could affect the flow field, and hence, the wind-induced pressures.

6.2 Future work

- In order to enhance the wind speed profile, the Particle Image Velocimetry system (PIV) should be used to get accurate and detailed measurements of the velocity flow near the ground.
- The current study concerned square roofs with a single plan dimension (60 m). Thus, it is recommended to test building models with different shape and plan dimensions.

References

- Aldoum, M., Stathopoulos, T., 2020. Wind loads on low-slope roofs of buildings with large plan dimensions. *Eng. Struct.* 225, 111298. <https://doi.org/10.1016/j.engstruct.2020.111298>
- Allen, D.E., 1986. Tornado damage in the Barrie/Orangeville area, Ontario, May 1985. *Build. Res. Note 240*, Inst. Res. Constr. Natl. Res. Counc. Canada, Ottawa.
- Allen, D.E., 1984. Tornado damage at Blue Sea Lake and Nicabong, Quebec, July 1984. *Build. Res. Note 222*, Inst. Res. Constr. Natl. Res. Counc. Canada.
- Alrawashdeh, Hatem, Stathopoulos, T., 2015. Wind pressures on large roofs of low buildings and wind codes and standards. *J. Wind Eng. Ind. Aerodyn.* 147, 212–225. <https://doi.org/10.1016/j.jweia.2015.09.014>
- Alrawashdeh, H., Stathopoulos, T., 2015. Wind pressures on flat roof edges and corners of large low buildings. Concordia University, Montreal, Quebec, Canada, Master's Thesis.
- Asano, K., Iida, Y., Uematsu, Y., 2019a. Laboratory study of wind loads on a low-rise building in a downburst using a moving pulsed jet simulator and their comparison with other types of simulators. *J. Wind Eng. Ind. Aerodyn.* <https://doi.org/10.1016/j.jweia.2018.11.034>
- Asano, K., Iida, Y., Uematsu, Y., 2019b. Laboratory study of wind loads on a low-rise building in a downburst using a moving pulsed jet simulator and their comparison with other types of simulators. *J. Wind Eng. Ind. Aerodyn.* 184, 313–320. <https://doi.org/10.1016/j.jweia.2018.11.034>
- ASCE/SEI 7-10, 2010. Minimum design loads and associated criteria for buildings and other structures. Structural Engineering Institute of ASCE, Reston, VA.
- ASCE 7, 2017. Minimum design loads and associated criteria for buildings and other structures, Minimum Design Loads and Associated Criteria for Buildings and Other Structures. <https://doi.org/10.1061/9780784414248>
- Cao, S., Wang, J., Cao, J., Zhao, L., Chen, X., 2015. Experimental study of wind pressures acting on a cooling tower exposed to stationary tornado-like vortices. *J. Wind Eng. Ind. Aerodyn.* 145, 75–86. <https://doi.org/10.1016/j.jweia.2015.06.004>

- Case, J., Sarkar, P., Sritharan, S., 2014. Effect of low-rise building geometry on tornado-induced loads. *J. Wind Eng. Ind. Aerodyn.* 133, 124–134.
<https://doi.org/10.1016/j.jweia.2014.02.001>
- Chay, M.T., Letchford, C.W., 2002. Pressure distributions on a cube in a simulated thunderstorm downburst - Part A: Stationary downburst observations. *J. Wind Eng. Ind. Aerodyn.* 90, 711–732. [https://doi.org/10.1016/S0167-6105\(02\)00158-7](https://doi.org/10.1016/S0167-6105(02)00158-7)
- Church, C.R., Snow, J.T., Baker, G.L., Agee, E.M., 1979. Characteristics of tornado-like vortices as function of swirl ratio: A Laboratory Investigation. *Journal of Atmospheric Sciences.* 36. 1755-1776. [https://doi.org/10.1175/1520-0469\(1979\)036<1755:COTLVA>2.0.CO;2](https://doi.org/10.1175/1520-0469(1979)036<1755:COTLVA>2.0.CO;2).
- Davenport, A.G., Isyumov, N., 1967. The application of the boundary layer wind tunnel to the prediction of wind loading. *Proc. Int. Res. Semin. Wind Eff. Build. Struct.* 201-230.
- Davies-Jones, R.P., 1973. The Dependence of Core Radius on Swirl Ratio in a Tornado Simulator. *J. Atmos. Sci.* [https://doi.org/10.1175/1520-0469\(1973\)030<1427:tdocro>2.0.co;2](https://doi.org/10.1175/1520-0469(1973)030<1427:tdocro>2.0.co;2)
- Doswell, C.A., Carbin, G.W., Brooks, H.E., 2012. The tornadoes of spring 2011 in the USA: An historical perspective. *Weather* 67, 88–94. <https://doi.org/10.1002/wea.1902>
- FEMA, 2015. Safe rooms for tornadoes and hurricanes: Guidance for community and residential safe rooms. P-361, Third Edition. Washington, DC (<https://www.fema.gov/media-library/assets/documents/3140>).
- Fujita, T.T., 1985. The Downburst–Microburst and Macroburst. Reports of Projects NIMROD and JAWS, SMRP. Chicago, Univ. Chicago Press. 124.
- Fujita, T.T., 1981. Tornadoes and downbursts in the context of generalized planetary scales. *J. Atmos. Sci.* [https://doi.org/10.1175/1520-0469\(1981\)038<1511:TADITC>2.0.CO;2](https://doi.org/10.1175/1520-0469(1981)038<1511:TADITC>2.0.CO;2)
- Haan, F.L., Balaramudu, V.K., Sarkar, P.P., 2010. Tornado-induced wind loads on a low-rise building. *J. Struct. Eng.* 136, 106–116. [https://doi.org/10.1061/\(ASCE\)ST.1943-541X.0000093](https://doi.org/10.1061/(ASCE)ST.1943-541X.0000093)
- Haan, F.L., Sarkar, P.P., Gallus, W.A., 2008. Design, construction and performance of a large

- tornado simulator for wind engineering applications. *Eng. Struct.* 30, 1146–1159.
<https://doi.org/10.1016/j.engstruct.2007.07.010>
- Hangan, H., 2014. The Wind Engineering Energy and Environment (WindEEE) Dome. *Wind Eng. JAWE* 39, 350–351.
- Hangan, H., Refan, M., Jubayer, C., Romanic, D., Parvu, D., LoTufo, J., Costache, A., 2017. Novel techniques in wind engineering. *J. Wind Eng. Ind. Aerodyn.* 171, 12–33.
<https://doi.org/10.1016/j.jweia.2017.09.010>
- Hjelmfelt M, 1988. Structure and Life Cycle of Microburst Outflows Observed in Colorado. *J. APPL. METEOROL.* 27(8, Aug. 1988) 900-927 27, 1–27.
- Hu, H., Yang, Z., Sarkar, P., Haan, F., 2011. Characterization of the wind loads and flow fields around a gable-roof building model in tornado-like winds. *Exp. Fluids* 51, 835–851.
<https://doi.org/10.1007/s00348-011-1102-6>
- Iida, Y., Uematsu, Y., 2019. Numerical study of wind loads on buildings induced by downbursts. *J. Wind Eng. Ind. Aerodyn.* 191, 103–116. <https://doi.org/10.1016/j.jweia.2019.05.018>
- Jensen, M., 1958. The model-law for phenomena in natural wind. *Ingenioren.* 2. 121-128.
- Jesson, M., Sterling, M., Letchford, C., Haines, M., 2015. Aerodynamic forces on generic buildings subject to transient, downburst-type winds. *J. Wind Eng. Ind. Aerodyn.* 137, 58–68. <https://doi.org/10.1016/j.jweia.2014.12.003>
- Jubayer, C., Elatar, A., Hangan, H., 2016. Pressure distributions on a low-rise building in a laboratory simulated downburst. In: *Proceedings of the 8th International Colloquium on Bluff Body Aerodynamics and Applications*, Boston, Massachusetts, USA, June 2016. 8th Int. Colloq. Bluff Body Aerodyn. Appl.
- Letchford, C.W., Chay, M.T., 2002. Pressure distributions on a cube in a simulated thunderstorm downburst. Part B: Moving downburst observations. *J. Wind Eng. Ind. Aerodyn.* 90, 733–753. [https://doi.org/10.1016/S0167-6105\(02\)00163-0](https://doi.org/10.1016/S0167-6105(02)00163-0)
- Lewellen, W.S., 1962. A solution for three-dimensional vortex flows with strong circulation. *J. Fluid Mech.* , Vol. 14 , Issue 3 , Novemb. 1962 , pp. 420 - 432 420–433.

- Lombardo, F.T., Mason, M.S., de Alba, A.Z., 2018. Investigation of a downburst loading event on a full-scale low-rise building. *J. Wind Eng. Ind. Aerodyn.* 182, 272–285.
<https://doi.org/10.1016/j.jweia.2018.09.020>
- Lombardo, F.T., Roueche, D.B., Prevatt, D.O., 2015. Comparison of two methods of near-surface wind speed estimation in the 22 May, 2011 Joplin, Missouri Tornado. *J. Wind Eng. Ind. Aerodyn.* 138, 87–97. <https://doi.org/10.1016/j.jweia.2014.12.007>
- Mason, M.S., James, D.L., Letchford, C.W., 2009. Wind pressure measurements on a cube subjected to pulsed impinging jet flow. *Wind Struct. An Int. J.* 12, 77–88.
<https://doi.org/10.12989/was.2009.12.1.077>
- McConville, A.C., Sterling, M., Baker, C.J., 2009. The physical simulation of thunderstorm downbursts using an impinging jet. *Wind Struct. An Int. J.* 12, 133–139.
- Mishra, Amit R., James, D.L., Letchford, C.W., 2008. Physical simulation of a single-celled tornado-like vortex, Part A: Flow field characterization. *J. Wind Eng. Ind. Aerodyn.* 96, 1243–1257. <https://doi.org/10.1016/j.jweia.2008.02.063>
- Mishra, A. R., James, D.L., Letchford, C.W., 2008. Physical simulation of a single-celled tornado-like vortex, Part B: Wind loading on a cubical model. *J. Wind Eng. Ind. Aerodyn.* 96, 1258–1273. <https://doi.org/10.1016/j.jweia.2008.02.027>
- NBC2015, 2015. User’s Guide-NBC 2015, Structural Commentaries (Part 4). Issued by the Canadian Commission on Buildings and Fire Codes, National Research Council of Canada.
- Razavi, A., Sarkar, P.P., 2018. Tornado-induced wind loads on a low-rise building: Influence of swirl ratio, translation speed and building parameters. *Eng. Struct.* 167, 1–12.
<https://doi.org/10.1016/j.engstruct.2018.03.020>
- Refan, M., Hangan, H., 2016. Characterization of tornado-like flow fields in a new model scale wind testing chamber. *J. Wind Eng. Ind. Aerodyn.* 151, 107–121.
<https://doi.org/10.1016/j.jweia.2016.02.002>
- Sabareesh, G.R., Matsui, M., Tamura, Y., 2012. Dependence of surface pressures on a cubic building in tornado like flow on building location and ground roughness. *J. Wind Eng. Ind. Aerodyn.* 103, 50–59. <https://doi.org/10.1016/j.jweia.2012.02.011>

- Sengupta, A., Haan, F.L., Sarkar, P.P., Balaramudu, V., 2008. Transient loads on buildings in microburst and tornado winds. *J. Wind Eng. Ind. Aerodyn.* 96, 2173–2187.
<https://doi.org/10.1016/j.jweia.2008.02.050>
- Sengupta, A., Sarkar, P.P., 2008. Experimental measurement and numerical simulation of an impinging jet with application to thunderstorm microburst winds. *J. Wind Eng. Ind. Aerodyn.* 96, 345–365. <https://doi.org/10.1016/j.jweia.2007.09.001>
- Stathopoulos, T., 1984. Design and fabrication of a wind tunnel for building aerodynamics. *J. Wind Eng. Ind. Aerodyn.* 16, 361–376. [https://doi.org/10.1016/0167-6105\(84\)90018-7](https://doi.org/10.1016/0167-6105(84)90018-7)
- Stathopoulos, T., Saathoff, P., 1991. Wind pressure on roofs of various geometries. *J. Wind Eng. Ind. Aerodyn.* 38, 273–284. [https://doi.org/10.1016/0167-6105\(91\)90047-Z](https://doi.org/10.1016/0167-6105(91)90047-Z)
- Wang, J., Cao, S., Pang, W., Cao, J., 2018. Experimental Study on Tornado-Induced Wind Pressures on a Cubic Building with Openings. *J. Struct. Eng. (United States)* 144, 1–14.
[https://doi.org/10.1061/\(ASCE\)ST.1943-541X.0001952](https://doi.org/10.1061/(ASCE)ST.1943-541X.0001952)
- Wang, J., Cao, S., Pang, W., Cao, J., 2017. Experimental Study on Effects of Ground Roughness on Flow Characteristics of Tornado-Like Vortices. *Boundary-Layer Meteorol.* 162, 319–339. <https://doi.org/10.1007/s10546-016-0201-6>
- Ward, N.B., 1972. The Exploration of Certain Features of Tornado Dynamics Using a Laboratory Model. *J. Atmos. Sci.* 29pp. 1194. 7, 1–16.
- Ying, S. J., and Chang, C.C., 1970. “Exploratory Model Study of Tornado-Like Vortex Dynamics,” *J. Atmos. Sci.* 27(1) pp. 3-14 7, 1–16.
- Zhang, Y., Hu, H., Sarkar, P.P., 2014. Comparison of microburst-wind loads on low-rise structures of various geometric shapes. *J. Wind Eng. Ind. Aerodyn.* 133, 181–190.
<https://doi.org/10.1016/j.jweia.2014.06.012>
- Zhang, Y., Sarkar, P., Hu, H., 2013. An experimental study of flow fields and wind loads on gable-roof building models in microburst-like wind. *Exp. Fluids* 54.
<https://doi.org/10.1007/s00348-013-1511-9>

Appendix A

Contours of mean and peak pressure coefficients of the 10 m height building for all wind directions.

Appendix A 1: 0° wind direction.

Appendix A 2: 15° wind direction.

Appendix A 3: 30° wind direction.

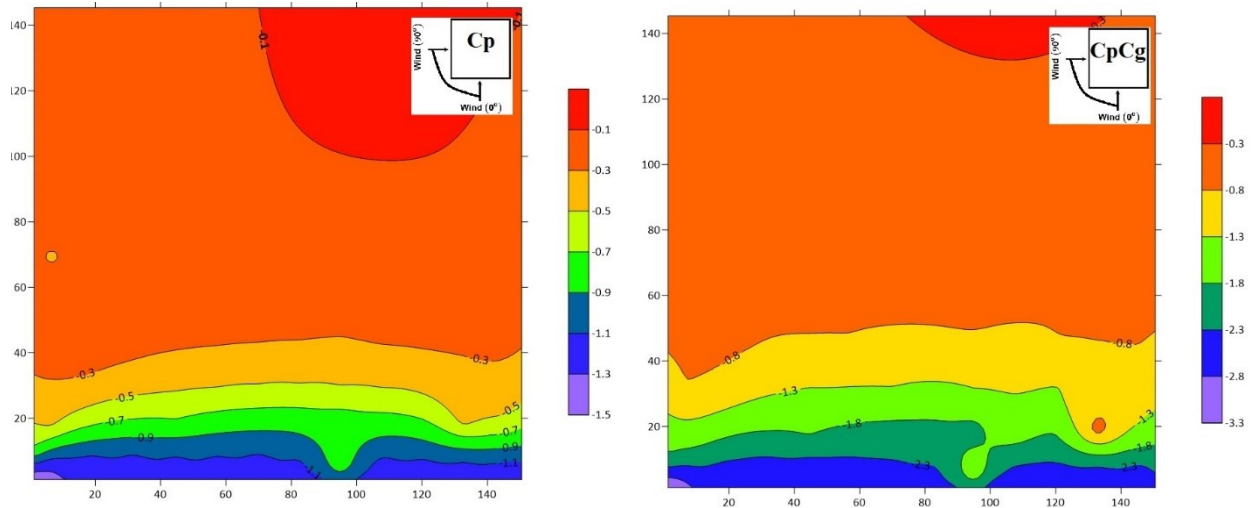
Appendix A 4: 45° wind direction.

Appendix A 5: 60° wind direction.

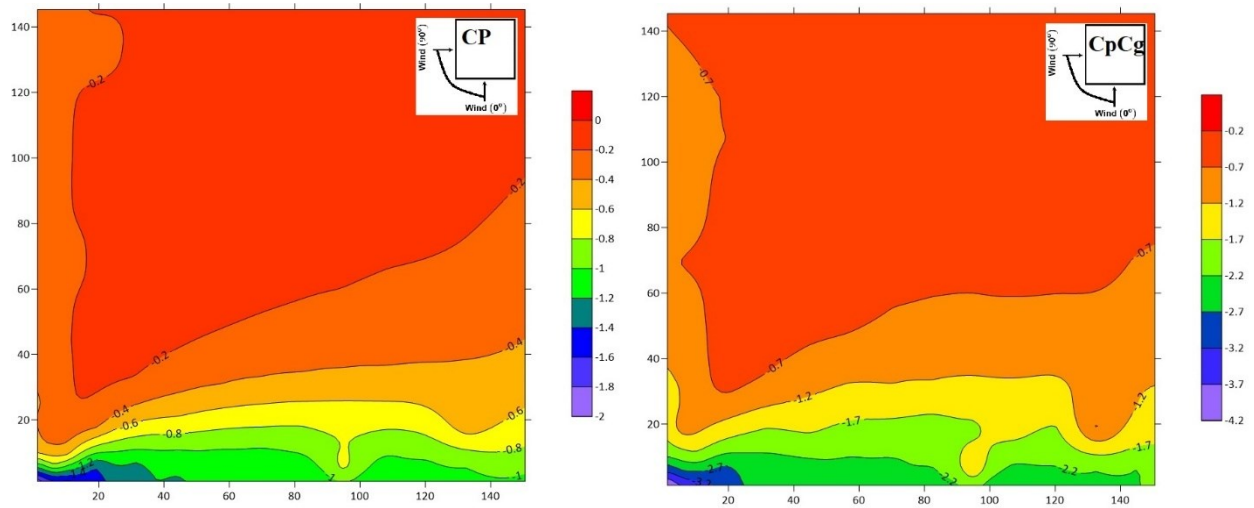
Appendix A 6: 75° wind direction.

Appendix A 7: 90° wind direction.

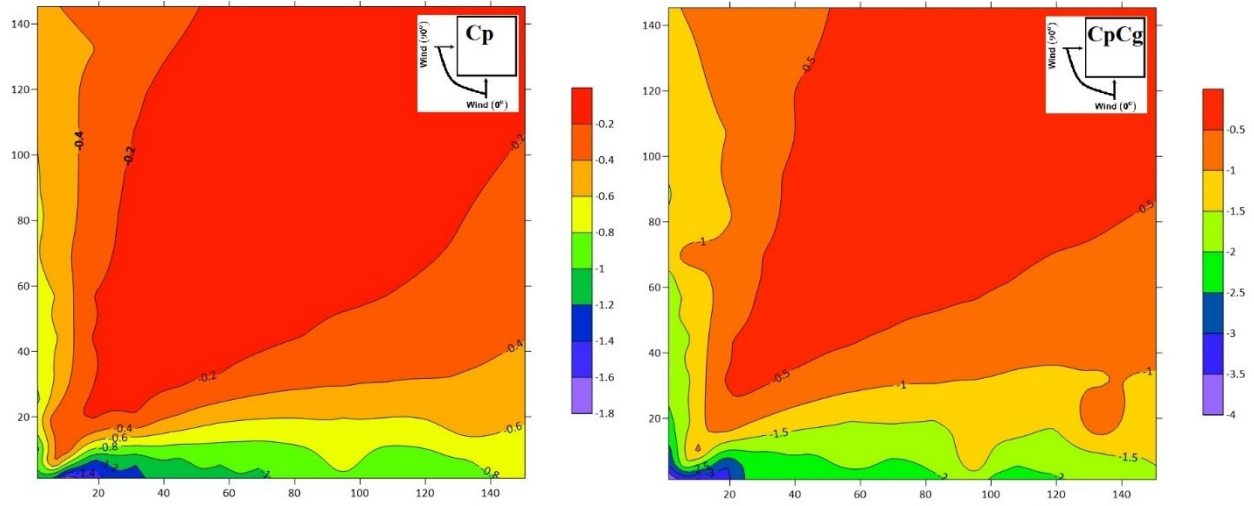
Appendix A 1: Contours of mean and peak pressure coefficients for 0° wind direction.



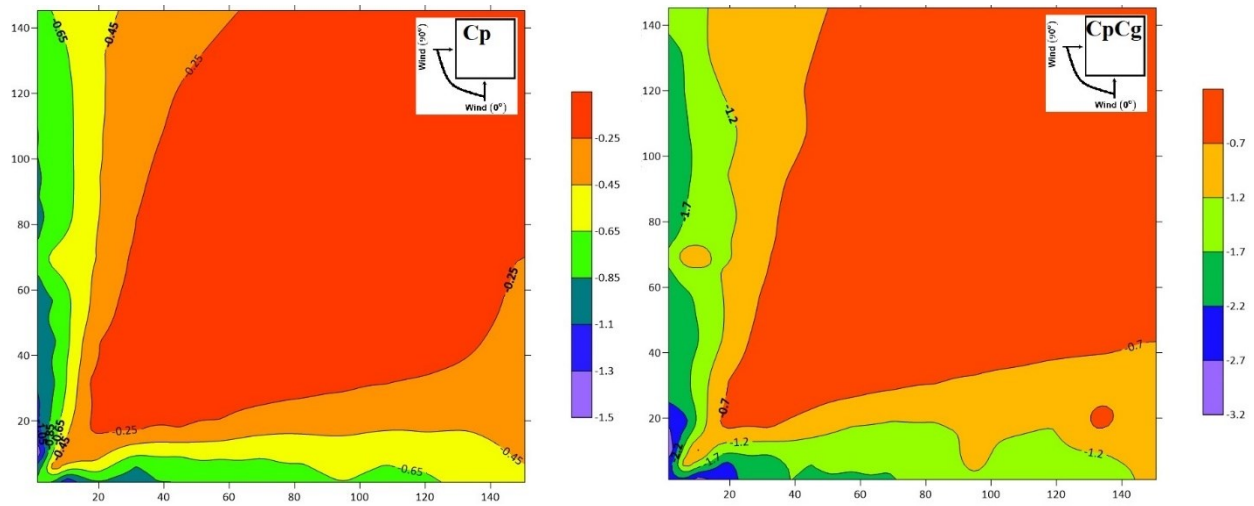
Appendix A 2: Contours of mean and peak pressure coefficients for 15° wind direction.



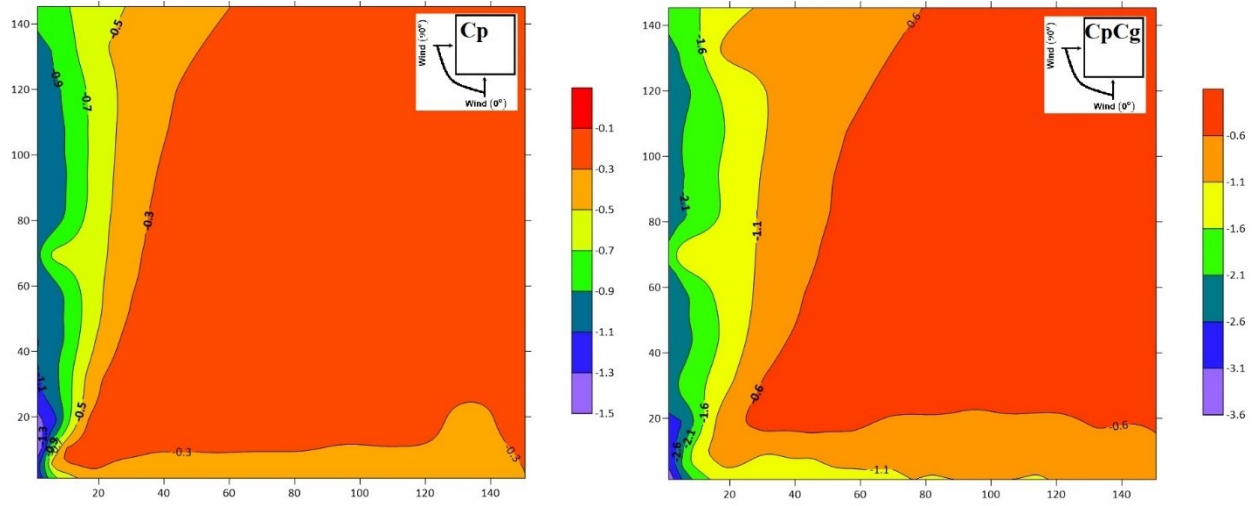
Appendix A 3: Contours of mean and peak pressure coefficients for 30° wind direction.



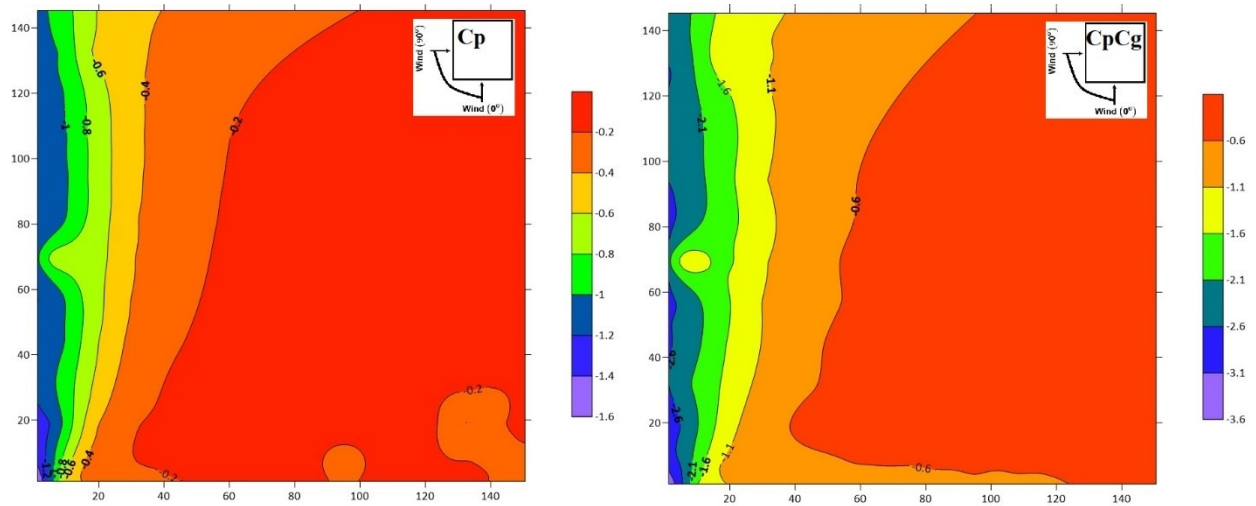
Appendix A 4: Contours of mean and peak pressure coefficients for 45° wind direction.



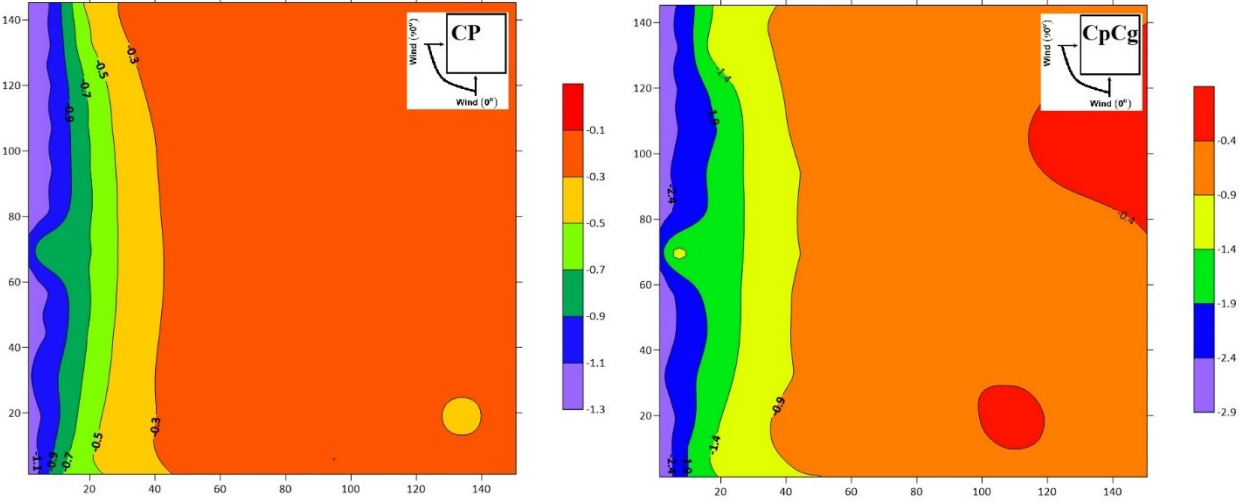
Appendix A 5: Contours of mean and peak pressure coefficients for 60° wind direction.



Appendix A 6: Contours of mean and peak pressure coefficients for 75° wind direction.



Appendix A 7: Contours of mean and peak pressure coefficients for 90° wind direction.



Appendix B

Contours of mean and peak pressure coefficients of the 20 m height building for all wind directions.

Appendix B 1: 0° wind direction.

Appendix B 2: 15° wind direction.

Appendix B 3: 30° wind direction.

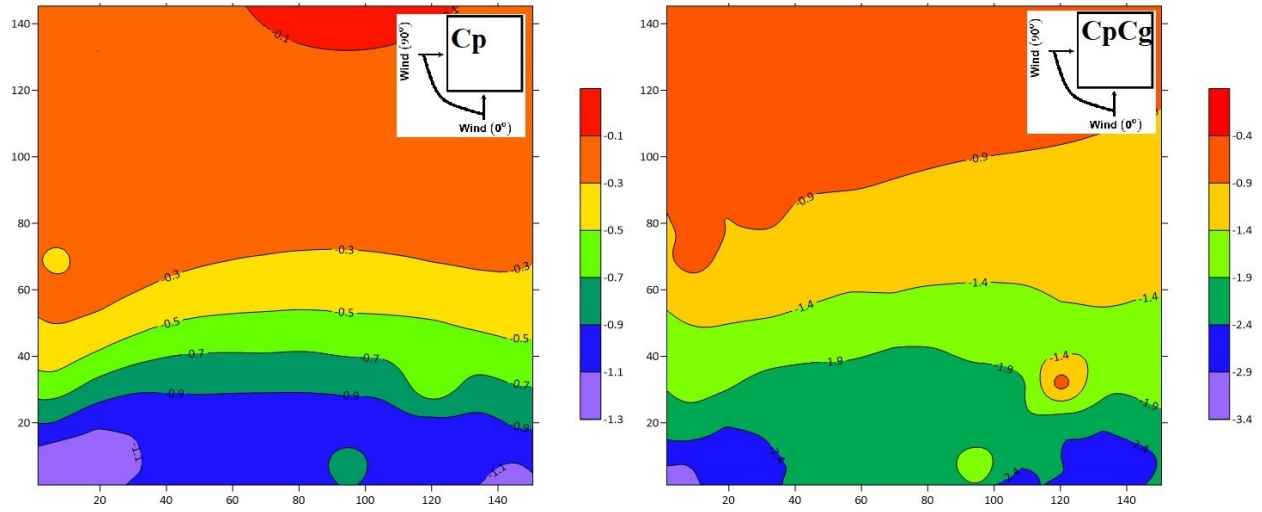
Appendix B 4: 45° wind direction.

Appendix B 5: 60° wind direction.

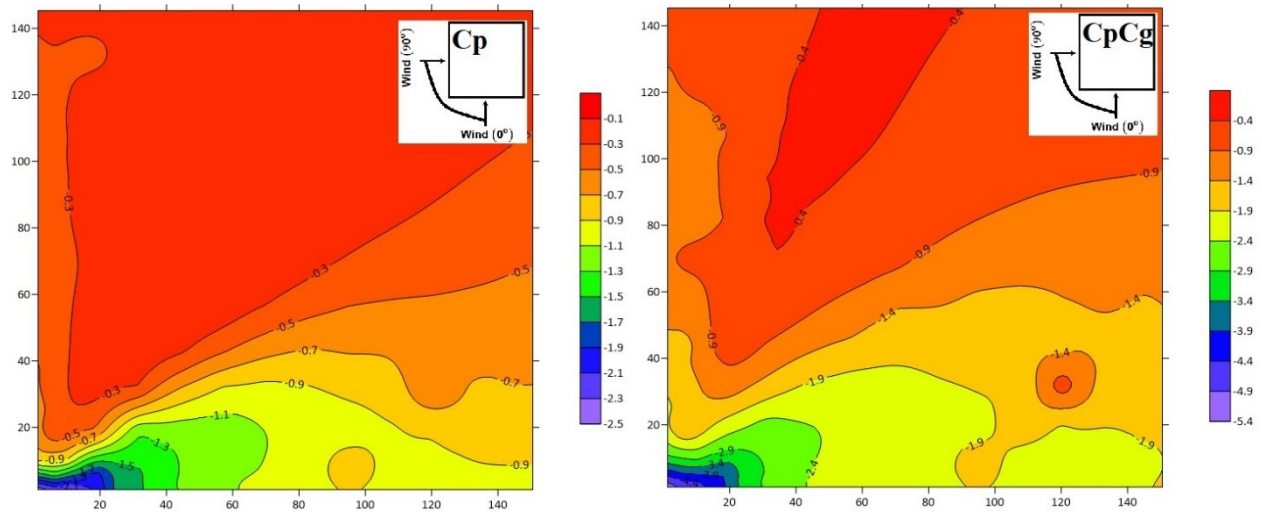
Appendix B 6: 75° wind direction.

Appendix B 7: 90° wind direction

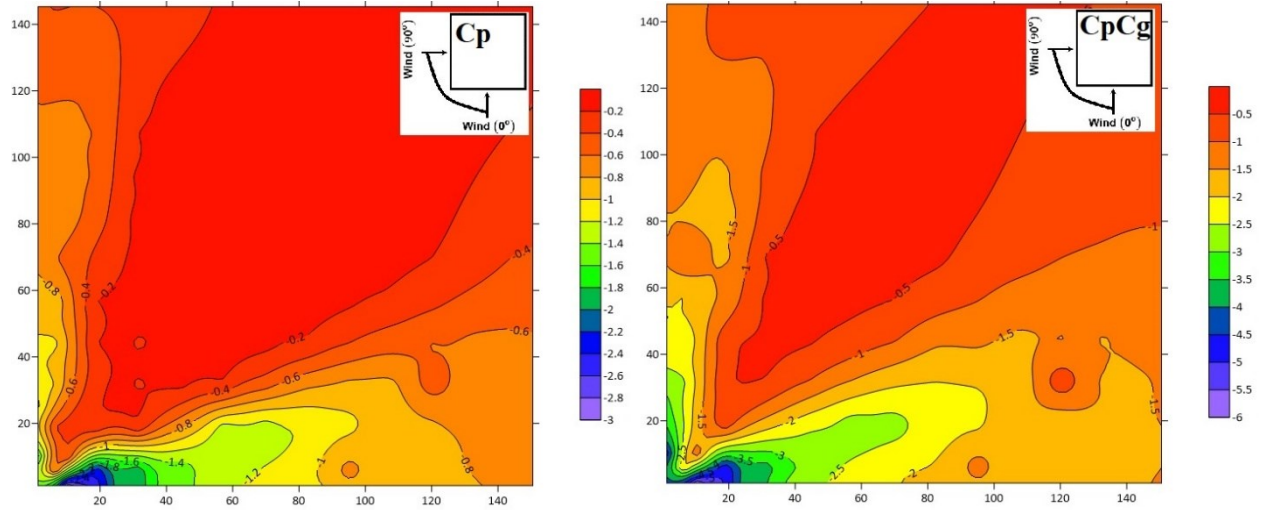
Appendix B 1: Contours of mean and peak pressure coefficients for 0° wind direction.



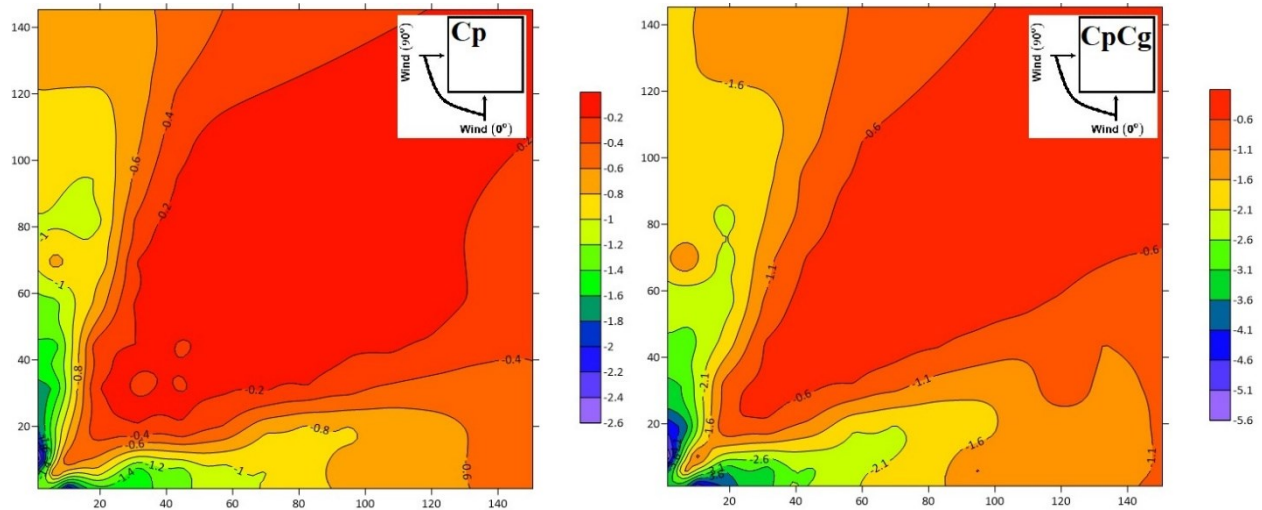
Appendix B 2: Contours of mean and peak pressure coefficients for 15° wind direction.



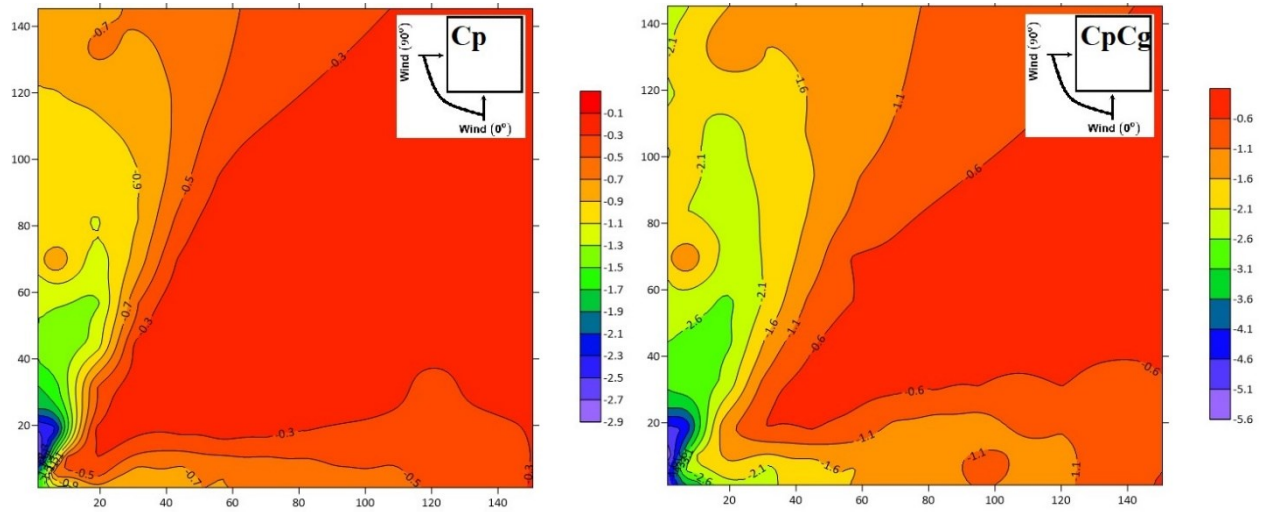
Appendix B 3: Contours of mean and peak pressure coefficients for 30° wind direction.



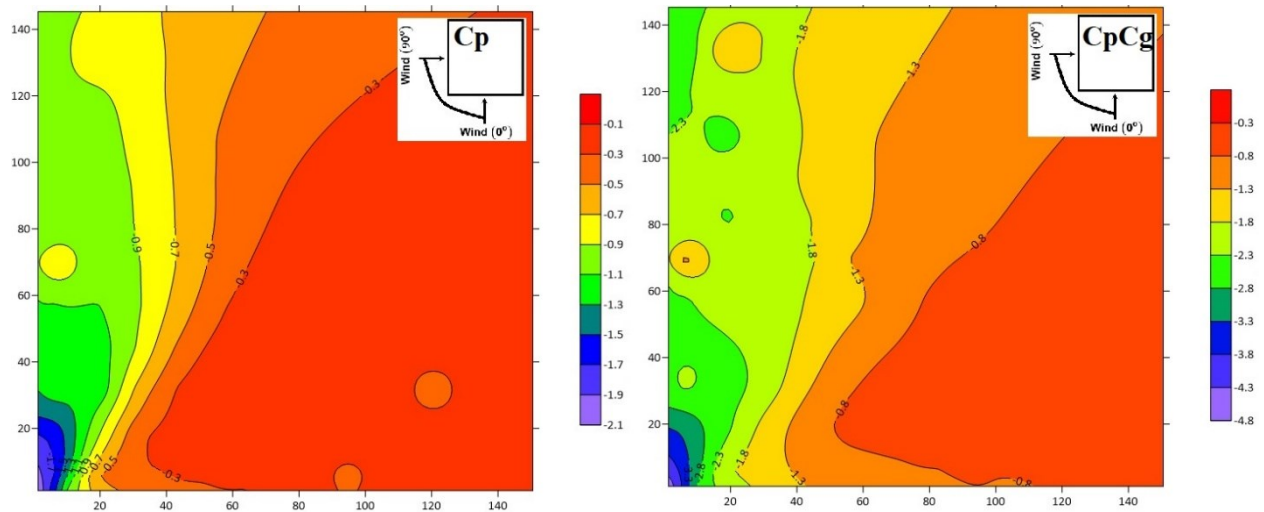
Appendix B 4: Contours of mean and peak pressure coefficients for 45° wind direction.



Appendix B 5: Contours of mean and peak pressure coefficients for 60° wind direction.



Appendix B 6: Contours of mean and peak pressure coefficients for 75° wind direction.



Appendix B 7: Contours of mean and peak pressure coefficients for 90° wind direction.

